

https://dspace.org/

Enhancement of photo-conversion efficiency of organic solar cells by plasmon resonance effect

Otieno, Francis Otieno

2016

http://hdl.handle.net/10539/19333

Downloaded from a DSpace repository. https://dspace.org/

Francis Otieno Otieno

ENHANCEMENT OF PHOTO-CONVERSION EFFICIENCY OF ORGANIC SOLAR CELLS BY PLASMON RESONANCE EFFECT.

DISSERTATION

Presented in fulfilment of the requirements for the degree of

Master of Science

In the Faculty of Science

School of Physics

University of the Witwatersrand

Private Bag 3

WITS

2050

Supervisor: Dr. Daniel Wamwangi



DECLARATION

I declare that “Enhancement of photo-conversion efficiency by plasmon resonance effect.” is my own, unaided work submitted at the University of the Witwatersrand, Johannesburg. And that this work has not been submitted for any degree or examination in any other institution of higher learning. Moreover, that all sources used or quoted have been indicated and acknowledged with complete references.

Name: Francis Otieno Otieno

Date: .....2015 Signature:.....

Acknowledgment

This thesis is an important milestone towards the realization of my dream of becoming a researcher. The journey has been characterized by a number of challenges but managed to go through with the help of a number of individuals, groups and organizations. My heartfelt gratitude goes to my beloved wife, Mildred who has been very supportive and understanding. She has been a great source of strength providing the pillar to lean on wherever experiments failed in the lab and a celebration atmosphere whenever they went through. Besides, she has been so motherly and caring wife ensuring my peaceful and satisfactory stay in Johannesburg. My beloved dad 'Wuon Oluoch' for his dedicated prayers, sound advice and more so for initiating the urge to further my education.

I would also like to thank my MSc advisor, Dr Daniel Wamwangi for his invaluable contribution and critic that were always conveyed in a brotherly manner. His appreciation of high quality science and integrity has been a marvel and has made me to strive to be a better scientist. To Dr Nosipho Moloto for her discussions and critics that was quite instrumental during the analysis of the results. Thanks also go to the Quantum dots group under Dr Nosipho (Mildred, Rudo, Siziwe, Stef, Pierre, Nthabi and Lerato) for always giving me a forum to present my findings and their constructive critics as well as always making me feel at home.

I owe a great debt of gratitude to all of my colleagues who went out of their way to orientate me into the thin film laboratory. In particular, I want to thank Dr Kamala Kamalakan, Lordwell Jhamba and Lesias Kotane for their absolutely invaluable support.

Special thanks go to Material for Energy Research Group (MERG) for their generous, timely funding that always enabled me pay my fees as well up-keep. The group critics and discussions were quite helpful in my data analysis.

Appreciation also goes to Wits and the Material Physics Research Institute for giving me the opportunity to undertake my research as well providing required facilities and expertise. In particular, the MMU for enabling me carry out microscopy.

Finally big thanks to God almighty for the grace of life and guidance.

Dedication

To my late beloved mum-Nyo Ogola, my dad- wuon Oluoch and dear wife Mildred.

List of figures

Figure 1.1 Solar radiation spectrum AM0 and AM1.5 as well as black body spectrum at a temperature of 5250 ^{o}C……14

Figure 1.2 a) showing industrial emission into the atmosphere b) shows IPCC's fifth assessment report on various scenarios of future emissions ……..……..16

Figure 1.3 a) shows alternating single and double adjacent carbon atoms in conjugated polymer while b) and c) shows The polymer poly (3-hexylthiophene) (P3HT) and the fullerene [6,6]-phenyl-C61 butyric acid methyl ester (PCBM) respectively……19

Figure 2.1 Schematic diagram of the photocurrent generation mechanism in organic photovoltaic devices……...33

Figure 2.2 a) The J-V characteristics of solar cell in the dark and under illumination b) equivalent circuit diagram…….…….33

Figure 2.3 Equivalent circuit for parasitic series and shunt resistances in a solar cell circuit……..37

Figure 2.4 a-b) The effect of parasitic series and shunt resistance (R_s and R_{sh}) on a solar cell's *I-V* curve……..…….……..…….38

Figure 3.1 Surface plasmon resonance where the free electrons in the metal nanoparticle are driven into oscillation…….……42

Figure 3.2 The green Lycurgus cup containing tiny amount of metal nanoparticles (MNPs) giving it this unusual optical characteristic……...…….43

Figure 3.3 Schematic representation of surface plasmon resonance effect along metal/dielectric interface……...……..44

Figure 4.1 Schematic diagram of RF magnetron sputtering apparatus and b) sputtering mechanism….54

Figure 4.2 a) Schematic diagram of thermal evaporator fitted with quartz crystal monitor b) thermal evaporation mechanism……...……..57

Figure 4.3 Schematic diagram of the cantilever-tip assembly used in an AFM b) Resonance curves of a Tapping Mode cantilever above and close to the surface c) Force curve highlighting the motion of an oscillating cantilever in Tapping Mode……..……..60

Figure 4.4 AFM images of as-deposited Ag nanoparticles a) thermally evaporated film with substrate directly above the source b) AFM derived dimensions of the films c) RF sputtered Ag film……..61

Figure 4.5 AFM images of as-deposited thermally evaporated Ag nanoparticles with the substrate inclined at an angle of 70^{o} with the source…… 61

Figure 4.6 AFM image of RF sputtered Ag nanoparticles after thermal annealing process in Argon filled furnace at different temperatures a) as-deposited b) annealed at 100 ^{o}C c) annealed at 150 ^{o}C d) annealed at 200 ^{o}C e) annealed at 250 ^{o}C…….....62

Figure 4.7 Size distribution of RF sputtered Ag nanoparticles upon annealing at temperature range of as-deposited and those annealed at a temperature range of 100-250 °C in argon ambient……...……63
Figure 4.8 Graphical variations of mean diameter and surface coverage with annealing temperature……..……..64
Figure 4.9 Arrhenius plot to show the dependence of coverage with temperature, the activation energy has been determined to 50 ±13 meV……..……...66
Figure 4.10 AFM image of RF sputtered Ag nanoparticles annealed in situ at different temperatures a) 150 ^{o}C b) 200 ^{o}C c) 300 ^{o}C……..…….……67
Figure 4.11 Optical absorption spectra of Ag nanoparticles grown by RF sputtering system at different powers for 8 seconds before being annealed at different temperature in Argon ambient……...…….68
Figure 4.12 Optical absorption spectra of Ag nanoparticles grown by RF sputtering system at different power before being annealed at a particular temperature in Argon ambient……...……70
Figure 4.13 Optical absorption spectra of Ag nanoparticles grown by RF sputtering system at a DC power of 15 W for 12 seconds before annealing in air……...……..71
Figure 4.14 Optical absorption spectra of Ag nanoparticles grown by RF sputtering system at power of 10W for different periods of time before being annealed in air……...……72
Figure 4.15 Optical absorption spectra of Gold NPs grown by RF sputtering system at DC power of 10W for different periods of time……...……..73
Figure 5.1 Device architecture of reference cell……..76
Figure 5.2 The morphology of P3HT:PCBM blend before and after proper dissolution in chlorobenzene…….……..77
Figure 5.3 UV-Vis absorption spectra of P3HT: PCBM blend films as cast and after annealing for 10 minutes at different temperatures (50 ^{o}C, 70 ^{o}C and 90 ^{o}C ± 10 ^{o}C)……79
Figure 5.4 UV-Vis absorption spectra of P3HT: PCBM blend films as cast and after annealing at a temperature of 50 ^{o}C ± 10 ^{o}C for different time intervals (5 minutes, 10 minutes, 15 minutes and 20 minutes)…..……...80
Figure 5.5 J-V characteristics (AM1.5, 70Mw/cm^{2}) of as-fabricated device and the annealed at different temperatures (50 ^{o}C, 70 ^{o}C and 90 ^{o}C ± 10 ^{o}C) for 10 minutes in Argon ambience……...……..…81
Figure 5.6 J-V characteristics (AM1.5, 70mW/cm^{2}) of as-fabricated device and the annealed at different time interval (10 minutes, 15 minutes and 20 minutes) at a temperature of 50 ^{o}C ± 10 ^{o}C in Argon ambience…….……..…….83
Figure 5.7 Device architectures of OSC with NPs on top of ITO……...……84
Figure 5.8 Morphology of film of P3HT:PCBM blend with a) NPs beneath (On top of ITO) and b) NPs on top of the active layer……...……...……85
Figure 5.9 Different plasmonic geometries for light-trapping for thin-film solar cells……..…….……86

Figure 5.10. The optical absorption spectra of the P3HT:PCBM BHJ without NPs as well as with NPs annealed at 100 °C, 150 °C, 200 °C and 250 °C (the absorbance is baseline corrected with Indium tin oxide (ITO) coated glass as the reference standard)……..…….……86

Figure 5.11 (a,) shows a *J–V* characteristics of both devices under illumination of devices with incorporated Ag sputtered on top of hole transport layer (ITO) and annealed at 100 °C and 250 °C while (b) is a semi-log plot of the J-V characteristics in the dark…….……..…87

Figure 6.1 a) I-V characteristics for ITO/PEDOT:PSS/P3HT:PCBM/Al solar device degrading with time in air ambience b-c) Photovoltaic performance of unencapsulated device as a function of exposure time to ambient air under AM 1.5 G filtered spectral illumination at incident intensity, 70 mW/cm^2 …….……..98

Figure 6.2 (a) I-V characteristics for ITO/PEDOT:PSS/P3HT:PCBM/Al solar device in the dark as a function of time in ambient air (b) Semi-log graph of reference device compared to device after 137 hours…….……98

Figure 6.3 UV-Vis spectrometer measurement of absorbance of P3HT:PCBM film with time before annealing at 50 °C and 70 °C in Argon ambience……...……99

Figure 6.4 (a) Molecular structure and (b) triclinic bulk structure of pentacene (c) thin film phase….100

Figure 6.5 (a-b) AFM image of RF sputtered Ag nanoparticles annealed at 100 °C and 250 °C respectively in Argon ambience (c-d) 22.2 nm evaporated pentacene on the annealed NPs ……..……...……...101

Figure 6.6 UV-Vis spectrometer measurement of absorbance of pentacene film on top of annealed Ag nanoparticles…… 102

Figure 6.7 UV-Vis spectrometer measurement of absorbance of PEDOT:PSS, P3HT:PCBM active layer on top of annealed Ag nanoparticles encapsulated with pentacene thin film……. 103

Figure 6.8 Band energy diagram for ITO/Ag nanoparticles/Pentacene/PEDOT:PSS/P3HT:PCBM/Al device…….……..…104

Figure 6.9 I-V characteristics for ITO/PEDOT:PSS/P3HT:PCBM/Al solar device degrading with time in air ambience under AM 1.5 G filtered spectral illumination at incident intensity, 70 mW/cm^2 …..104

Figure 6.10 Photovoltaic performance of encapsulated device as a function of exposure time to ambient air…….……...…105

List of tables

Table 4.1 Summary of AFM analysis on the Ag nanoparticles annealed at different temperature in Argon filled furnace……. 64

Table 5-1 Summary of the performance of the OPVs as-fabricated and after annealing at different temperature for 10 minutes in Argon ambience……...….81

Table 5-2 Summary of the performance of the OPVs upon annealing for different time interval at a temperature of 50 ^{o}C ± 10 ^{o}C in Argon ambience……..……...…83
Table 5-3. Summary of the performance of the OPVs with different Ag nanoparticles size sputtered on top of the ITO…….…… 88

List of symbols

A	Acceptor
AFM	Atomic force microscope
Ag	Silver
Al	Aluminium
AM	Air-Mass
Au	Gold
BHJ	Bulk heterojunction
CT	Charge-transfer state
D	Donor
DC	Direct current
DI	Deionized water
EU	European Union
FF	Fill factor
FRET	Förster resonance energy transfer
GHGs	Greenhouse gases
HOMO	Highest occupied molecular orbital
I_{max}	Maximum current
IPCC	Intergovernmental panel on climate change
ITO	Indium tin oxide
J_{sc}	Short circuit current density
J-V	Current density-voltage
LD	Exciton diffusion length
LiF	Lithium fluoride
LSPs	Localized surface plasmons
MgPh	Magnesium phthalocynines
MNPs	Metal nanoparticles
NPs	Nano-particles

NIR	Near Infra-red
OPVs	Organic photovoltaics
OSCs	Organic solar cells
P3HT	Poly(3-hexylthiophene-2,5-diyl)
PCBM	[6,6]-phenyl-C61-butyric acid methyl ester
PCE	Power conversion efficiency
PEDOT:PSS	poly(3,4- ethylenedioxy thiophene): poly(styrenesulfonate)
PID	Proportional-integral-differential
P_{in}	Incident light power density
PQC	Power-conversion efficiency
PVD	Physical vapor deposition
R_{DA}	Inter-molecular distance
RF	Radio frequency
R_s	Series resistance
R_{sh}	Shunt resistance
SERS	Surface Enhanced Raman Scattering
SPR	Surface Plasmon resonance
V_{oc}	Open circuit voltage

Abstract

Organic Photovoltaic (OPVs) is a promising alternative technology to provide clean and inexhaustible energy due to their excellent optoelectronic properties of the active polymer blends. The organic polymers have low weight, tunable electrical and optical properties besides being relatively insensitive to film imperfections which in the long run enable low-cost high-throughput roll-to-roll processing. However, their photo-conversion efficiency (PCE) and instability to air remains their greatest drawback as these preclude their commercialization. Indeed the highest power-conversion efficiency reported in literature is between 10-12 % compared to their inorganic counterparts (40 %). Therefore there is great need for improvement to make them competitive with grid parity. In this thesis, the major factors limiting the efficiency of organic solar cells such as light absorption, exciton diffusion and dissociation as well as charge collection are investigated and discussed.

Despite the high thickness dependent absorption coefficients ($>10^5$ cm^{-1}) within the visible spectrum the materials exhibit short exciton diffusion lengths (10-20 nm) which limit the optimal active layer thickness to a few nanometers. Improving optical absorption within this thickness forms the basis of this project. We report the use of surface Plasmons synthesized by both thermal evaporation and Radio Frequency (RF) magnetron sputtering system to tune and enhance optical absorption and scattering using the surface Plasmon resonance effect. The NPs were annealed at various temperatures and for different times to reconstruct and modify their shapes, sizes as well as the inter-particle distance (coverage).

Stability is of paramount importance in organic semiconductor devices. Serious degradation in air constrains their applications potential. The study further investigates the mechanisms that determine the stability of organic photovoltaic devices. Our results depict the degradation mechanisms and their circumvention through the use of high mobility pentacene to improve stability.

Table of contents.

Declaration……..2
Acknowledgment……....3
Dedication……...5
List of figures……..6
List of tables……8
List of symbols……9
Abstract……..11
Chapter 1 Introduction ……..……....14

1.1 The solar emission spectrum .....……..14
1.2 The importance of solar energy as alternative energy source…….15
1.3 Development of Photovoltaics……..……..17
1.4 Conjugated polymers……..……19
1.5 Problem statement……20
1.6 Objectives of the study……..…….. 21
1.7 Structure of the thesis……..…… 22

Chapter 2 Working principles of Organic solar cells…….…….……... 27

2.1 Photogeneration of charge carriers…….…….. 27
2.2 Exciton diffusion……..……..……. .29
2.3 Exciton dissociation……..…… 31
2.4 Charge transport and collection……..…….……..32
2.5 Parameters used in solar cell…….…….33

Chapter 3 Nanoparticle plasmonics……..42

3.1 Brief overview…….. ..42
3.2 Localized surface plasmons……44
3.3 Surface plasmon polaritons……44
3.4 Applications of nanoparticle plasmon resonance……46
3.5 Plasmonics for organic solar cells……...48
3.6 Mechanisms of absorption by plasmon resonance…….....48

Chapter 4
Methodology…….. 53

4.1 Brief overview……. 54

4.2 RF sputtering technique……... 54

4.3 Thermal evaporation technique……... 56

4.4 Growth and characterization …….. 58

4.41 Morphology of NPs ……... 58

4.42 Insitu annealing……..……..……... 67

4.43 Optical properties surface plasmons…….. 68

Chapter 5 Efficiency enhancement…… 76

5.1 Effect of thermal annealing…… 76

5.2 Absorption enhancement using NPs…….…….. 84

5.3 Device results and discussions..…….. 87

Chapter 6 Encapsulation using pentacene……. 92

6.1 Degradation mechanisms…… 92

6.2 Chemical degradation…….…… 92

6.3 Physical and mechanical degradation...…….…….. 95

6.4 Growth and characterization of pentacene……..……100

6.5 Device results and discussions…..…….…….……101

Chapter 7 Conclusion and future work…….……108

7.1 Conclusion…….…….….108

7.2 Future work and recommendations..…….…….…….110

Workshop/ conferences attended…….…….111

Chapter 1. Introduction

1.1 The solar emission spectrum

The Sun is by far the most important energy source for life emitting energy as electromagnetic radiation at an extremely large and relatively constant rate. Its broad spectral emission range spans through the ultraviolet, visible and infrared regions of the electromagnetic spectrum. The incident flux of radiant energy per unit area is called irradiance or insolation and it is measured in watts per square meter (W/m^2). The energy emitted is equivalent to a black body radiation at 5250 ^oC [1].

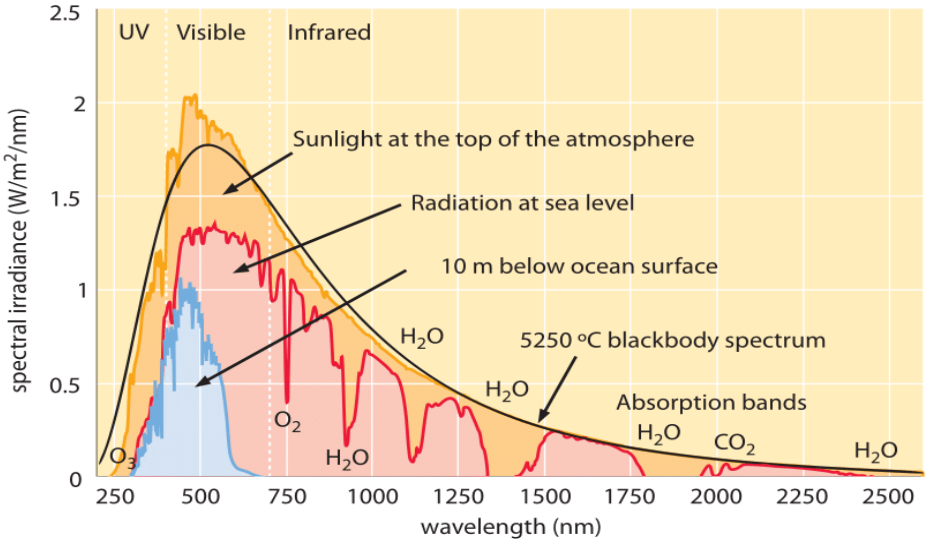


Figure 1.1 Solar radiation spectrum AM0 and AM1.5 as well as black body spectrum at 5250 °C [2].

The solar energy is normally partly absorbed by the atmospheric gases. This absorption changes the shape of the emission spectrum such that the ultraviolet radiation below 300nm is removed mainly by nitrogen, oxygen and ozone. Furthermore infrared photons in the range 1000-2000 nm are absorbed by water.

The incident power is a function of the solar emission spectrum, and it is generally given in terms of the air-mass (AM) coefficient which is the ratio between the optical path length to the sun and the optical path length when the sun is directly overhead [3].

It given by:

$$AM = \frac{1}{\cos\theta} \qquad 1\text{-}1$$

where θ is the angle of the sun, measured from directly overhead. The air-mass simulates the amount of atmosphere propagated by light before reaching the Earth's surface. For instance, AM0 corresponds to the extraterrestrial spectrum, AM1 to the sun in zenith (x^o) while AM1.5 which is the standard for device testing corresponds to when the sun is at an angle of elevation of 48.189^o with a total power density of 100 mW/cm^2 [4].

Besides the aforementioned, diffuse scattering of the solar energy by cosmic particles and molecules may also lead to radiation losses and this account for about 15% [1].

1.2 The importance of solar energy as alternative energy source

Thermal power plants (coal, gas, oil, biomass, geothermal and uranium) constitute 78% of world electricity production. However concerns over the limited life expectancy of fossil fuel reserves, global warming and other environmental implications continue to stimulate and intensify research on renewable energy [5].

In recent years, components of the global carbon balance have changed substantially with major increases in anthropogenic emissions [6] and changes in land and ocean sink fluxes due to climate variability and change [7].

In 2007 an Intergovernmental Panel on Climate Change comprising a panel of scientists convened by the United Nations, produced an elaborate report outlining the threats posed by greenhouse gases (GHGs). According to this report, there is need to reduce CO_2 emissions by

80% below 1990 levels by the year 2050. This call for capping of the atmospheric carbon dioxide concentration below 450 ppm is precipitated by inevitable drastic climate change.

(a)



(b)

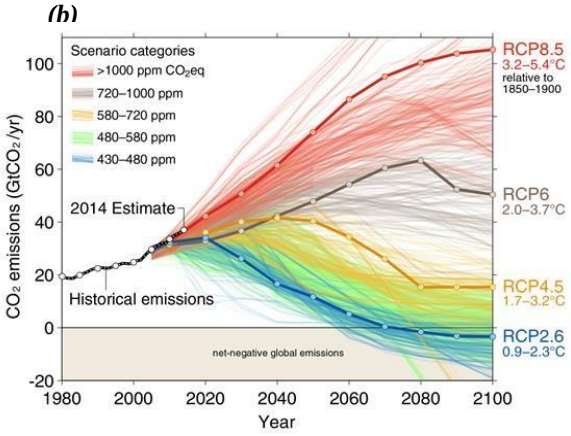


Figure 1.2 a) showing industrial emission into the atmosphere b) shows IPCC's fifth assessment report on various scenarios of future emissions [8].

Global carbon dioxide emissions from fossil fuel combustion and cement production grew by 2.3 per cent to a record high of 36.1 billion tons CO_2 in 2013. In 2014 emissions increased to a further 2.5%, 65 per cent above the level of 1990. The top emitters of CO_2 are China with emissions growth at 4.2% due to faster improvements in carbon intensity of the economy, USA at 2.9%, due to a rebound in coal consumption. Indian emissions grew at 5.1%, due to robust economic growth as well as continued increase in the carbon intensity of the economy while that of the European Union (EU28) decreased at 1.8%, due to a weak economy and emission decreases in some countries offsetting a return to coal led by Poland, Germany, Finland. With current emission rate recorded in 2014, it is likely that the remaining 'quota' to surpass 2°C of global warming will be used up in around 30 years (one generation) [8].

There is an urgent need for sustained and unprecedented reduction of global emission by about 7% per annum in order to stay within the quota [9].

Despite improvements to living standards as well as Gross Domestic Product growth due to industrial development, this has not been without costs. The evidence for anthropogenic global warming primarily due to the combustion of fossil fuels is overwhelming. To prevent

environmental catastrophe, there is great need to end addiction to the use of fossil fuel. This is a monumental task that necessitates a complex solution.

The renewable energy route is proving to be a potential solution to the growing energy challenges due to its abundance and environmental compatibility [10-11]. Solar energy can supply more than the global demands provided that it is efficiently tapped. Incoming solar radiation is on order of $100W/m^2$. This implies that about 1.5×10^{17} W hit the earth's surface – 10 000 times the global consumption per second. Currently the manufacturing and installation costs of photovoltaics (PVs) prohibit them from competing favorably with fossil fuels. Therefore the development on highly efficient and low cost photovoltaics continues to provide the driving force of intense research.

1.3 Development of photovoltaics.

Photovoltaic was discovered by Edmund Becquerel, a French experimental physicist. He reported the generation of photocurrent upon incidence of light on platinum electrodes covered with silver bromide or silver chloride in aqueous solution [12]. The first photoconductivity experiment was made by Smith in 1873 followed by William Adams in 1876 [13]. In 1896 Charles Fritts developed the first large-area photovoltaic device made of metal electrode/semiconductor/semitransparent thin metal electrode. The difficulty in light transmission led to a marginal power conversion efficiency of less than 1% [14].

In 1905, Einstein gave an explanation for the photoelectric effect forming the basis for proper theoretical understanding of photovoltaic effect. In 1906, Pochettino discovered photoconductivity in solid anthracene. This became the first organic compound showing photoconductivity before the phenomenon was re-addressed by Volmer in 1913 [15]. Early work in Organic solar cells was inspired by photosynthesis in which light is absorbed by

chlorophyll (a member of the porphyrin family) to carry out photochemical separation and finally store energy inform of chemical bonds [16].

1950-1960s saw the emergence of organic dye photoacceptors in imaging. Kearns and Calvin in 1958 fabricated cells made of magnesium phthalocynines (MgPh) giving an open circuit voltage of 200 mV [17]. The first polymer-based solar cells were fabricated in 1980s [18-19]. They had their active layer made of a single layer of a polymer or a dye. These devices were characterized by a low power conversion efficiency (PCE) (<0.1%). In 1986 Tang made a great discovery in OSCs when he fabricated a cell composed of a donor–acceptor (DA) heterojunction using phthalocyanine and perylene derivatives. A photo-conversion efficiency of η_P = 0·95% was obtained with these members of the porphyrin family [20]. Since then Polymer BHJ solar cells composed of interpenetrating networks of electron donor and acceptor have gained considerable interest due to their low-cost, simple and cost-effective processes based on the high-throughput roll-to-roll systems, and high application versatility. The hole and electron mobility in the blend depends on the nanoscale morphology of the blend which is determined by;

- The type of solvent used,
- Processing temperature,
- The composition ratios between polymer and fullerene,
- The solution concentration, thermal annealing, and the solubility and miscibility of the blends [21-25].

Hiramoto demonstrated the first small molecular BHJ [26] while in 1994 Yu et. al, fabricated the first polymer:C60 BHJ photodetector [27].

A blend of P3HT and PCBM which is investigated in this thesis was first reported by Hummelen's Group with a PCE of 0.2% [28]. The same year Padingger's Group showed an improvement in PCE to 3.5% after changing weight ratio to 1:1 from 1:4 before annealing the

active layer at 75 °C [29]. This opened quite a number of groups to perform experiments changing the ratio of blend constituents, annealing temperatures as well as duration of annealing of the active layer. In April 2011, Mitsubishi Chemicals reported a PCE of 9.2% [30] before Yang and co-workers achieved 10.6% PCE in 2012 [31].

From the progress made in organic solar cell, the future seems promising with new emerging approaches such as quantum dots/organic hybrid OSCs capable of generating multiple of electrons upon a single incident photon [32-33]

1.4 Conjugated polymers

A conjugated polymer is a long chain of repeating subunit molecules, or monomers with a series of alternating single and double bonds within a molecule. They are composed of discrete molecules held together by weak van der Waals forces [34]

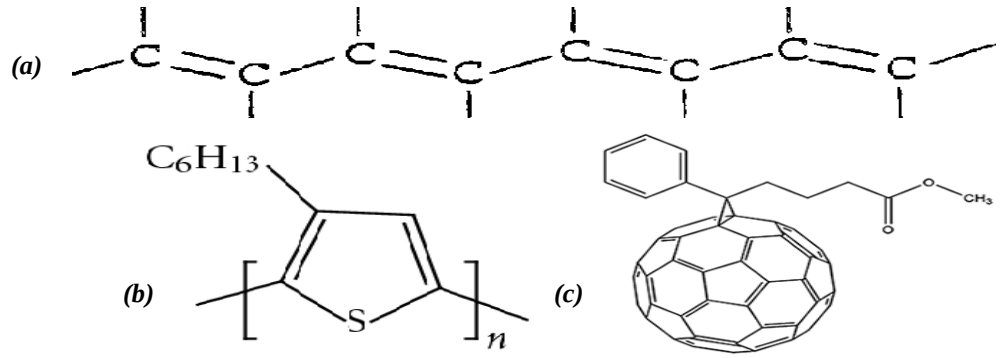


Figure 1.3 a) shows alternating single and double adjacent carbon atoms in conjugated polymer while b) and c) shows The polymer poly (3-hexylthiophene) (P3HT) and the fullerene [6,6]-phenyl-C61 butyric acid methyl ester (PCBM), respectively [35].

In the backbone of a conjugated polymer, each carbon atom binds to only three neighboring atoms. This leaves one electron per carbon atom in a p_z orbital. The mutual overlap between the p_z orbitals results in the formation of π bonds along the conjugated backbone. This leads to delocalized π electrons formed along the entire conjugation path. Due to delocalized π electrons filling up the whole band, conjugated polymers are said to be

intrinsic semiconductors. The filled π band is known as the highest occupied molecular orbital (HOMO) while the empty π* band is the lowest unoccupied molecular orbital (LUMO). This π system can be excited without the chain held together by the σ bonds falling apart. This makes it possible to promote an electron from the HOMO to the LUMO level through light absorption [36]. Conductivity in the polymers is mainly based on the motion of charged defects within the conjugated framework. The charge carriers, either *p*ositive (p-type) or *n*egative (n-type) are the products of oxidizing or reducing the polymer respectively [37].

Polymers have been widely used as acceptor and donor materials. An example of a widely used acceptor is fullerene. These are spherical, ellipsoidal or tube-like carbon molecules [38].

In this thesis, the polymer-fullerene based OPV cell is investigated with poly (3-hexylthiophene) (P3HT) acting as the donor and the fullerene [6,6]- phenyl-C61 butyric acid methyl ester (PCBM) as the acceptor [39]. In its pristine form, P3HT has a hole mobility of 10^{-8} m^2V^{-1} s^{-1} which first decreases when blended with PCBM and subsequently recovers upon annealing [40]. On the other hand PCBM first synthesized by Heeger and coworkers in 1995 has remained a very dominant acceptor material [41].

1.5 **Problem statement**

Organic photovoltaics offer a better potential solution to the exigent energy challenges as well as a means to reducing environmental pollution resulting from reliance on fossil fuel. However, their low photo conversion efficiency remains their greatest drawback that precludes their roll out. Indeed the highest power-conversion efficiency (PQC) reported in literature is 10-12 % which is incomparable to their inorganic counterpart (40 %).

Coupled to this challenge is their stability to air. Organic polymers degrade rapidly when exposed to oxygen this is a feature that greatly limits their commercialization. For the widespread usage of OPVs, high module efficiencies (>10%) and lifetimes suitable for

commercial applications are required. The development of new light-harvesting materials, the improvement of device structures, the development of cost effective device processing methods and modification of the optoelectronic properties of the active layer are crucial to enhancing efficiency as well as the device stability.

1.6 Aim and objective of the study

1.61 Aim

The aim of this project was to fabricate and characterize BHJ organic photovoltaic cell incorporating noble metal (Ag) nanoparticles synthesized in various sizes and shapes obtained by annealing both in air and Argon ambient. The optimum incorporation of the noble metal nanoparticles in the OPV cell structure was pursued to achieve maximum light scattering and absorption by plasmon resonance. In order to study stability of the device, the NPs were encapsulated by thermally evaporated pentacene. This approach provides for presence of multiple absorption peaks and thereby enhance not only stability but also the J_{sc} and efficiency of the device.

1.62 Objectives

- To fabricate a working BHJ OPV (P3HT:PCBM) as a reference solar cell.
- To synthesize and characterize noble metal (Ag and Au) nanoparticles of varied shapes using thin film growth techniques and surface energy variations.
- To optimize the incorporation of noble metal nanoparticles into the OPV cell device for light scattering leading to an improved light absorption.
- Investigate the optoelectronic properties of OPV incorporated with surface Plasmon resonance effect.
- To investigate optical properties of pentacene encapsulated NPs as well stability check on device.

Thesis structure

This thesis has its chapters laid out in the following structure:

Chapter 1 describes the background study of solar energy and the development road map of photovoltaics as well as study on the structure of conjugated polymers.

Chapter 2 describes the basic working principles of Organic solar cells. This includes exciton generation, exciton diffusion to the donor-acceptor heterojunction where dissociation takes place. The production of free electrons and holes, the concept of charge transport and collection are presented briefly in this section. Subsequently the parameters used in solar cells are discussed.

Chapter 3 presents an introduction to the theoretical framework of plasmonic resonance in metal particles. Various applications of surface plasmons as well as mechanisms of absorption in organic solar cells using plasmonic resonance are discussed.

Chapter 4 highlights a brief overview of thin film growth followed by the theoretical description of RF sputtering and thermal evaporation techniques. After outlining the experimental procedure of growing NPs, their morphology and optical properties are characterized using AFM and UV-Vis spectrometer respectively and the results reported.

Chapter 5 discusses the steps used in device fabrication. The efficiency enhancement through thermal annealing is reported as well through incorporation of NPs on top of ITO electrode. The effect on V_{oc}, J_{sc} and FF are also discussed.

Chapter 6 presents the degradation mechanisms in organic solar cell. The degradation trend of OPVs exposed to air is also reported. The results of device encapsulation using pentacene grown through thermal evaporation are also presented.

Chapter 7 gives a summary of most important parts of this thesis.

Reference

[1] Nelson, J. (2003). *The physics of solar cells* (Vol. 1, pp. 1-15). London: Imperial college press.

[2] http://seagerexoplanets.mit.edu/teaching.htm accessed on 10 March 2015 at 12.15 pm.

[3] Eltbaakh, Y. A., Ruslan, M. H., Alghoul, M. A., Othman, M. Y., & Sopian, K. (2013). Measurements of spectral-band solar irradiance in Bangi, Malaysia.*Solar Energy*, *89*, 62-80.

[4] Gueymard, C. A., Myers, D., & Emery, K. (2002). Proposed reference irradiance spectra for solar energy systems testing. *Solar energy*, *73*(6), 443-467.

[5] http://www.unesco.org/bpi/science/content/press/anglo/12.htm accessed on 10 March 2015 at 12.15 pm.

[6] Raupach MR, Marland G, Ciais P, Le Quéré C, Canadell JG, Klepper G, Field CB (2007) Proc Natl Acad Sci USA 104:10288–10293.

[7] Buermann W,Lintner BR , Koven CD , Angert A , Pinzon JE , tucker CJ , Fung IY (200 7) Proc Natl Acad Sci USA 104:4249–4254

[8] Centre for international climate and environmental research (CICERO). "Global warming: Dwindling chances to stay below 2 ^{o}C warming." Science Daily, 21 September 2014. <www.sciencedaily.com/release/2014/09/14092114500.

[9] http://www.sciencedaily.com/releases/2014/09/140921145005.htm accessed on 10 March 2015 at 2.23 pm.

[10] Renewable and Sustainable Energy Reviews 11, (2007) 1388–1413

[11] Renewable and Sustainable Energy Reviews 9, (2005) 444–473

[12] Becquerel, A. E. (1839). Recherches sur les effets de la radiation chimique de la lumière solaire au moyen des courants électriques. *Comptes Rendus de LAcadémie des Sciences*, *9*, 145-149.

[13] Smeeton, T., & Humphreys, C. (2006). Perspectives on electronic and optoelectronic materials. In *Springer handbook of electronic and photonic materials* (pp. 3-15). Springer US.

[14] Spanggaard, H., & Krebs, F. C. (2004). A brief history of the development of organic and polymeric photovoltaics. *Solar Energy Materials and Solar Cells*,*83*(2), 125-146.

[15] Volmer, M. (1913). Different Photoelectric Phenomena in Anthracene, their Relation to one another, to Fluorescence and to the Formation of Dianthracene.*Annalen der Physik*, *40*, 775-96.

[16] Sun, S. S., & Sariciftci, N. S. (Eds.). (2005). *Organic photovoltaics: mechanisms, materials, and devices*. CRC press.

[17] Spanggaard, H., & Krebs, F. C. (2004). A brief history of the development of organic and polymeric photovoltaics. *Solar Energy Materials and Solar Cells*,*83*(2), 125-146.

[18] Weinberger, B. R., Akhtar, M., & Gau, S. C. (1982). Polyacetylene photovoltaic devices. *Synthetic Metals*, *4*(3), 187-197.

[19] Glenis, S., Tourillon, G., & Garnier, F. (1986). Influence of the doping on the photovoltaic properties of thin films of poly-3-methylthiophene. *Thin Solid Films*, *139*(3), 221-231.

[20] Tang CW. 2-layer organic photovoltaic cell. Applied Physics Letters 1986; 48(2): 183–185.

[21] Sariciftci, N. S., Smilowitz, L., Heeger, A. J., & Wudl, F. (1992). Photoinduced electron transfer from a conducting polymer to buckminsterfullerene. *Science*,*258*(5087), 1474-1476.

[22] Yu, G., Gao, J., Hummelen, J. C., Wudl, F., & Heeger, A. J. (1995). Polymer photovoltaic cells: enhanced efficiencies via a network of internal donor-acceptor heterojunctions. *Science-AAAS-Weekly Paper Edition*, *270*(5243), 1789-1790.

[23] Brabec, C. J., Cravino, A., Meissner, D., Sariciftci, N. S., Fromherz, T., Rispens, M. T., ... & Hummelen, J. C. (2001). Origin of the open circuit voltage of plastic solar cells. *Advanced Functional Materials*, *11*(5), 374-380.

[24] Li, G., Shrotriya, V., Huang, J., Yao, Y., Moriarty, T., Emery, K., & Yang, Y. (2005). High-efficiency solution processable polymer photovoltaic cells by self-organization of polymer blends. *Nature materials*, *4*(11), 864-868.

[25] Hiramoto, M., Fujiwara, H., & Yokoyama, M. (1991). Three-layered organic solar cell with a photoactive interlayer of codeposited pigments. *Applied physics letters*, *58*(10), 1062-1064.

[26] Yu, G., Pakbaz, K., & Heeger, A. J. (1994). Semiconducting polymer diodes: Large size, low cost photodetectors with excellent visible-ultraviolet sensitivity.*Applied Physics Letters*, *64*(25), 3422-3424.

[27] Kim, J. Y., Kim, S. H., Lee, H. H., Lee, K., Ma, W. L., Gong, X., & Heeger, A. J. (2006). New architecture for high-efficiency polymer photovoltaic cells using solution-based titanium oxide as an optical spacer.

[28] Chirvase, D., Chiguvare, Z., Knipper, M., Parisi, J., Dyakonov, V., & Hummelen, J. C. (2003). Electrical and optical design and characterisation of regioregular poly (3-hexylthiophene-2, 5diyl)/fullerene-based heterojunction polymer solar cells. *Synthetic Metals*, *138*(1), 299-304.

[29] Crispin, X., Marciniak, S., Osikowicz, W., Zotti, G., van der Gon, A. W., Louwet, F., ... & Salaneck, W. R. (2003). Conductivity, morphology, interfacial chemistry, and stability of poly (3, 4-ethylene dioxythiophene)–poly (styrene sulfonate): A photoelectron spectroscopy study. *Journal of Polymer Science Part B: Polymer Physics*, *41*(21), 2561-2583.

[30] Pettersson, L. A., Ghosh, S., & Inganäs, O. (2002). Optical anisotropy in thin films of poly (3, 4-ethylenedioxythiophene)–poly (4-styrenesulfonate). *Organic electronics*, *3*(3), 143-148.

[31] Seo, J., Kim, W. J., Kim, S. J., Lee, K. S., Cartwright, A. N., & Prasad, P. N. (2009). Polymer nanocomposite photovoltaics utilizing CdSe nanocrystals capped with a thermally cleavable solubilizing ligand. *Applied Physics Letters*,*94*(13), 133302.

[32] Zhou, Y., Riehle, F. S., Yuan, Y., Schleiermacher, H. F., Niggemann, M., Urban, G. A., & Krüger, M. (2010). Improved efficiency of hybrid solar cells based on non-ligand-exchanged CdSe quantum dots and poly (3-hexylthiophene). *Applied Physics Letters*, *96*(1), 013304.

[33] Parnell, A. J., Dunbar, A. D., Pearson, A. J., Staniec, P. A., Dennison, A. J., Hamamatsu, H., ... & Jones, R. (2010). Depletion of PCBM at the cathode interface in P3HT/PCBM thin films as quantified via neutron reflectivity measurements. *Advanced Materials*, *22*(22), 2444-2447.

[34] E. Klimov, W. Li, X. Yang, G.G.Hoffmann, and J. Loos. Scanning near-field and confocal raman microscopic investigation of p3ht-pcbm systems for solar cell applications. Macromolecules, 39(13):4493–4496, 2006

[35] Hoffmann, R., Janiak, C., & Kollmar, C. (1991). A chemical approach to the orbitals of organic polymers. *Macromolecules*, *24*(13), 3725-3746.

[36] Breeze, A. J., Schlesinger, Z., Carter, S. A., & Brock, P. J. (2001). Charge transport in TiO 2/M E H− P P V polymer photovoltaics. *physical review B*,*64*(12), 125205.

[37] Havinga, E. E., Ten Hoeve, W., & Wynberg, H. (1992). A new class of small band gap organic polymer conductors. *Polymer Bulletin*, *29*(1-2), 119-126.

[38] Frederik C. Krebs. Polymeric Solar Cells: Materials, Design, Manufacture. DEStech Publications, Inc., Lancaster, Pennsylvania, 2010.

[39] Knaapila, M., Stepanyan, R., Lyons, B. P., Torkkeli, M., & Monkman, A. P. (2006). Towards general guidelines for aligned, nanoscale assemblies of hairy-rod polyfluorene. *Advanced Functional Materials*, *16*(5), 599-610.

[40] Yu, G., Gao, J., Hummelen, J. C., Wudl, F., & Heeger, A. J. (1995). Polymer photovoltaic cells: enhanced efficiencies via a network of internal donor-acceptor heterojunctions. *Science-AAAS-Weekly Paper Edition*, *270*(5243), 1789-1790.

Chapter 2. Working principles of Organic solar cells

The working principle of organic solar cells is based on photovoltaic effect. This entails the generation of a potential difference at the polymer/fullerene interface as a result of a photo response.

The conversion of light into electricity by an organic solar cell can be described by the following steps:

- Photo-absorption to generate electron-hole pair (exciton).
- Exciton diffusion to the donor acceptor interface.
- Exciton dissociation leading to separate charge carriers.
- Charge transport within the device layers to the respective electrodes [1].

2.1 Photogeneration of charge carriers

Photo absorption by an organic molecule occurs due to the interaction of the oscillating electric field component vector of the light wave with its electrons in the HOMO level. This only takes place for incident light of a particular wavelength (resonance energy). In the event that energy of the photon is higher than the optical band gap, then, excess energy is converted into vibrational and rotational energy (thermalization) within the crystal. It's also possible to experience irradiative energy transfer to a molecule in case of a femtosecond intraband de-excitations upon photo-absorption to excited states. However, absorption usually takes place when the incident photon has sufficient energy to promote a transition. Upon absorption of a photon, the excited molecule exists in the lowest excited singlet state for time scales of the order of nanoseconds before finally relaxing to the ground state [2].

The organic conjugated π-system polymers have low dielectric constant (2-4) but typically, they exhibit high thickness dependent absorption coefficients ($>10^5$ cm^{-1}) within the visible spectrum [3].

According to Gregg *et al.* the production of excitons in OPVs may be attributed to the following:

- Weak interactions between organic molecules compared to strong covalent bonds in inorganic counterparts resulting in spatial restriction to the potential well of corresponding hole.
- Low dielectric constant relative to the dielectric constant of inorganic semiconductors prohibiting the formation of free charge carriers upon photon absorption [4].

The choice of the donor and acceptor material is very crucial as absorber materials of sufficient band gap and thickness should match the solar emission spectrum for efficient light collection.

The probability of absorption of a photon with energy E is described by the absorption coefficient α(E) which varies with the semiconductor used. In organic polymers where absorption results in exciton generation, α(E) is proportional to the density of the HOMO from which a hole is produced, and the density of the LUMO to which the generated electron is excited to. Consider α(E) to be uniform throughout the polymer, then the light intensity emerging out of a glass slab of thickness x is given by:

$$I = I_o \exp(-\alpha x) \qquad 2\text{-}1$$

where I_o is the incident light intensity [5]. P3HT used here as a donor is suitable as its band gap (1.9-2.0 eV) spans within the longer UV and the visible (400nm-650nm) spectrum. It also has a high hole mobility in excess of 10^{-8} $cm^{-1}V^{-1}s^{-1}$. Moreover, it is partially stable to air and soluble (~50 mg/ml) in chlorinated solvents such as chloroform, chlorobenzene, dichlorobenzene and trichlorobenzene. However, P3HT coverage is 30% of the AM1.5 solar photon flux (assuming complete absorption of the solar emission intensity by the material) [3] while the rest of the incident sunlight is wasted. On the other hand PCBM, fullerene based compound, has been used due to its high electron affinity with an electron mobility of ~ 2×10^{-3} $cm^2/V.s$ and superior

ability to delocalize negative charges but a relatively low absorptivity in the wavelength range of 400 to 700 nm [6]. From this discussion, the P3HT - PCBM blend despite having nearly insignificant series resistance less than 5 Ωcm^2 for devices with active layer thinner than 100 nm [7], fails to achieve a high PCE due to inefficient usage of incident light. We thus propose to increase the absorption spectrum in the inaccessible regions to increase the higher short circuit current density and open circuit voltages. This is done using surface Plasmon resonance effect.

2.2 Exciton diffusion

The photogenerated exciton has to travel a distance of the order of 10 nm to the interface for dissociation [8-9]. This is the exciton diffusion length which predicates on the thickness of the active layer of the OPV. There are two general mechanisms through which exciton diffusion takes place in thin organic polymer films, namely:

- Through Förster transfer mechanism. The lack of molecular interaction in organic semiconductors influences exciton transport, which according to Förster resonance energy transfer (FRET) theory occurs through a hopping mechanism. For singlet excitons, the rate of energy transfer between the molecules, K_{ET} is proportional to the electronic coupling, V, and inversely proportional to the sixth power of inter-molecular distance, $R_{DA.}$

$$K_{ET} \propto V^2 = \frac{\mu_D{}^2 \mu_A{}^2}{R_{DA}{}^6} \qquad 2\text{-}2$$

Where μ_A is the transition dipole moments of the acceptor (A), μ_D is the transition dipole moments of the donor (D). Photoexcitation of one polymer causes a change in the motion of the π-electrons thus altering the charge distribution inside the molecule. This results in a temporal electric dipole in the excited molecule. For two molecules adjacent to one another the temporal electric dipole can induce a dipole of same magnitude in the neighbouring molecule at ground state. As the originally excited electron relaxes, its energy may be transferred

through dipole-dipole interaction to the adjacent molecule at ground state resulting in the original molecule returning to the ground state without radiative relaxation while the adjacent molecule is being excited without absorbing a photon. This mechanism allows for excitation of singlet energy of a polymer from one chain to another. This process is also called singlet exciton diffusion

- The Dexter exchange mechanism.

This mechanism involves the diffusion of triplet excitons by Dexter exchange. Triplet excitons are formed as a result of intersystem crossing of a photoexcited system. The formation of triplets in organic molecules is a forbidden process due to electron spin momentum conservation [10].

If an exciton is not separated within its lifetime usually in picosecond time scale, the electron-hole pair simply recombines [8-9]. An efficient solar cell should have the majority of excitons reaching the interface within the exciton lifetime (τ_{exc}). The diffusion length L_{exc} is related to the exciton lifetime and the diffusion coefficient D_{exc} of the excitons according to the expression,

$$L_{exc} = \sqrt{D_{exc}\tau_{exc}} \qquad 2\text{-}3$$

For molecular materials τ_{exc} is several picoseconds and L_{exc} is about 10 nm [11].

In 1992 Sariciftci *et al*. demonstrated that ultrafast electron transfer takes place from a conjugated polymer to the PCBM, showing the great potential of fullerenes as acceptor materials [12]. The small diffusion length limits the thickness of the active layer contributing to photocurrent to a very thin region near the donor/acceptor junction while the excitons generated in the remainder of the device are lost.

In the BHJ used in this work, the polymer-fullerene blend ensures that the correlation length scales with the exciton diffusion length to enable most of the excitons generated diffuse to the interface and separate efficiently [13-14].

Huijser et al. using analysis of the incident photon to current efficiency (IPCE) for P3HT and porphyrin-based bilayer reported a diffusion length of 18 nm for P3HT [15]. However, this value includes energy transfer between the P3HT and the porphyrin, which can greatly enhance exciton harvesting [16- 17].

2.3 Exciton dissociation

Exciton dissociation occurs at the interface (heterojunction) of two materials provided the offset between their bandgaps is greater than the exciton's binding energy. A typical exciton binding energy is of the order of 0.25–1 eV [18]. This is the minimum energy required to dissociate the exciton. Thermal energy (~25meV) and electrical (electric field) energy are therefore insufficient under normal operating conditions to dissociate the exciton, and instead the chemical potential difference between two organic semiconductors is utilized [19-20]. The probability of charge transfer is 100% as long as the energy offset between the LUMO of the donor and acceptor is greater than 0.3 eV. This energy provides sufficient electric field to enable exciton dissociation. The energetic driving force for separating the positive (holes) and negative (electrons) charges relies in the difference between the LUMO levels of the donor and acceptor.

The exciton dissociation efficiency is a function of the heterointerface area and the ability of the exciton to diffuse to this interface [21]. To maximize exciton dissociation, a large heterointerface is needed. This is normally achieved by the use of BHJ cells. Once the exciton is dissociated, the electron and hole still experience significant Coulomb attraction and

although structurally separated, they remain in a bound state with a finite lifetime. This bound state is commonly referred to as a charge-transfer (CT) state [22-23].

2.4 Charge collection

Once dissociation has taken place at the donor – acceptor interface, the holes and electrons hop through the p-type and n-type material, respectively. To reach the electrodes, the charge carriers need a net "force": This is provided by internal electric field and the concentration gradient of the respective charge carrier species. The first leads to a field – induced drift and the second to a diffusion current [24-27].

Since the performance of OSCs greatly depends on the interfaces between the various layers, it is necessary to minimize the energy barrier between the electrodes and the organic layers so as to achieve a nearly Ohmic contact. Different interfacial layers between the electrodes and the organic layers have been used to improve charge collection and reduce surface recombination. Such interfacial layers include poly(3,4- ethylenedioxy thiophene): poly(styrenesulfonate) (PEDOT:PSS), MoO_3, V_2O_5, and NiO_x for efficient hole collection. On the other hand LiF , CsF, Cs_2CO_3 and TiO_x interlayers deposited between the organic layers and the cathode have been reported to enhance electron collection [28].

In this thesis the transparent conducting substrate (ITO) used for holes collection is spin coated with PEDOT: PSS in an aqueous solution. The PEDOT:PSS layer improves the surface quality of the ITO electrode (reducing the probability of shorts) as well as facilitates the hole injection/extraction. Furthermore, the work function of this electrode can be changed by chemical/electrochemical redox reactions of the PEDOT layer. On the other hand thermally evaporated Aluminum thin film of a lower work function compared to ITO is used for electron collection [29]. The summary of the operative overview of the device is as shown in figure 2.1.

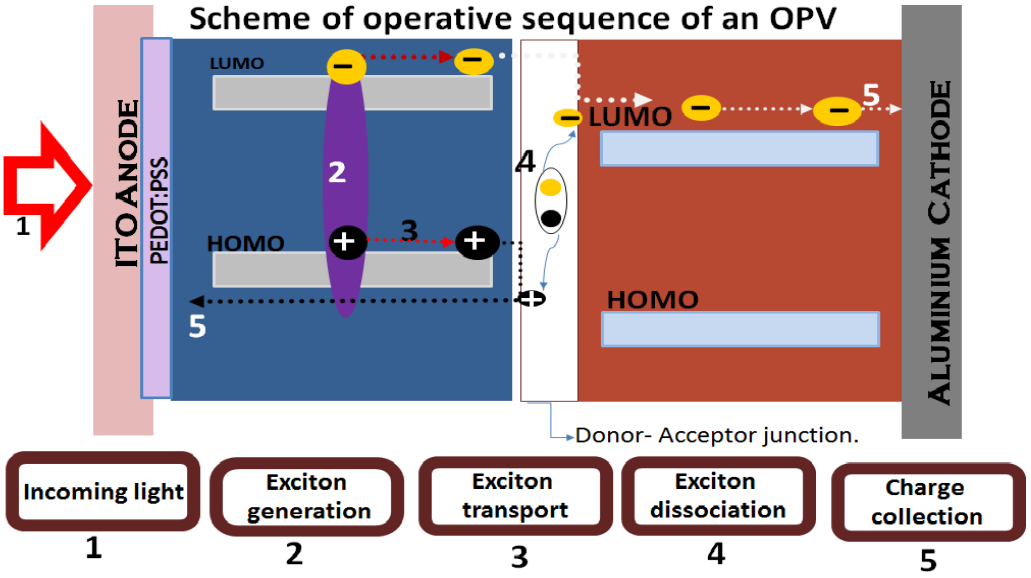


Fig 2.1 Schematic diagram of the photocurrent generation mechanism in organic photovoltaic devices.

2.5 Parameters used in solar cell

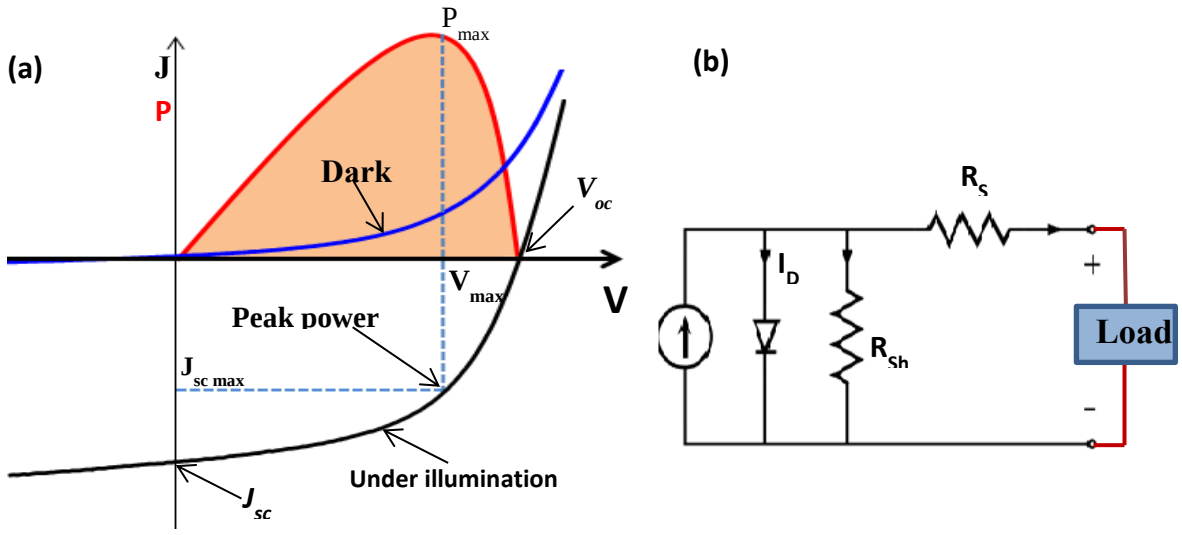


Figure 2.2 a) The J-V characteristics of solar cell in the dark and under illumination b) equivalent circuit diagram.

The main parameters used in characterization of solar cell performance include; peak power P_{max}, short circuit current density, J_{sc}, open circuit voltage, V_{oc}, fill factor *FF etc*. These parameters are obtained from the illuminated as well as dark J-*V* characteristic as illustrated in Fig 2.2. The power conversion efficiency is derived from these parameters.

2.51 *Short circuit current*

This is the current flowing through the external circuit in the absence of a load (current when voltage equals zero). Short circuit current is determined by the photon flux density incident on the solar cell which depends on the spectrum of the incident light. For the standard solar cell measurements, the spectrum is standardized to the AM1.5 spectrum. The current density is roughly proportional to the area of the solar cell. The maximum current that can be delivered by the solar cell mainly depends on the optical properties of the cell which include absorption of the active layer and reflection from the back end electrodes.

When a load is connected across the terminals of the cell as shown in Fig 2.2 b, the current decreases as charges accumulate at the terminals. The resulting current is a superposition of short circuit current resulting from absorption of photons and the dark current. Dark current is caused by the potential across the load when the device is not illuminated and it flows in the opposite direction [30]. Considering solar cell as an ideal diode with an ideality factor of 1, the dark current density is given by:

$$J_{dark}(V) = J_O(e^{qV/K_BT} - 1) \qquad 2\text{-}4$$

Where J_o is a constant, q is electron charge while V is voltage across the terminals. The resulting current, approximated as a superposition of dark and short circuit current is given by:

$$J = J_{SC} - J_O(e^{qV/K_BT} - 1) \qquad 2\text{-}5$$

2.52 Open circuit voltage

This is the voltage between the terminals when no current is drawn (infinite load resistance). $\boldsymbol{V_{oc}}$ corresponds to the forward bias voltage when the photocurrent is compensated by the dark current and it gives the maximum voltage that a solar cell can deliver.

At $\boldsymbol{V_{oc}}$ the two currents cancels out such that no current flows resulting in:

$$V_{OC} = \frac{K_B T}{q} \ln\left(\frac{J_{sc}}{J_o} + 1\right) \qquad 2\text{-}6$$

From the above equation, $\boldsymbol{V_{oc}}$ is dependent on the dark current J_o, the photo-generated current J_{sc} and the temperature under which the device is subjected to. Studies on BHJ have shown that the open-circuit voltage depends on the energy difference between the highest occupied molecular orbital (HOMO) level of the donor and the lowest unoccupied molecular orbital (LUMO) level of the acceptor so long as there is a good electrical contact at the electrode-organic layers interface. The HOMO level is approximated as the ionization potential of the donor while the LUMO as the electron affinity of the acceptor molecules.

2.53 Fill factor

The fill factor is the ratio of maximum power generated to the product of V_{oc} and J_{sc}. It gives a measure of how much of the open circuit voltage and short circuit current is utilized at maximum power.

$$FF = \frac{J_{\max} V_{\max}}{J_{sc} V_{oc}} \qquad 2\text{-}7$$

Fill factor (FF) of a solar cell may be termed as the quality of the cell. It reflects the ability of the photogenerated charge carriers to be collected by the respective contacts. FF is influenced by many factors interplaying with each other intricately namely;

- The level of the LUMO of the acceptor and donor that determines the nature of the V_{oc} and hence the fill factor.

- The series and shunt resistances which have a pronounced effect on the shape of *J–V* curve around V_{oc} and Jsc respectively hence affecting the 'square' shape of the *J-V* curve.

Usually, there is a competition between charge extraction and recombination which are both mediated by the mobility of carriers in the device. Though high mobility is necessary to ensuring efficient exciton dissociation and transport of carriers, it may lead to charge recombination hence the need for optimization to ensure maximum FF. However, limiting the minority surface recombination by keeping a low Ohmic contact at the active layer- electrode interface will allow maximum FF despite high carrier mobility [31-34].

Since most organic semiconductors have very low mobility (e.g., 10^{-5} – 10^{-3} $cm^2 \cdot V^{-1} \cdot s^{-1}$) [35-36], they experience inefficient charge extraction. Various approaches have been adopted to improve the carrier mobility in the OPV materials. One approach involves increasing the nanoscale crystallinity and molecular packing of the polymer film through controlled annealing conditions [37-38].

2.54 power conversion efficiency PCE

The power conversion efficiency is defined as the ratio of output power (maximum generated power) to incident power P_{in} expressed as a percentage. The AM1.5 spectrum ($100W/m^2$) has been used as a standard reference for measuring the power conversion efficiency of solar cells according to the expression;

$$\eta = \frac{P_{\max}}{P_{in}} = \frac{J_{\max} V_{\max}}{J_{sc} V_{oc}} = \frac{J_{sc} V_{oc} FF}{P_{in}} \qquad 2\text{-}8$$

According to Kirchartz et al. the maximum theoretical efficiency for OPVs is calculated to be above 20% [39]. This huge disparity with the experimental value may be attributed to:

- Optical losses; when part of the incident light absorbed by materials are not involved in charge carrier production.

- Exciton losses; due to part of excitons failure to reach the donor/acceptor interfaces.
- Recombination losses– charge carriers recombine at film defects or interfaces.
- Collection losses– charge carrier mobility is insufficient to ensure that the charge carriers reach the electrodes.

By far the greatest loss mechanism is the exciton recombination at donor/acceptor interfaces resulting from mismatched energy levels between donor and acceptor.

2.55 Parasitic resistances

The power in a solar cell device is normally dissipated through contact resistance and the leakage current. These effects are equivalent electrically to parasitic resistances in (i) series and (i) parallel as shown in figure 2.3.

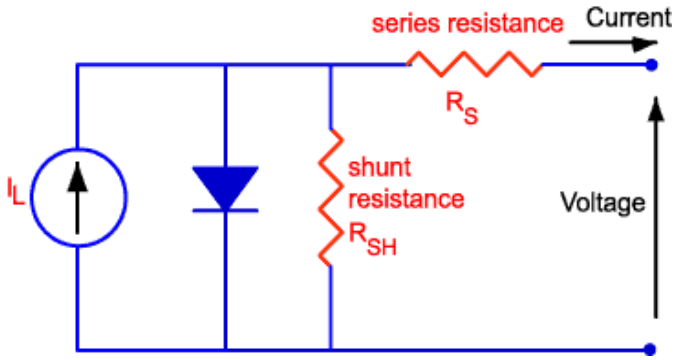


Figure 2.3 Equivalent circuit for parasitic series and shunt resistances in a solar cell circuit.

The series resistance $R_{s,}$ arises from cell material particularly through the front surface of the contacts. In *I-V* graph series resistance is derived from inverse of slope at $V_{oc.}$

On the other hand parallel or shunt resistance, R_{sh} arises from leakage of current through the cell. It is represented by the inverse of slope at I_{sc} in *I-V* graph.

For an ideal cell, R_{sh} should be infinite and would not provide an alternate path for current to flow, while R_S would be zero, resulting in no further voltage drop before the load.

Decreasing R_{sh} and increasing R_s reduces the fill factor (FF) (shown in figure 2.4) and subsequently a reduction in P_{max}. If R_{sh} is decreased too much, V_{oc} will drop, while increasing R_S excessively can cause I_{sc} to drop instead.

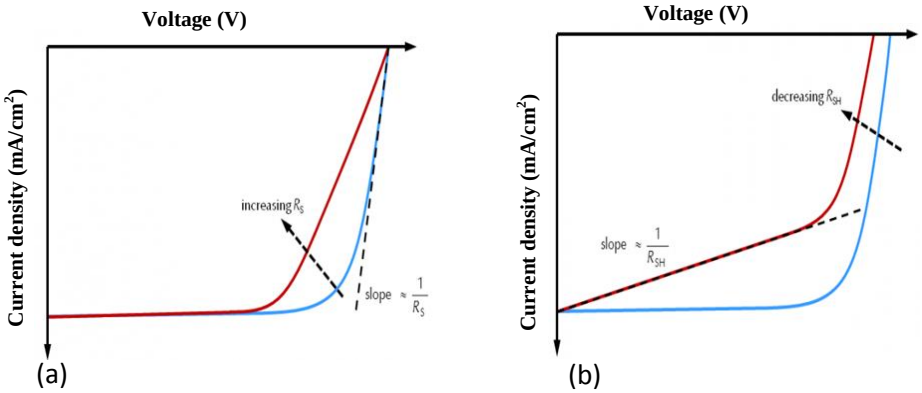


Figure 2.4 a-b) The effect of parasitic series and shunt resistance (R_s and R_{sh}) on a solar cell's I-V curve adapted from [40].

Reference

[1] Günes, S., Neugebauer, H., & Sariciftci, N. S. (2007). Conjugated polymer-based organic solar cells. *Chemical reviews*, *107*(4), 1324-1338.

[2] Perepichka, I. F., Perepichka, D. F., Meng, H., & Wudl, F. (2005). Light-emitting polythiophenes. *Advanced Materials*, *17*(19), 2281-2306.

[3] Günes, S., Neugebauer, H., & Sariciftci, N. S. (2007). Conjugated polymer-based organic solar cells. *Chemical reviews*, *107*(4), 1324-1338.

[4] Gregg, B. A., & Hanna, M. C. (2003). Comparing organic to inorganic photovoltaic cells: Theory, experiment, and simulation. *Journal of Applied Physics*, *93*(6), 3605-3614.

[5] Würfel, P., & Würfel, U. (2009). *Physics of solar cells: from basic principles to advanced concepts*. John Wiley & Sons.

[6] http://www.sciencemag.org/content/295/5564/2425.full.pdf accessed on 10 March 2015 at 12.18 pm.

[7] Shen, Yang, and Mool C. Gupta. "Investigation of electrical characteristics of P3HT: PCBM organic solar cells." *Photovoltaic Specialists Conference (PVSC), 2012 38th IEEE*. IEEE, 2012.

[8] M. Pope and C. E. Swenberg, *Electronic processes in organic crystals and polymers*, 2nd ed. (Oxford University Press, 1999).

[9] Hill, A. Kahn, Z. G. Soos, and R. A. Pascal, "Charge-separation energy in films of P-conjugated organic molecules," Chem. Phys. Lett. 327, 181–188 (2000).

[10] Vella Jr, Jarrett H. *Singlet and triplet excitons in organic and organometallic thin films: Diffusion and triplet sensitization*. University of Florida, 2009.

[11] Vacar, D., Maniloff, E. S., McBranch, D. W., & Heeger, A. J. (1997). Charge-transfer range for photoexcitations in conjugated polymer/fullerene bilayers and blends. *Physical Review B*, *56*(8), 4573.

[12] Sariciftci, N. S., Smilowitz, L., Heeger, A. J., & Wudl, F. (1992). Photoinduced electron transfer from a conducting polymer to buckminsterfullerene. *Science*,*258*(5087), 1474-1476.

[13] Shajing S, Sariciftci N, Mechanisms, materials and devices Taylor &Francis Group CRC press.2005

[14] Forrest, S. R. (2005). The limits to organic photovoltaic cell efficiency. *MRS bulletin*, *30*(01), 28-32.

[15] Huijser, A., Savenije, T. J., Shalav, A., & Siebbeles, L. D. (2008). An experimental study on the molecular organization and exciton diffusion in a bilayer of a porphyrin and poly (3-hexylthiophene). *Journal of Applied Physics, 104 (3), 2008*.

[16] Scully, S. R., & McGehee, M. D. (2006). Effects of optical interference and energy transfer on exciton diffusion length measurements in organic semiconductors. *Journal of applied physics*, *100*(3), 034907.

[17] Scully, S. R., Armstrong, P. B., Edder, C., Frechet, J. M., & McGehee, M. D. (2007). Long-range resonant energy transfer for enhanced exciton harvesting for organic solar cells. *Advanced materials-deerfield beach then weinheim-*, *19*(19), 2961.

[18] Gregg, B.A.; Hanna, M.C. Comparing organic to inorganic photovoltaic cells: Theory, experiment, and simulation. J. Appl. Phys. 2003, 93, 3605–3614.

[19] Gregg, B.A. The photoconversion mechanism of excitonic solar cells. MRS Bull. 2005, 30, 20–22.

[20] G¨unes, S.; Neugebauer, H.; Sariciftci, N.S. Conjugated polymer-based organic solar cells. Chem. Rev. 2007, 107, 1324–1338.

[21] Li, G.; Zhu, R.; Yang, Y. Polymer solar cells. Nat. Photonics 2012, 6, 153–161.

[22] Clarke, T.M.; Durrant, J.R. Charge photogeneration in organic solar cells. Chem. Rev. 2010,110, 6736–6767.

[23] Imahori, H.; Guldi, D.M.; Tamaki, K.; Yoshida, Y.; Luo, C.; Sakata, Y.; Fukuzumi, S.Charge separation in a novel artificial photosynthetic reaction center lives 380 ms. J. Am. Chem. Soc. 2001, 123, 6617–6628.

[24] Koster, L. J. A., Smits, E. C. P., Mihailetchi, V. D., & Blom, P. W. M. (2005). Device model for the operation of polymer/fullerene bulk heterojunction solar cells. *Physical Review B*, *72*(8), 085205.

[25] Kirchartz, T., Pieters, B. E., Taretto, K., & Rau, U. (2008). Electro-optical modeling of bulk heterojunction solar cells. *Journal of applied physics*, *104*(9), 094513.

[26] Deibel, C., Wagenpfahl, A., & Dyakonov, V. (2008). Influence of charge carrier mobility on the performance of organic solar cells. *physica status solidi (RRL)-Rapid Research Letters*, *2*(4), 175-177.

[27] Häusermann, R., Knapp, E., Moos, M., Reinke, N. A., Flatz, T., & Ruhstaller, B. (2009). Coupled optoelectronic simulation of organic bulk-heterojunction solar cells: Parameter extraction and sensitivity analysis. *Journal of Applied Physics*, *106*(10), 104507.

[28] Xiao, T. (2012). Modifying the organic/electrode interface in Organic Solar Cells (OSCs) and improving the efficiency of solution-processed phosphorescent Organic Light-Emitting Diodes (OLEDs).

[29] Günes, S., Neugebauer, H., & Sariciftci, N. S. (2007). Conjugated polymer-based organic solar cells. *Chemical reviews*, *107*(4), 1324-1338.

[30] Huang, Y. N. (2012). Semi-transparent ZnO: Al/Cu2O Thin-film Heterojunction Fabricated At Low Temperature: Effect Of An Intrinsic ZnO Buffer Layer At The Junction.

[31] Mauer, R., Howard, I. A., & Laquai, F. (2010). Effect of nongeminate recombination on fill factor in polythiophene/methanofullerene organic solar cells. *The Journal of Physical Chemistry Letters*, *1*(24), 3500-3505.

[32] Tress, W., Petrich, A., Hummert, M., Hein, M., Leo, K., & Riede, M. (2011). Imbalanced mobilities causing S-shaped IV curves in planar heterojunction organic solar cells. *Applied Physics Letters*, *98*(6), 063301.

[33] Qi, B., & Wang, J. (2013). Fill factor in organic solar cells. *Physical Chemistry Chemical Physics*, *15*(23), 8972-8982.

[34] Potscavage Jr, W. J., Yoo, S., & Kippelen, B. (2008). Origin of the open-circuit voltage in multilayer heterojunction organic solar cells. *Applied physics letters*,*93*(19), 193308.

[35] Garcia-Belmonte, G., Munar, A., Barea, E. M., Bisquert, J., Ugarte, I., & Pacios, R. (2008). Charge carrier mobility and lifetime of organic bulk heterojunctions analyzed by impedance spectroscopy. *Organic Electronics*,*9*(5), 847-851.

[36] Tanase, C., Meijer, E. J., Blom, P. W. M., & De Leeuw, D. M. (2003). Unification of the hole transport in polymeric field-effect transistors and light-emitting diodes. *Physical Review Letters*, *91*(21), 216601.

[37] Chu, C. W., Yang, H., Hou, W. J., Huang, J., Li, G., & Yang, Y. (2008). Control of the nanoscale crystallinity and phase separation in polymer solar cells.*tandem*, *11*, 12.

[38] Ray, B., Khan, M. R., Black, C., & Alam, M. A. (2013). Nanostructured electrodes for organic solar cells: Analysis and design fundamentals.*Photovoltaics, IEEE Journal of*, *3*(1), 318-329.

[39] Kirchartz, T., Pieters, B. E., Taretto, K., & Rau, U. (2008). Electro-optical modeling of bulk heterojunction solar cells. *Journal of applied physics*, *104*(9), 094513.

[40] National Instruments. Part ii – photovoltaic cell i-v characterization theory and labview analysis code. Development Zone, URL: http://zone.ni.com/devzone/cda/tut/p/id/7230

Chapter 3: Nanoparticle plasmonics.

3.1 Brief overview.

The free electrons in a metal may be considered electron plasma. In this case a plasmon is a quasiparticle resulting from the quantization of plasma oscillations of the free electron gas density with respect to the fixed positive ions. Plasmons are Bosons. Polaritons on the other side are bosonic (quasi-) particles resulting from strong coupling of electromagnetic waves with an electric or magnetic dipole-carrying excitation (not to be confused with the polaron, which is a fermion). At the point where the two dispersion relationships of light and excitation are crossing each other they have the same energy and therefore coupling occurs [1].

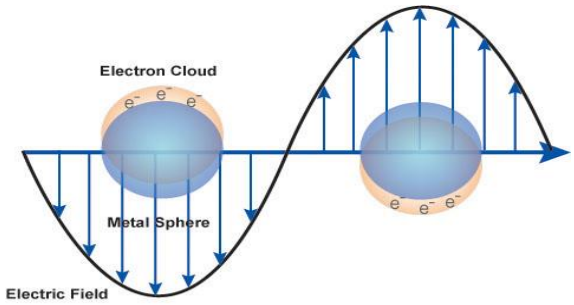


Figure 3.1 Surface plasmon resonance where the free electrons in the metal nanoparticle are driven into oscillation. Reproduced from ref. [2]

The intensive research in nanometer-scale metal particles is driven by their large number of potential applications such as ultrafast optical switches, optical tweezers, labels for biomolecules, optical filters, biosensors, surface enhanced spectroscopies, plasmonics, and chemical sensors. A number of these applications require that the nanoparticles be in metal island film form supported on a substrate. These applications exploit the size- and shape-dependent nature of the optical properties of nanoparticles. Optical absorption and scattering by metal nanoparticles result from the collective oscillation of the free electrons gas known as surface plasmons.

This phenomenon of plasmonic effect is only observed in nanoscale metallic particles with radius smaller than the incident wavelength, λ, such that any applied fields can be considered uniform across a particle. The induced electric field around nanoparticles may be much greater than the incident electromagnetic field by several orders of magnitude [2].

The genesis of SPs goes back to 1908 when Gustav Mie came up with a rigorous theoretical treatment on the optical properties of metallic colloids [3]. This was the first scientific explanation despite evidences from ancient civilization showing the use of metal nanoparticles. The most documented example is the Roman glass cage cup (Lycurgus cup) which appear red or green when illuminated from inside or outside, respectively. This occurrence is attributed to the presence of metallic nanoparticles in the glass.



Figure 3.2 The green Lycurgus cup containing tiny amount of metal nanoparticles (MNPs) giving it this unusual optical characteristic [3].

3.2 Localized surface plasmons.

Localized surface plasmons (LSPs) can be described as charge density oscillations which are confined to metallic nanoparticle and nanostructures. LSPs are excited by incident electromagnetic field at an incident wavelength when the two fields are at resonance (Fig 2.1 b). This results into: strong light scattering, appearance of intense surface plasmon (SP) absorption bands as well as enhancement of local electromagnetic fields. Localized surface plasmons (LSPRs) are non-propagating and can be excited directly by an incoming electromagnetic field that matches the energy of an oscillation [4]. The energy of LSPRs is determined by the type of material used, dielectric environment as well as size and shape of nanostructure.

Locally enhanced electromagnetic fields around the particles are perfectly suited for enhancing optical processes such as Surface Enhanced Raman Scattering (SERS) and fluorescence. Other applications include lenses for high resolution near field optical lithography, antennas for directing light emission or for light harvesting where the optical cross-section is increased [6].

3.3 Surface plasmon polaritons

Surface plasmon polaritons (SPPs) are electromagnetic waves propagating alongmetal/dielectric interface. They occur when incident electromagnetic field is coupled to theoscillation of the electron plasma in the metal. This only occurs when wave vector of the incident electromagnetic wave matches that of the SPPs for the same angular frequency, ω.

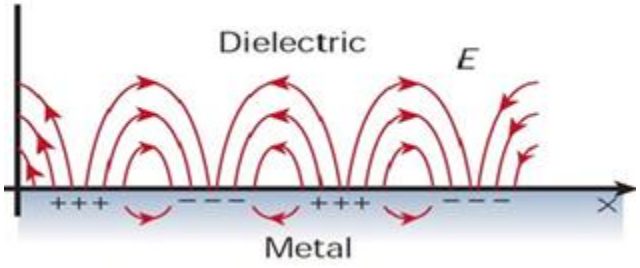


Figure 3.3 Schematic representation of surface plasmon resonance effect along metal/dielectric interface [7].

In contrast to localized modes seen with particles, surface plasmon polaritons whose modes are associated with a planar interface are usually extended in nature and they may propagate to a few tens of micrometres. As a result a lot of research has been ongoing on SPP as a means of providing stronger integration of optical signals compared to the currently obtained from the use of dielectric light-guides [7].

When a beam of light is incident onto a particle, part of the electromagnetic wave is absorbed while other part is scattered in form of a new radiation. The amount of scattered/absorbed by a particle as well as the angular distribution of the scattered light all varies with particle characteristics such as shape, size, dielectric environment and material properties. These characteristics determine the scattering/ absorption cross section. The scattering/ absorption cross section refers to the area in which all incident photons are absorbed or scattered. The sum of scattering and absorbing areas is called extinction cross-section [8].

The characteristic color and brightness of a given particle, and its experimentally observable transmission spectrum, are often expressed as the "cross sections" for extinction, absorption, and scattering (C_{ext}, C_{abs}, C_{sca}, respectively). In the dipole approximation these are very simply related to the quasistatic polarizability α by the optical theorem of wave scattering [9].

The absorption and scattering cross-section of metal nanoparticles with much smaller diameter well below the wavelength of light can be described using point dipole model [10].

The scattering and absorption cross-section are given respectively by the equations [11-12];

$$C_{scat} = \frac{1}{6\pi}\left(\frac{2\pi}{\lambda}\right)^4 |\alpha|^2 \qquad 2\text{-}1$$

$$C_{abs} = \frac{2\pi}{\lambda}\mathrm{Im}[\alpha] \qquad 2\text{-}2$$

Where $\alpha = 3V\left(\frac{\varepsilon_P/\varepsilon_m - 1}{\varepsilon_p/\varepsilon_m + 2}\right)$ 2-3

$C_{ext} = C_{sca} + C_{abs}$. 2-4

Where α is the polarizability of the particle, V is the particle volume, ε_p is the dielectric function of the particle and ε_m is the dielectric function of the embedding medium. At surface plasmon resonance $\varepsilon_p = -2\varepsilon_m, \alpha = \infty$, Normally noble metals give a higher extinction cross-section which may be up to ten times the geometrical cross-section of the metal nanoparticles [14]. They are thus said to be more efficient.

At the excitation of surface plasmons, a peak is observed on the absorption spectrum of metal nanoparticles. The absorbed light provides required energy to take electrons to the excited states. Among metals, silver and gold are the two most often used for plasmonic applications due to their relatively low loss in the visible and NIR ranges.

3.4 Applications of nanoparticle plasmon resonance

Plasmonic nanoparticles have gained a lot of research interest due to their specific optical properties which make them have wide applications. Some of which are discussed below:

Spectroscopic technique

Since plasmonic nanoparticles have a greater enhanced electric field around them compared to the incident light, they can be used in various spectroscopic techniques, where the signal generated is proportional to the electric field and in many occasions in powers of 2-4. Such techniques include fluorescence which usually aid in detection and studying organic especially biological molecules. This is achieved when a fluorescent or a fluorescently labelled molecule placed close to a plasmonic nanostructure substantially gains efficient optical excitation/de-excitation and in turn giving fluorescence as well as enhancing fluorescence

intensity. The interparticle spacing leads to strong local electric fields even to a factor of 1340 [14-15].

Raman spectroscopy

Raman spectroscopy and infrared spectroscopy is a technique used for studying molecular vibrational modes. Plasmonic nanostructures can be used in enhancing the signal upto 10^{12} at plasmonic resonance [16]. Moreover plasmon enhanced Raman scattering enable for detection of a single molecule due to its high sensitivity making it possible to study processes inside a living cell [15, 17].

Imaging of living tissue and detection of diseases.

This is normally done using optical markers such fluorescent dyes as well as quantum dots. However they face challenges for instance dyes are highly susceptible to photobleaching while quantum dots are likely to be toxic. The optical markers may also interfere with the function of the molecules being detected hence the discovery of plasmonic nanoparticles for label free sensing is a great reprieve as they do not show any sign of photobleaching and are relatively non-toxic[14]. Plasmonic nanostructures allows for signal detection by either optical means through light scattering or by thermal means due to light absorption in the particle leading to increased local temperature.

Heating of nanoparticles upon resonant absorption of light is also applicable for treatment of diseases. To achieve this, plasmonic nanoparticles are selectively introduced through illumination to increase the temperature. This can be lethal for the cells but can be used to thermally release chemotherapeutic drugs attached to the plasmonic nanoparticles hence obtaining a local release function [15].

3.5 Plasmonics for organic solar cells

The use of NPs to enhance efficiency in photovoltaics was first carried out on organic and dye sensitized solar cells. In 1991 Hayashi *et al*. reported an enhanced efficiency of organic solar cells using surface plasmons excited in metal contacts of a cell [18]. The use of localized plasmon excitation in metal clusters was first performed by Stenzel et al in 1995. In their report Cu metal clusters performed better than Ag and Au particles. They attributed this to intensified near-field around the particles [19]. However, Westphalen *et al* attributed this performance to generation of excitons in the metal clusters which inject electron into the circuit. Since then quite a number of research groups have dedicated their efforts to developing efficient organic plasmonic based solar cells [20-23]. It is capable of enhancing absorption of organic solar cell within a small thickness of the active layer. Hägglund et al showed by theoretical approaches that it is possible to attain a maximum efficiency of 12 % through the use of Ag nanoparticles using an absorbing layer of only 6 nm thick [24]. Changjun et al. on the other hand predicted an enhanced overall optical absorption in the organic layers by up to 50% in thin-film organic solar cells when the top transparent electrode is partially substituted by a periodic metallic grating [25].

3.6 Mechanisms of absorption enhancement by plasmonic resonance

The enhancement of light absorption in solar cells takes place in four different ways:

- ***Scattering of light into the active layer***

At resonance frequency, the noble metal nanoparticles may be used as a subwavelength scattering elements to couple and trap freely propagating plane waves from the sun into the active layer by folding the light into the thin layer. This will lead to an increased effective path length in the active layer. For a nanoparticle surrounded by a homogenous medium, light scattering is nearly symmetric in forward as well as backward directions. However with an

introduction of a different media of a higher dielectric constant around the nanoparticles, the scattering would most likely be into the medium with high dielectric constant. Even though scattering efficiency increases with particle size, it has been shown that small particles are more efficient in scattering in the forward direction [26].

- ***Through enhanced electric field***

The strong local field enhancement makes metal nanoparticles act as subwavelength antennas in which the plasmonic near field is coupled to the active layer increasing the probability of electron excitations which is proportional to the square of electric field, hence effective absorption cross-section. This ensures that the incident energy is stored in a localized surface plasmon mode on a femtosecond timescale [27].

According to Hägglund *et al* the use of enhanced near-fields is to absorb a substantial light energy within an active layer as thin as 10-20 nm which make the phenomena quite appropriate for thin film organic solar cell with small exciton diffusion length [24].

- ***Creation of electron-hole pair within the plasmonic nanoparticle***

Excitations at plasmons resonance may decay by exciting an electron-hole pair within the nanoparticle itself. If the nanoparticle work function matches the conduction band of the semiconductor then the created electron may be transferred to the conduction band of the semiconductor. This makes the nanoparticle charged and may add to the solar cell current provided the particles are not electrically isolated. However White et al. showed that solar cells based on plasmon-enhanced internal photoemission faces severe efficiency limits due to the properties of metallic absorbers, with maximum theoretical efficiencies of 7% predicted even with perfect optical absorption. This is attributed to schottky barrier formed between metal

nanoparticle and the semiconductor. These excited electrons may not have sufficient energy to overcome the schottky barrier. Thus, the key to improving the efficiency lies in modifying the density of state of the absorber, but this may be difficult to achieve in practice. In the short term, plasmon-enhanced internal photoemission may offer more benefits for Schottky junction photodetectors where increased optical absorption is important for improved performance [28].

- ***Formation of propagating surface plasmons excited at the rear metal film.***

Propagating surface plasmon polariton (SPP) may be excited metal/dielectric interface at the rear of the solar cell. This leads to formation of electromagnetic waves that travel along the interface between the metal back contact and the active layer (Surface plasmon resonance). This can efficiently trap and guide light into the active layer. In this way the incident photon flux is effectively turned by 90^{o} making light to be absorbed along the lateral direction which has larger dimensions compared to the absorption length [25].

Reference

[1] Pitarke, J. M., Silkin, V. M., Chulkov, E. V., & Echenique, P. M. (2007). Theory of surface plasmons and surface-plasmon polaritons. *Reports on progress in physics*, *70*(1), 1.

[2] Hutter, E., & Fendler, J. H. (2004). Exploitation of localized surface plasmon resonance. *Advanced Materials*, *16*(19), 1685-1706.

[3] Lee, J. Y., & Peumans, P. (2010). The origin of enhanced optical absorption in solar cells with metal nanoparticles embedded in the active layer. *Optics Express*, *18*(10), 10078-10087.

[4] Maier, S. A. (2007). *Plasmonics: fundamentals and applications*. Springer Science & Business Media.

[5] Kelly, K. L., Coronado, E., Zhao, L. L., & Schatz, G. C. (2003). The optical properties of metal nanoparticles: the influence of size, shape, and dielectric environment. *The Journal of Physical Chemistry B*, *107*(3), 668-677.

[6] Schmidt, T. M. (2013). *Engineering of gold and aluminum plasmonic structures: Fabrication and fluorescence enhancement* (Doctoral dissertation, PhD Thesis).

[7] Murray, W. Andrew, and William L. Barnes. "Plasmonic materials." *Advanced materials* 19.22 (2007): 3771-3782.

[8] Bohren, C. F. (1983). How can a particle absorb more than the light incident on it? *American Journal of Physics*, *51*(4), 323-327.

[9] Bohren, C. F., & Huffman, D. R. (2008). *Absorption and scattering of light by small particles*. John Wiley & Sons.

[10] Forrest, S. R. (2005). The limits to organic photovoltaic cell efficiency. *MRS bulletin*, *30*(01), 28-32.

[11] Yoon, W. J., Jung, K. Y., Liu, J., Duraisamy, T., Revur, R., Teixeira, F. L., & Berger, P. R. (2010). Plasmon-enhanced optical absorption and photocurrent in organic bulk heterojunction photovoltaic devices using self-assembled layer of silver nanoparticles. *Solar Energy Materials and Solar Cells*, *94*(2), 128-132.

[12] Zhang, Y., Yip, H. L., Acton, O., Hau, S. K., Huang, F., & Jen, A. K. Y. (2009). A simple and effective way of achieving highly efficient and thermally stable bulk-heterojunction polymer solar cells using amorphous fullerene derivatives as electron acceptor. *Chemistry of Materials*, *21*(13), 2598-2600.

[13] Lee, K. C., Lin, S. J., Lin, C. H., Tsai, C. S., & Lu, Y. J. (2008). Size effect of Ag nanoparticles on surface plasmon resonance. *Surface and Coatings Technology*, *202* (22), 5339-5342.

[14] Giannini, V., Fernández-Domínguez, A. I., Heck, S. C., & Maier, S. A. (2011). Plasmonic nanoantennas: fundamentals and their use in controlling the radiative properties of nanoemitters. *Chemical Reviews*, *111*(6), 3888-3912.

[15] Gusak, V., Nkurunziza, E., Langhammer, C., & Kasemo, B. (2014). Real-Time Adsorption and Desorption Kinetics of Dye Z907 on a Flat Mimic of Dye-Sensitized Solar Cell TiO_2 Photoelectrodes. *The Journal of Physical Chemistry C*, *118*(30), 17116-17122.

[16] Halas, N. J., Lal, S., Chang, W. S., Link, S., & Nordlander, P. (2011). Plasmons in strongly coupled metallic nanostructures. *Chemical reviews*, *111*(6), 3913-3961.

[17] Stewart, M. E., Anderton, C. R., Thompson, L. B., Maria, J., Gray, S. K., Rogers, J. A., & Nuzzo, R. G. (2008). Nanostructured plasmonic sensors. *Chemical reviews*, *108*(2), 494-521.

[18] Hayashi, S., Kozaru, K., & Yamamoto, K. (1991). Enhancement of photoelectric conversion efficiency by surface plasmon excitation: A test with an organic solar cell. *Solid state communications*, *79*(9), 763-767.

[19] Stenzel, O., Stendal, A., Voigtsberger, K., & Von Borczyskowski, C. (1995). Enhancement of the photovoltaic conversion efficiency of copper phthalocyanine thin film devices by incorporation of metal clusters. *Solar energy materials and solar cells*, *37*(3), 337-348.

[20] Weickert, J., Dunbar, R. B., Hesse, H. C., Wiedemann, W., & Schmidt-Mende, L. (2011). Nanostructured organic and hybrid solar cells. *Advanced Materials*, *23*(16), 1810-1828.

[21] Duche, D., Torchio, P., Escoubas, L., Monestier, F., Simon, J. J., Flory, F., & Mathian, G. (2009). Improving light absorption in organic solar cells by plasmonic contribution. *Solar Energy Materials and Solar Cells*, *93*(8), 1377-1382.

[22] Kulkarni, A. P., Noone, K. M., Munechika, K., Guyer, S. R., & Ginger, D. S. (2010). Plasmon-enhanced charge carrier generation in organic photovoltaic films using silver nanoprisms. *Nano letters*, *10*(4), 1501-1505.

[23] Lal, N. N., Soares, B. F., Sinha, J. K., Huang, F., Mahajan, S., Bartlett, P. N., ... & Baumberg, J. J. (2011). Enhancing solar cells with localized plasmons in nanovoids. *Optics express*, *19*(12), 11256-11263.

[24] Hägglund, C., & Apell, S. P. (2010). Resource efficient plasmon-based 2D-photovoltaics with reflective support. *Optics express*, *18*(103), A343-A356.

[25] Min, C., Li, J., Veronis, G., Lee, J. Y., Fan, S., & Peumans, P. (2010). Enhancement of optical absorption in thin-film organic solar cells through the excitation of plasmonic modes in metallic gratings. *Applied Physics Letters*, *96*(13), 133302.

[26] Atwater, H. A., & Polman, A. (2010). Plasmonics for improved photovoltaic devices. *Nature materials*, *9*(3), 205-213.

[27] Nelson, J. (2003). *The physics of solar cells* (Vol. 1, pp. 1-15). London: Imperial college press.

[28] White, T. P., & Catchpole, K. R. (2012). Plasmon-enhanced internal photoemission for photovoltaics: Theoretical efficiency limits. *Applied Physics Letters*, *101*(7), 073905.

Chapter 4. Methodology

4.1 **Brief overview**.

The growth of thin films from atoms deposited from the gas phase is intrinsically a non-equilibrium phenomenon governed by competition between kinetics and thermodynamics [1]. Plasmon growth involves deposition of controlled amount of atoms onto a clean substrate at a well set of growth conditions such as pressure, time, surface energy and temperature. Upon deposition of an atom on a substrate, the ad atom diffuses on the flat surface. The ability to diffuse is described by the surface diffusion coefficient D defined as:

$$D = a^2 k_s \qquad 4\text{-}1$$

Where a is the effective hopping distance between sites while k_s is the site-to-site hopping rate of an ad atom and

$$k_s \propto \exp\{\tfrac{-V_s}{k_B T}\} \qquad 4\text{-}2$$

Where v_s is the potential energy barrier from site to site, T is the substrate temperature while k_B is the Boltzmann constant. D determines the average distance an ad atom will have to travel before either reaching and joining an existing island or meeting another ad atom for a possible nucleation [1].

In this project, the NPs have been grown using both RF magnetron sputtering and thermal evaporation techniques at room temperature. Thermal annealing of the films in air and Argon ambient was carried out exsitu. Different process parameters such as RF power, deposition time and the angle of inclination of substrate relative to source were varied to produce NPs of different sizes, shape and inter-particle distance.

4.2 Radio Frequency (RF) Sputtering.

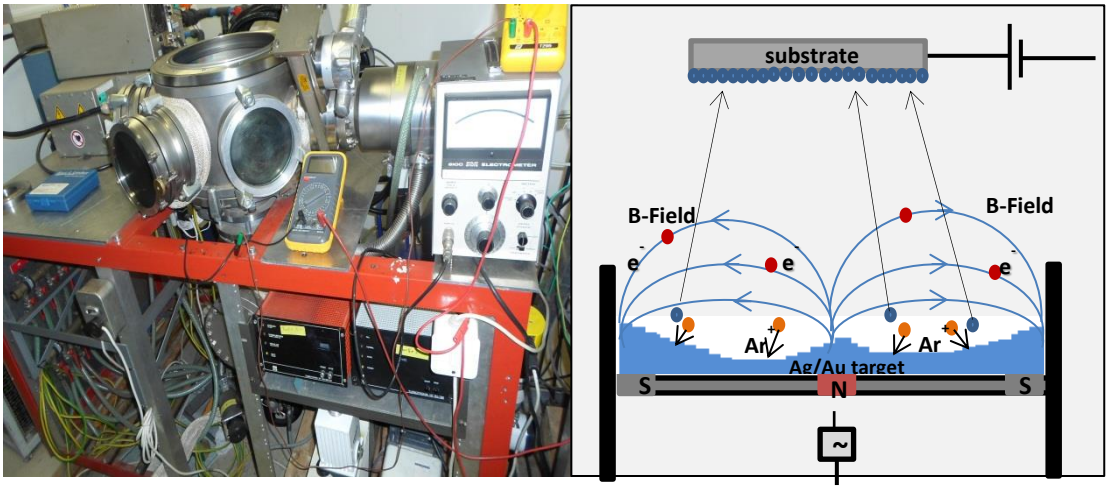


Figure 4.1 Schematic diagram of RF magnetron sputtering apparatus and b) sputtering mechanism.

Magnetron sputtering has rapidly developed over the last decade becoming popular in a wide variety of industrial coatings. This is due to rising demand for high quality functional films. The most common uses for sputtering are: interconnects in electronics, magnetic disks in data storage, anti-reflective coatings in optics, anti-corrosion coatings in surface coatings, and anti-rejection coatings in medical applications [2].

Sputtering is a physical vapor deposition (PVD) process used for depositing materials onto a substrate. This is done by ejecting atoms from the target which in turn condense onto a substrate (anode) in a high vacuum chamber.

The target acts as the source of material to be deposited. The chamber is first evacuated using a rotary pump up to 10^{-2} mbar, before the turbo pump is switched on, lowering the pressure further to 10^{-5} mbar. The vacuum reduces impurities associated with air or humidity in the chamber.

Once the desired vacuum has been attained, electrically neutral Argon atoms are introduced into the chamber. A RF power is applied to the target to generate a self-bias voltage placed between the target and the substrate. This DC voltage then creates a field which accelerates the free electrons present in the chamber. There is a stochastic probability that these

accelerating free electrons will collide with the Argon atoms introduced. If a free electron collides inelastically with an argon atom then there are two possible outcomes:

- The electron may cause excitation of the Argon atom making the gas atoms to glow. This electron will then either cause an outer-shell electron to be ejected or will be re-ejected, thus having one electron hit the Argon atom and one electron leaving the Argon atom.
- In case the electron has enough kinetic energy on collision with the Argon atom, it will ionize the atom resulting into ejection of two electrons. This secondary electron creates a cascading effect, with one electron producing two electrons and an ionized Argon atom. If a large number of Argon atoms undergo this process, then plasma (hot gas-like phase consisting of ions and electrons) is formed. The plasma is also known as glow discharge since it emits light.

The formed ions are then accelerated to the cathode target, which is held at negative voltage where they forcefully collide with the target surface. This collision provides enough energy to break the bonds between atoms of the target material and physically eject/sputter target material atoms. The ejected atoms will move in more or less a line of sight path and may get scattered as they collide with Argon atoms in the chamber.

The ejected atoms then travel some distance before they condense on the substrate to form a film. However, since electrons have a much higher velocity than the Argon ions, positive charges accumulate near the cathode. This will cause the area around the cathode to become depleted of electrons resulting into fewer collisions of electrons and Argon atoms, and in turn causing this area to be void of plasma. This area is called the dark zone and it can be minimized using a magnetron sputtering head.

The magnetron sputtering system has an additional strong magnetic field close to the target area which causes electrons to spiral along a magnetic flux lines adjacent to the target rather than being attracted towards the substrate. This ensures that the plasma is confined near

the target surface thereby minimizing film damage during growth. Besides, electrons are able to move through a longer distance, hence increasing the probability of further ionization of the argon atoms. This way, stable plasma is generated with high density of ions. In return the efficiency of the sputtering system is enhanced by the more ions formed. The faster ejection rate brings about increased rate of deposition. This reduces chances of formation of impurities in the thin-film while the long distance between the plasma and the substrate reduces chances of damage as a result of stray electron and Argon ions.

The rate of deposition known as sputtering yield is defined as the amount of atoms released from the target for every incident argon of given kinetic energy. For instance, a sputtering yield of 2 means that two target atoms are released for every incident Ar^{+} of given kinetic energy.

DC is commonly used in sputtering involving conducting targets. On the other hand RF power supply is convenient for insulator and semiconductor targets. RF has automatic or manual matching impedance capable of matching the network between the power supply and the sputtering gun with the automatic network being the most recommended for micro Magnetics magnetron sputtering system. The micro Magnetics magnetron sputtering guns are capable of operating with both DC and RF power supply. However, in most cases the magnetron sputtering has limited capability to using magnetic target materials. This is because of it magnetic nature of its target material that can interfere with magnetic field produced by the sputtering gun hence making the magnetron system less efficient. This can be solved using varying the design of the Micro Magnetics sputtering gun or the use of two sputtering gun i.e. the magnetic as well as non-magnetic [3].

4.3 Thermal evaporation

Thermal evaporation is one of the oldest and most inexpensive techniques used in growing thin films. Our interest in thermal evaporation for metal island film deposition stems from the following: the technique offers a great deal of promise in terms of general simplicity of operation, minimal requirements for sample preparation, ease of adaptation to automated operation, and potential for scale up to production levels of material throughput [4]. In contrast to all of the thin film deposition techniques, thermally evaporated thin films are built without the use of solvents. Thermal evaporation involves vaporizing a solid by heating the material to sufficiently high temperatures in high vacuum (10^{-5} mbar). The vaporized material diffuses vertically before re-condensing on a cooler substrate positioned above the evaporation site. On this substrate, the vaporized molecules are allowed to deposit. During this process, a quartz crystal monitor is used to measure the film's thickness and the deposition rate [5]. There is no damage associated with resistive thermal evaporation since there are no particles with high velocity incident to the growing film. Film properties strongly depend on chamber pressure (vacuum level) and film thickness [6], deposition rate, geometry of source relative to substrate, substrate temperature as well as the material concentration [7].

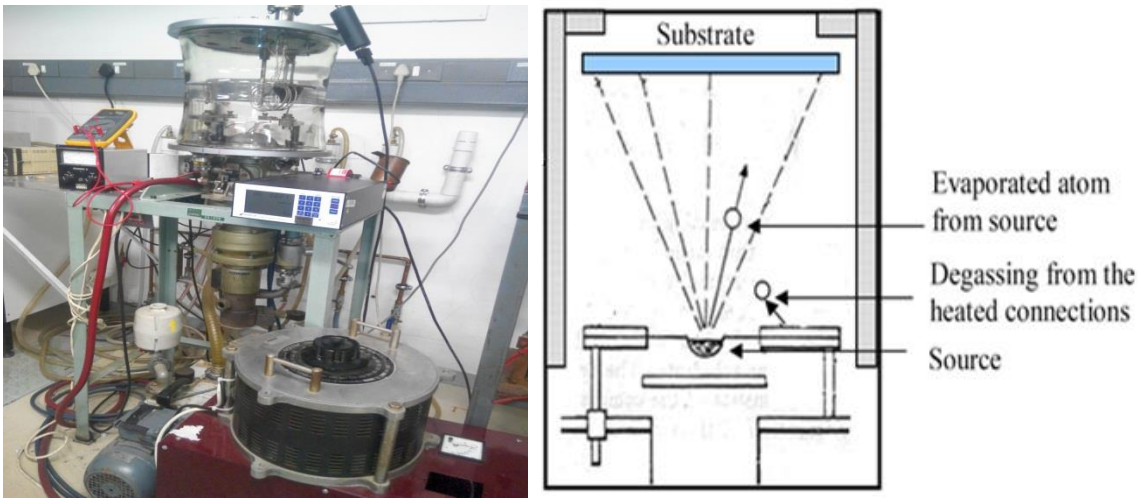


Figure 4.2 a) Schematic diagram of thermal evaporator fitted with quartz crystal monitor b) thermal evaporation mechanism.

The growth of thin film by physical deposition technique may assume different growth mechanisms such as:

- Frank van-de Merwe (FM) in which atoms are strongly bonded to the substrate than to each other resulting in two dimension growth of nucleus forming planar sheets,
- Volmer-Weber growth model in which the nucleus grows in 3-dimension forming islands on the substrate,
- Stransi-Krastanov growth which contain both Frank van-de Merwe and Volmer-Weber models. Here first one or two monolayers are formed followed by island formation on top,
- Polycrystalline and columnar growth models which occurs due to limited atomic mobility at the surface. Columnar shaped grains is mainly obtained on rough surfaces where peaks receive more atoms from all directions compared to the valleys as a result of geometrical shadowing while in case of low atom mobility on the surface, peaks tend to grow faster than the valleys.

4.4 Growth and characterization

4.41 Morphology of plasmons

Thermally evaporated and the RF sputtered silver NPs were characterized using Atomic force microscope (Veeco Di3100 AFM).

The Atomic Force Microscope is designed to measure local properties such as height, friction, and magnetism, using a sharp probe which is adjusted into close proximity with the sample surface [2]. The probe is fitted with a cantilever-type spring which has a fixed end and on the opposite side is a pyramidal tip attached on the underside [8]. In response to the Van der Waals force between tip and sample the cantilever, also called lever, is deflected. The tips normally have spring constants ranging between 0.001 to 100N/m driven to vibrate at a certain frequency ω with oscillation amplitudes of a few nanometers (~ 10 nm) [9]. When the tip is far away

from the sample, the tip and sample interaction can be ignored. The model of a damped harmonic oscillator can be applied as the probe is moved in a raster pattern relative to the sample, and measurements are taken in a serial fashion at discreet locations.

Surface morphology of deposited films can be studied using various modes: non-contact mode where the harp tip on a cantilever is brought into very close to a sample surface; contact mode where it is in contact with the surface; or in tapping mode where the cantilever vibrates on a resonance frequency in the very close vicinity of the sample surface so that the tip is intermittently touching the surface. A laser beam is incident on the cantilever and the reflected laser monitored. The tip-sample interaction causes a deflection of the cantilever hence causing a displacement of the reflected laser. This displacement is used to construct an image showing the surface morphology of the sample [2].

In this project "Tapping Mode" was used. Here the probe is driven to the natural resonance frequency using a piezoelectric motor such that the tip touches the surface only for a short time, thus avoiding the issue of lateral forces and drag across the surface. A direct tip-sample force is not actually measured instead the force is constructed by adding the short-range repulsive Coulomb and long-range attractive Van der Waals forces. The desired set point is maintained by processing the resulting error signal by a proportional-integral-differential (PID) feedback controller that drives the piezoelectric motor to minimize the error signal [9]. It is essential to adjust the feedback system to achieve reliable information from the AFM due to the inherently unstable feedback situation in Tapping Mode operation making it difficult to automate some of the scan adjustments. Forces can vary when going away from a steady-state situation. The higher the tip amplitude, the higher the energy stored in the lever and in the imaging forces. Drift due to temperature changes and/or fluid levels change may also affects the operation in fluids [10]

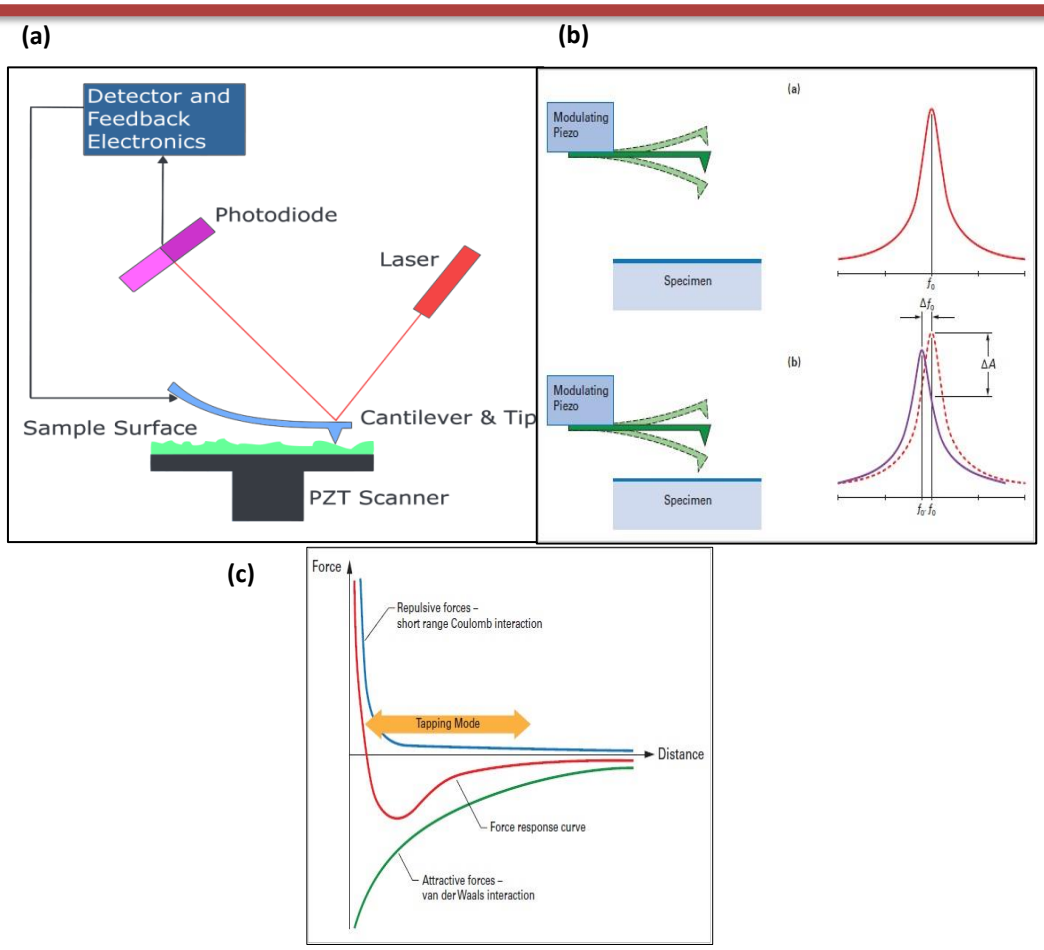
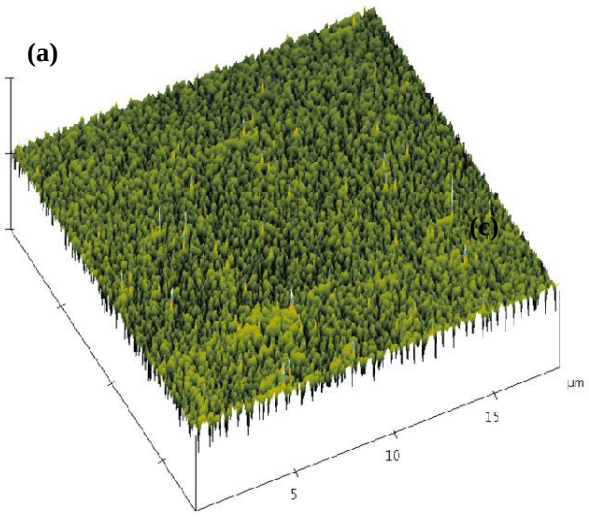


Figure 4.3 Schematic diagram of the cantilever-tip assembly used in an AFM b) Resonance curves of a Tapping Mode cantilever above and close to the surface c) Force curve highlighting the motion of an oscillating cantilever in Tapping Mode adapted from [2].

The force curve or direct forces between the tip and the sample (shown in Fig 4.3 c)) shows an average response of many interactions through the lock-in amplifier.



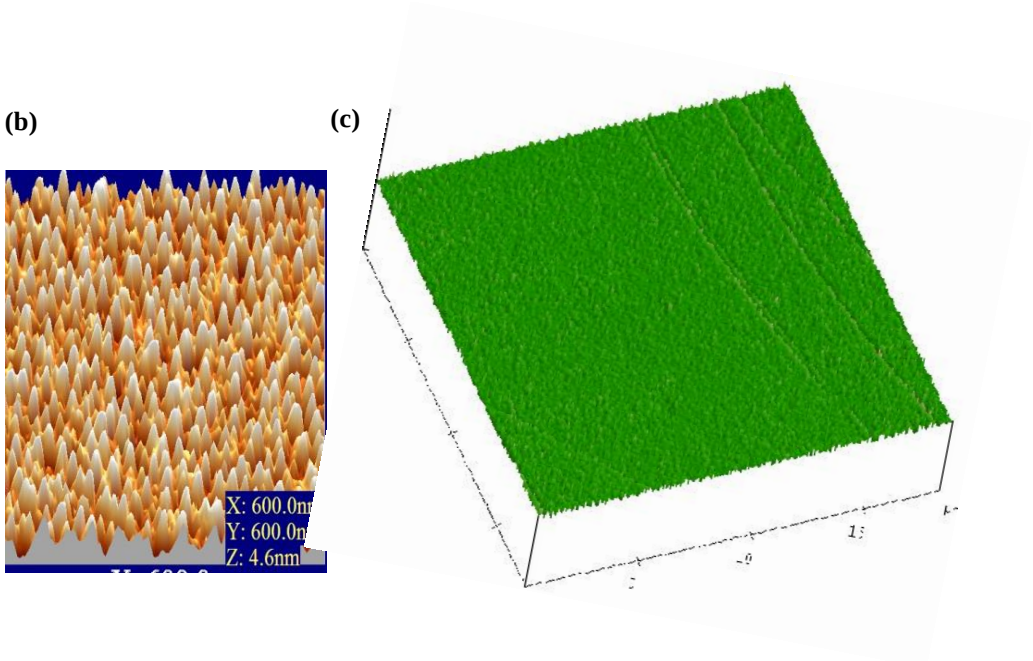


Figure 4.4 AFM images of as-deposited Ag nanoparticles a) thermally evaporated film with substrate directly above the source b) AFM derived dimensions of the films c) RF sputtered Ag film.

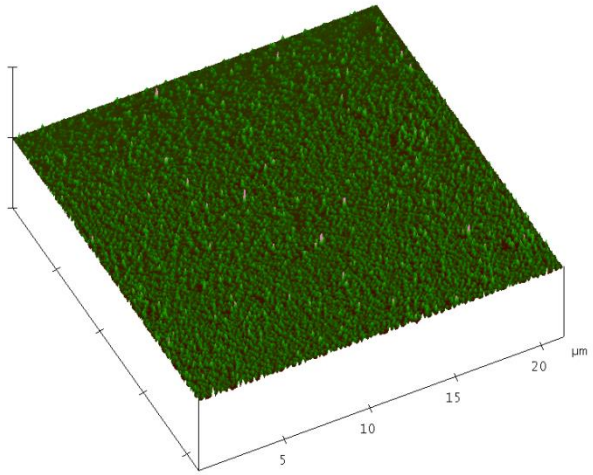


Figure 4.5 AFM images of as-deposited thermally evaporated Ag nanoparticles with the substrate inclined at an angle of 70^{o} with the source.

In order to attain isolated islands at a constant target-substrate distance (~6 cm), argon was let in at a flow rate of 13 sccm at STP and a low deposition time of about 10 seconds was used. The 4.6 nm film deposited by both thermal evaporation and sputtering system onto an ITO substrate was found to yield a discontinuous morphology consisting of a dense structure of highly irregular nanostructures with a high surface coverage of ~ 79%. When the substrate was

inclined at an angle of 70^{o} to the Ag source, the surface coverage is irregular as the distance from the source is not uniform (Figure 4.5). This gives regions closest to the source to be densely populated compared to other areas as shown in fig 4.5. This shows that the orientation and surface distribution of the particles on the surface is also affected by the angle of inclination of the substrate to the source. The surface statistical analysis indicated various size distributions ranging from 5nm to 70 nm. The inter-particle distance derived from grain analysis using image J programme showed that the particles are very close to one another resulting into high surface coverage.

The films were then annealed in Argon filled furnace with a one cycle of ramping and dwelling with the ramping set at a rate of 100 ^{o}C/ minutes and a dwelling time of 10 minutes. With these settings, the annealing temperatures were varied between 100-250 ^{o}C and the annealed samples scanned ex-situ at room temperature using the AFM.

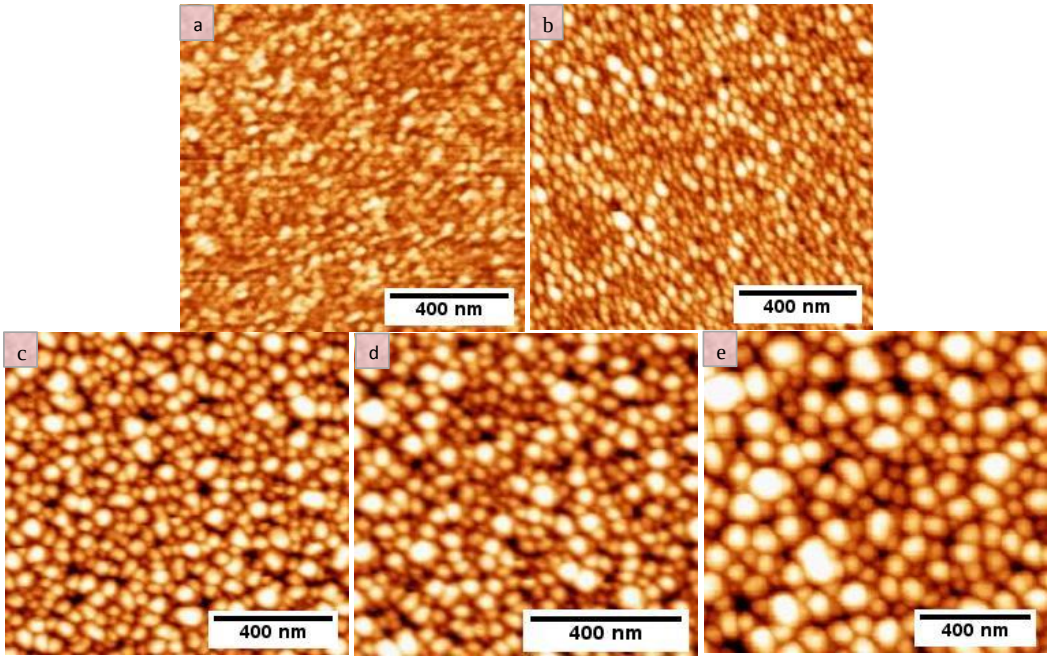


Figure 4.6 AFM image of RF sputtered Ag nanoparticles after thermal annealing process in Argon filled furnace at different temperatures a) as-deposited b) annealed at 100 ^{o}C c) annealed at 150 ^{o}C d) annealed at 200 ^{o}C e) annealed at 250 ^{o}C.

Films which were grown using thermal evaporation also showed similar morphology upon annealing.

The AFM images show that increasing annealing temperature leads to the formation of large Ag nanoparticles coupled with reduced coverage (Fig. 4.6 & 4.7). This is seen by the increase in the inter-island spacing with annealing as corroborated by the values in Table 4.1. The Ag nanoparticles reconstruct to assume a "hemispherical" like shape with increasing temperature. From size distribution analysis, the mean particle diameter increased with increasing annealing temperature as shown in Figure 4.7.

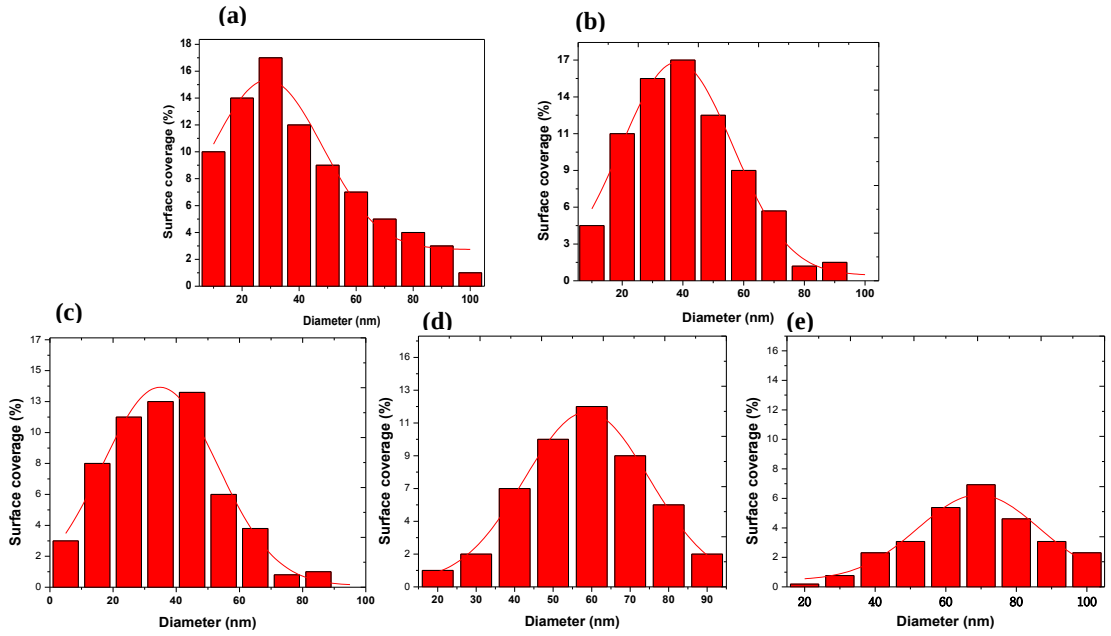


Figure 4.7 Size distribution of RF sputtered Ag nanoparticles upon annealing pristine Ag islands and those annealed at a temperature range of 100-250 ^{o}C in argon ambient.

Table 4.1 Summary of AFM analysis on the Ag nanoparticles annealed at different temperature in Argon filled furnace.

Annealing temperature (°C)	Mean diameter (nm)	Surface coverage (%)
As-deposited	39	79
100	41	77
150	46	61
200	58	49
250	71	38

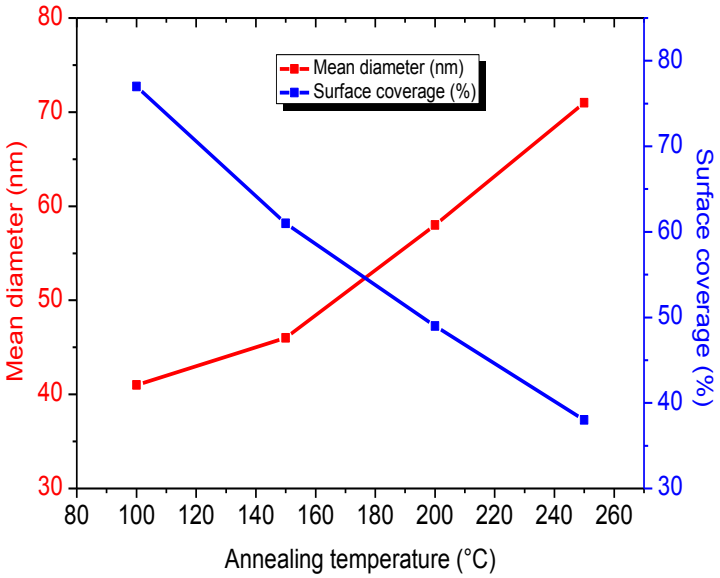


Figure 4.8 Graphical variations of mean diameter and surface coverage with annealing temperature.

During thermal annealing of thin films, plastic and elastic effects produce the partial collapse of the boundary network of surface protrusions (SPs). This in turn promotes relaxation processes driven by surface diffusion, diffusion into grain boundaries, and bulk diffusion [11]. According to Porath *et al.* grain-coarsening occurs when films are annealed at high temperature exceeding 300°C as a result of a combination of grain boundary migration as well as bulk-defect diffusion. This mechanism is normally associated with high activation energies.

However, at lower temperatures (T< 300°C) surface diffusion dominates over bulk defect diffusion [12].

Surface tension causes the metal atoms in thin films coalesce together to form clusters at high temperature. This is attributed to the reduction in surface energy inducing surface migration which leads to restructured Ag nanoparticles which have more hemispherical shapes relative to pristine islands formed after sputtering [13]. The ad atoms in the as-deposited Ag film initially form islands with irregular shapes. This conforms to the Volmer-Weber film growth mode. The shapes and sizes of these nano islands are reconstructed by annealing due to increased diffusion of ad atoms at high temperature. Further annealing modifies the surface energy approximated to be in the range of 0.97-2.17 J/m^2, inducing surface migration and reconstruction of the Ag nanoparticles to more hemispherical like shapes relative to their 'as deposited' counterparts [14]. This is further corroborated by the decrease in surface coverage with increasing annealing temperature (Table 4. 1). The AFM data show that the surface coverage decreases from 79% as-deposited Fig 4.7 (a) to 38% at 250 °C shown in fig 4.7(e). Since these temperatures, are far below the melting temperature of Ag (T_M = 1235 K), the reduction in surface coverage can be attributed to migration of Ag atoms at the surface which leads to an increase in Ag nano-island diameter after coalescence [15].

We have determined the activation energy required for the reconstruction of the Ag islands to be 50 ± 13 meV and this is consistent with the values obtained for Ag diffusion in a monolayer of Ag [16]. The results of this measurement have been extracted in the Arrhenius plot of fig 4.9. This is a plot using Arrhenius equation $K = Ae^{-E_a/k_BT}$ such that the slope gives the activation energy of the particle.

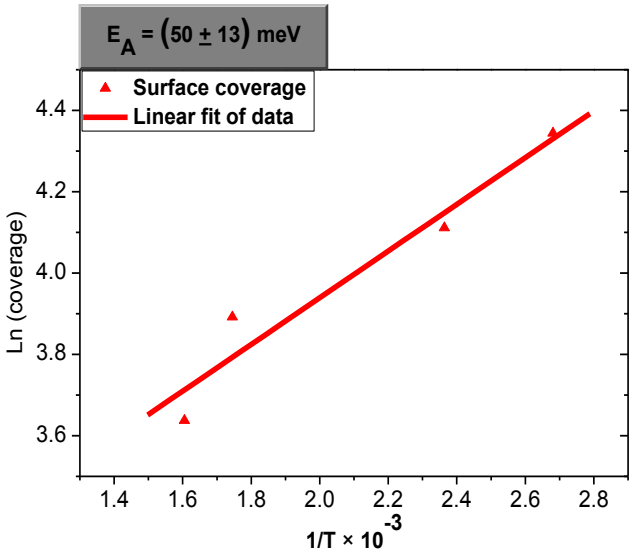


Figure 4.9 Arrhenius plot to show the dependence of coverage with temperature, the activation energy has been determined to be 50 ±13 meV.

After annealing at 100 °C (Fig. 4.4 a) Ag islands of 20–50 nm lateral dimensions become more pronounced. With increasing temperature, the lateral dimension increases gradually. At 200 °C and 250 °C (fig 4.4 c-d), only a trace of the initial 20–30 nm islands is still apparent. The island size of 50-60 nm and 60-80 nm, respectively dominate in these temperature regimes. Surface migration of particles enhances coalescence resulting in fewer, larger particles [15]. The reduction in surface coverage can be attributed to an increase in nanoparticle diameter as the particles coalesce resulting in fewer, larger particles.

4.42 In situ annealing

Annealing can also be achieved by mounting the samples on a heated stage such that the deposition surface is energized.

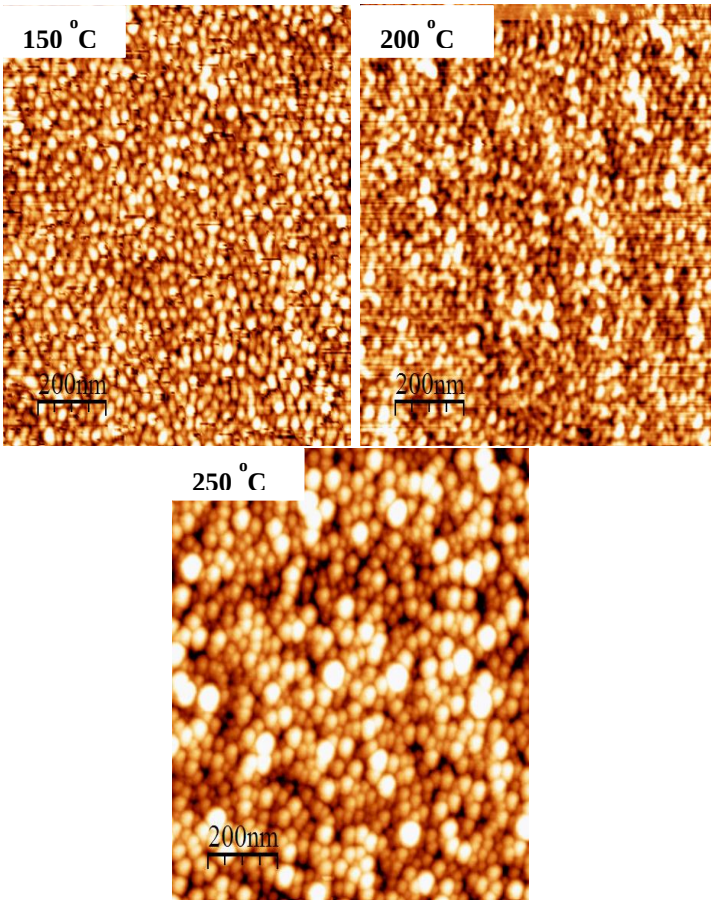


Figure 4.10 AFM image of RF sputtered Ag nanoparticles annealed in situ at different temperatures a) 150 °C b) 200 °C c) 250 °C.

At low substrate temperature the particles remain rather immobile since their adhesion to the substrate and surface tension are larger than surface diffusion energy. This is attributed to possible partial submersion. This can be explained by the fact that the surface energy of Ag nanoparticles derived from Kelvin equation of 7.2 J/m^2 [18] is larger than that of the glass substrate ranging between 0.25-0.5 J/m^2. Annealing in situ enhances surface diffusion of the nanoparticle leading to formation of larger particles with increased inter-island distance.

4.43 Optical properties of NPs.

When a particle is illuminated by a beam of light, part of the light is absorbed by the particle while the other is inelastically scattered to produce radiation of lower energy. The amount of light scattered and absorbed by the particle, as well as the angular distribution of the scattered light, depend on the particular characteristics of the particle, i.e., its shape, size and material properties. The attenuation of an electromagnetic wave by the phenomena of scattering and absorption is called extinction [19]. At plasmonic resonance excitation, strong scattering and absorption of the light results in intense surface plasmon extinction bands [20]. The ability of a material to absorb at a particular wavelength is described by the absorption coefficient; a good material for solar cell application should have a high absorption over a wide range of wavelengths. In this project the silver NPs grown by different power and time were characterized using UV-Vis NIR-500 Carry Spectrometer.

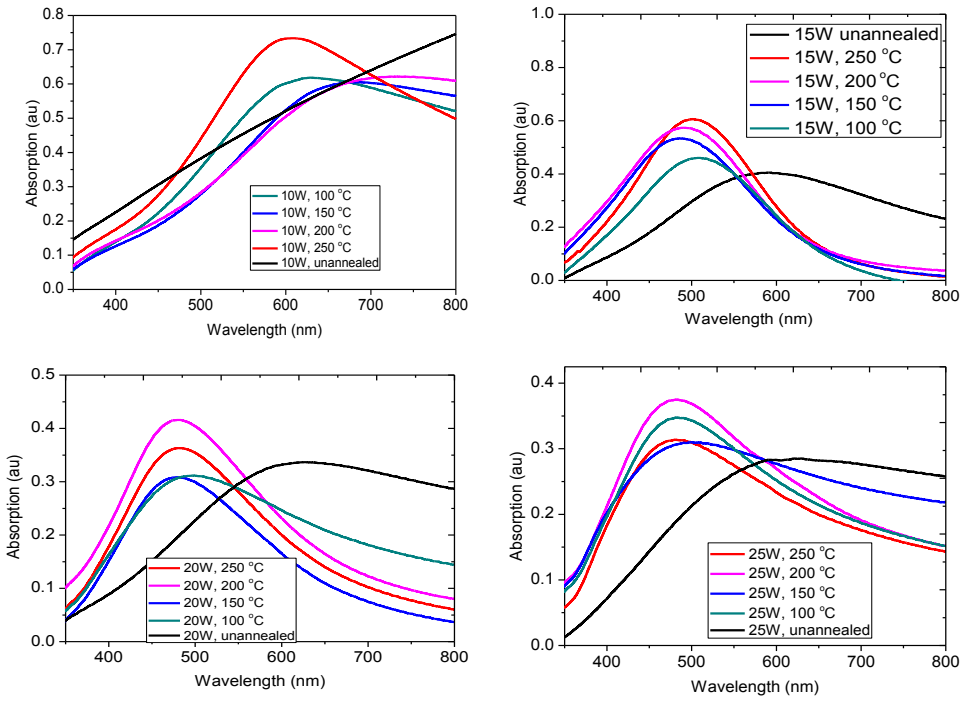


Figure 4.11 Optical absorption spectra of Ag nanoparticles grown by RF sputtering system at different powers for 8 seconds before being annealed at different temperature in Argon ambient.

From Fig 4.11, the sputtered NPs show broad LSP resonance band around 600 nm except for the sample sputtered at 10W, 8 seconds that only shows an absorption peak upon annealing. The reduction in the full width at half maximum (FWHM) upon annealing indicates that annealing decreases the lifetime of the surface plasmons.

Setting high sputtering power in magnetron sputtering system energizes inert argon gas hence providing sufficient kinetic energy to ad atoms. The surface diffusion of these ad atoms is therefore expected with the increased momentum transfer to enhance nucleation and growth in the film. As the power increases, the surface mobility of the ad atoms also increases resulting in formation of continuous film hence the reduction in LSP absorption seen in figure 4.11. On the other hand the low sputter power produce low deposition rate as the Ar^+ are less energetic to knock out the target species resulting in slow nucleation and growth related to a few small grains on the surface [19]. This may have led to the disappearance of absorption peak when the power was set at 10W for 8 seconds.

NPs sputtered at 15W (Fig 4.11 (b) showed blue shifted absorption peaks with enhanced absorption upon annealing in Argon ambient. The broad LSP resonance band before annealing can be explained in terms of LSP multi-pole effects according to the Mie theory [22]. Annealing in argon ambient leads to a blue shift in plasmon band and sharper peaks. The blue shift in plasmon absorption coupled with the size and shape changes evidenced by the AFM is attributed to the net surface Plasmon changes. Although it is expected that an increase in particle size leads to a red shift in plasmon absorption maximum, the decreased interaction of neighboring nanoparticles dominate due to increased particle separation since mass is conserved on the surface during annealing [23-24]. Hence as nanoparticles become more spherical, larger and more spaced, the width of the absorption band is determined by the inter-particle dipole-dipole interactions [4]. Annealing at 100 ^oC, 150 ^oC and 200 ^oC, causes surface reconstruction of the Ag island resulting from surface diffusion which aids in the migration of

the ad atoms on the Ag island. With further increase in temperature, the smaller size nano structures coalesce to form larger size clusters. At 250 ^{o}C the Ag nanoparticles absorption eventually red shifted. This red shift is attributed to the increase in the Ag island size and also on island interspacing which weakens dipole-dipole interactions. At this juncture the plasmonic absorption is dominated by the size and shape of the isolated nanoparticles [4]. This result from dipole resonance redshift when size is increased, which is mainly attributed to retardation of the depolarization field across the sphere diameter [17]

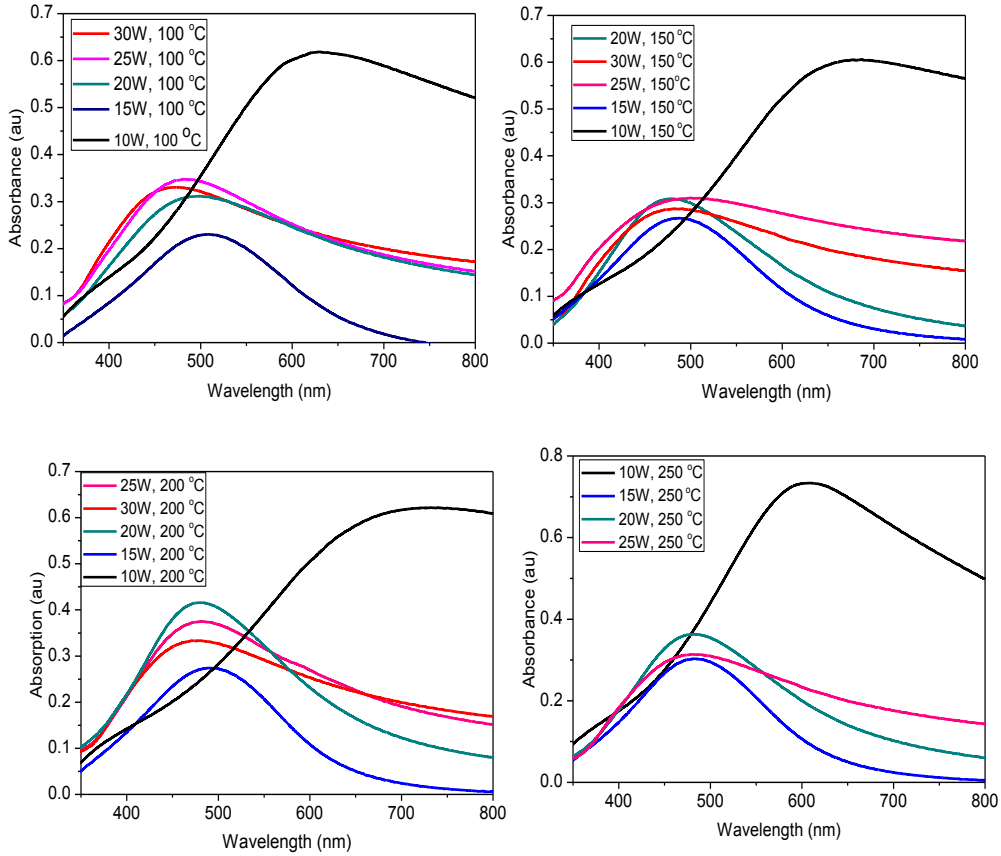


Figure 4.12 Optical absorption spectra of Ag nanoparticles grown by RF sputtering system at different power before being annealed at a particular temperature in Argon ambient.

The broad absorption band when NPs sputtered at 10W before they are annealed may be as a result of few nanoparticles of varied shapes and sizes formed on the surface. As the power change at constant temperature, the position of the absorption peak is not greatly affected as

evidenced in figure 4.12, all peaks for a given temperature seems to be at the same wavelength except for the 10W NPs.

During annealing in Argon ambient, an increase of temperature up to 200 ^{o}C, a blue shift is observed as well as enhanced absorption seen in the increased absorption peaks. This could be as a result of surface reconstruction of the Ag island resulting from surface diffusion which aids in the migration of the ad atoms on the Ag island. With further increase in temperature, the smaller size nano structures coalesce to form larger size clusters.

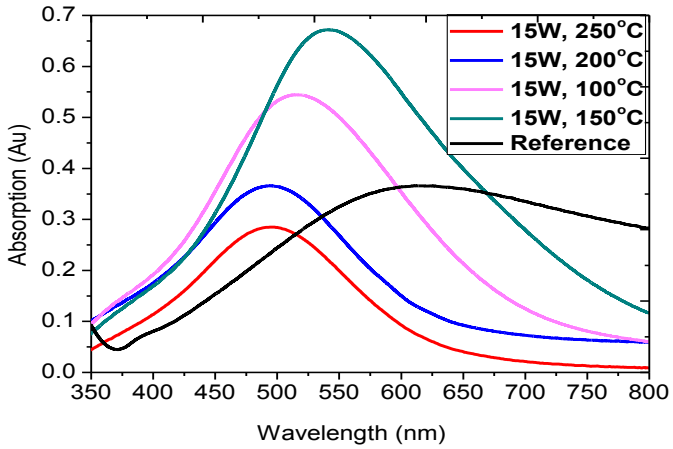


Figure 4.13 Optical absorption spectra of Ag nanoparticles grown by RF sputtering system at a DC power of 15 W for 10 seconds before annealing in air.

Annealing in air and at elevated temperatures induces a change in the surface energy and curvature of the Ag nanoparticles, this in the presence of atmospheric O_2 leads to the possible formation of the thermodynamically stable Ag_2O (at low temperatures < 170°C) and AgO phases on the surface of the Ag nanoparticles. This assertion corroborates with the study by De Rooij on the nature of the silver oxide polymorphs formed under diverse annealing conditions of Ag surface [16]. The oxidation of Ag nanoparticles reduces the SPR effect. At 200°C the oxide layer is somewhat thicker causing a reduction in absorption [17] as witnessed in fig 4.3. Oxidation reduces the amount of atomic Ag present in the nanoparticles and thereby decreases the density of free carriers. In addition the formation of an oxide envelops on the Ag nanoparticles leads to the screening of the local field by the oxide. While we have not provided sufficient experimental evidence on the oxidation state of silver due to the limited volume of the oxide present which precludes precise measurement of the oxidation state, the possible phases of silver oxide present on the surface of the Ag nanoparticles have been postulated

solely from thermodynamic arguments. The oxidation of Ag is dependent on the O_2 partial pressure and the energy of formation (ΔH_f = -31.1 kJ/mol) of the $Ag_{1-x}O_x$ at the surface of the Ag islands [24-27]. Further annealing of Ag islands in air increases the thickness of the $Ag_{1-x}O_x$ envelop over the Ag nanoparticles, thus decreasing the size of the Ag nanoparticles and shifting the absorption maximum towards the blue

According to De Rooij silver readily forms unstable Ag_2O at room temperature. Above 100 ^oC, a stable oxide layer formed may show heavy flaking [28]. The variation in the high frequency dielectric constant of $\varepsilon_\infty(Ag)$ and $\varepsilon_\infty(Ag_{1-x}O_x)$ yields a decrease and shift in the optical absorption,α.

Another important factor to consider during thin film deposition is the deposition time.

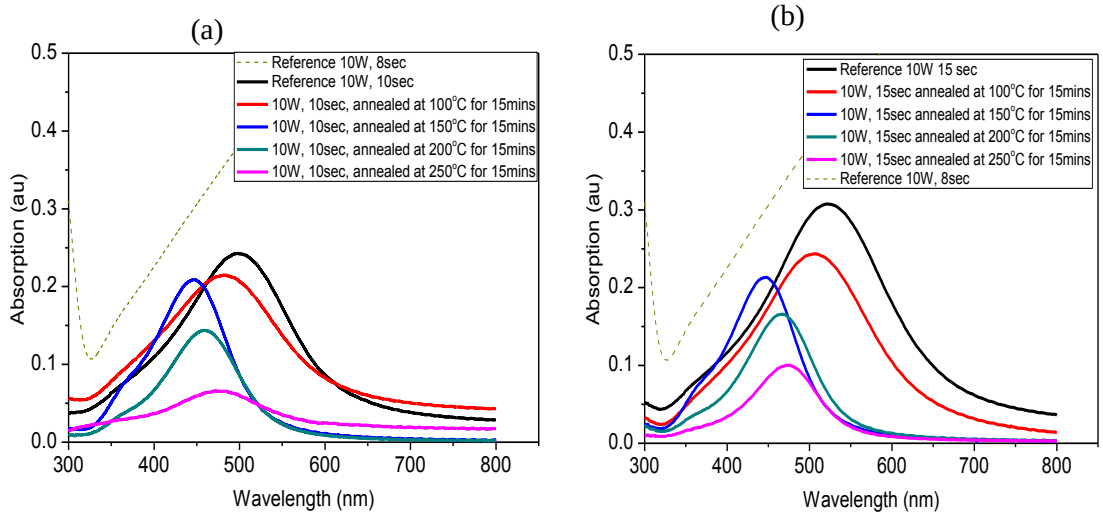


Figure 4.14 Optical absorption spectra of Ag nanoparticles grown by RF sputtering system at power of 10W for different periods of time before being annealed in air.

The thickness of the film gradually increases with deposition time. Very thick film are not suitable for incorporation into organic solar cells as they are likely to cause short circuiting in case there exist hillocks making the islands penetrate from one electrode to the other. Furthermore presence of continuous film may bring about a mismatch in work function with semiconductor energy level making them act as recombination sites. NPs at low power and time exhibit no LSP absorption as the particles are quite few and are too far from one another as shown by the 10 W, 8 seconds graph (dotted) in fig 4.14.

A similar trend is observed for Au NPs upon annealing. This behavior is further dependent on variation of deposition power and time. The fundamental difference is in the position of resonance in which case these absorption peaks are observed at higher wavelengths. At sputtering power of 10W, gold require more deposition time in order to realize reasonable absorption peak as shown in figure 4.15. Increasing deposition time leads to a red-shift in absorption peak as the particles sizes increases as well as the distance between the particles gradually decreases.

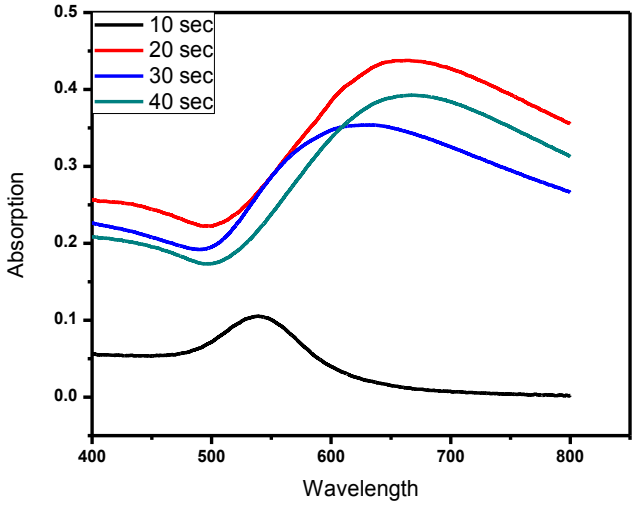


Figure 4.15 Optical absorption spectra of Gold NPs grown by RF sputtering system at DC power of 10W for different periods of time.

An attempt to incorporate Au plasmons sputtered at low power of 15W and 10W into the OPV device showed minimal enhancement.

Reference

[1] Zhang, Z., & Lagally, M. G. (1997). Atomistic processes in the early stages of thin-film growth. *Science*, *276*(5311), 377-383.

[2] Wright, J. (2014). *Design and Implementation of DC Magnetron Sputter Deposition System and Hall Effect System Via LabVIEW* (Doctoral dissertation, Ohio University).

[3] http://www.directvacuum.com/pdf/what_is_sputtering.pdf

[4] Gupta, R., Dyer, M. J., & Weimer, W. A. (2002). Preparation and characterization of surface plasmon resonance tunable gold and silver films. *Journal of Applied Physics*, *92*(9), 5264-5271.

[5] Bashar, S. A. (1998). Study of indium tin oxide (ITO) for novel optoelectronic devices. *UMIST, Manchester*, 106-109.

[6] Yao, J. L., Hao, S., & Wilkinson, J. S. (1990). Indium tin oxide films by sequential evaporation. *Thin Solid Films*, *189*(2), 227-233.

[7] Balasubramanian, N., & Subrahmanyam, A. (1989). Electrical and optical properties of reactively evaporated indium tin oxide (ITO) films-dependence on substrate temperature and tin concentration. *Journal of Physics D: Applied Physics*, *22*(1), 206.

[8] Shin, B. (2007). *Study of thin film growth kinetics of homoepitaxy by molecular beam epitaxy and pulsed laser deposition* (Doctoral dissertation, Harvard University Cambridge, Massachusetts).

[9] Wen, J. (2011). Excitation and Detection of Highly Confined Plasmonic Gap Modes with Subwavelength Dimensions.

[10] http://www.azonano.com/article.aspx?ArticleID=3010

[11] Alonzo-Medina, G. M., González-González, A., Sacedón, J. L., & Oliva, A. I. (2013, June). Understanding the thermal annealing process on metallic thin films. In *IOP Conference Series: Materials Science and Engineering* (Vol. 45, No. 1, p. 012013). IOP Publishing.

[12] Porath, D., Bar-Sadeh, E., Wolovelsky, M., Grayevsky, A., Goldstein, Y., & Millo, O. (1995). Annealing study of gold films using scanning tunneling microscopy. *Journal of Vacuum Science & Technology A*, *13*(3), 1165-1170.

[13] Semin, D. J., & Rowlen, K. L. (1994). Influence of vapor deposition parameters on SERS active Ag film morphology and optical properties. *Analytical Chemistry*, *66*(23), 4324-4331.

[14] Nakayama, K., Tanabe, K., & Atwater, H. A. (2008). Plasmonic nanoparticle enhanced light absorption in GaAs solar cells. *Applied Physics Letters*, *93*(12), 121904.

[15] Temple, T. L., Mahanama, G. D. K., Reehal, H. S., & Bagnall, D. M. (2009). Influence of localized surface plasmon excitation in silver nanoparticles on the performance of silicon solar cells. *Solar Energy Materials and Solar Cells*,*93*(11), 1978-1985.

[16] P. Royer, J. Goudonnet, R. Warmack, T. Ferrell, Substrate effects on surface-plasmon spectra in metal-island films, Physical Review B, 35 (1987) 3753.

[17] Bi, H., Cai, W., Zhang, L., Martin, D., & Träger, F. (2002). Annealing-induced reversible change in optical absorption of Ag nanoparticles. *Applied physics letters*, *81*(27), 5222-5224.

[18] Medasani, B., Park, Y. H., & Vasiliev, I. (2007). Theoretical study of the surface energy, stress, and lattice contraction of silver nanoparticles. *Physical Review B*, *75*(23), 235436.

[19] Andreas T. Optical properties of metallic nanoparticles. Diss. Institut für Physik, Fachbereich Theoretische Physik Karl–Franzens–Universität Graz, Juli 2011.

[20] Doron-Mor, I., Barkay, Z., Filip-Granit, N., Vaskevich, A., & Rubinstein, I. (2004). Ultrathin gold island films on silanized glass. Morphology and optical properties. *Chemistry of materials*, *16*(18), 3476-3483.

[21] Le, M. T., Sohn, Y. U., Lim, J. W., & Choi, G. S. (2010). Effect of sputtering power on the nucleation and growth of Cu films deposited by magnetron sputtering. *Materials transactions*, *51*(1), 116-120.

[22] Cheng, P., Li, D., & Yang, D. (2011). Effect of rapid thermal processing on surface plasmon resonance of Ag island films. *Optoelectronics and advanced materials-rapid communications*, *5*(3-4), 455-458.

[23] Hutter, E., & Fendler, J. H. (2004). Exploitation of localized surface plasmon resonance. *Advanced Materials*, *16*(19), 1685-1706.

[24] Yguerabide, J., & Yguerabide, E. E. (1998). Light-scattering submicroscopic particles as highly fluorescent analogs and their use as tracer labels in clinical and biological applications: I. Theory. *Analytical biochemistry*, *262*(2), 137-156.

[25] Aslan, K., Leonenko, Z., Lakowicz, J. R., & Geddes, C. D. (2005). Annealed silver-island films for applications in metal-enhanced fluorescence: interpretation in terms of radiating plasmons. *Journal of fluorescence*, *15*(5), 643-654.

[26] Mertens, H., Koenderink, A. F., & Polman, A. (2007). Plasmon-enhanced luminescence near noble-metal nanospheres: Comparison of exact theory and an improved Gersten and Nitzan model. *Physical Review B*, *76*(11), 115123.

[27] Akihisa, Y., & Hiroshi, K. (1992). In situ optical observation of oxygen-adsorption-induced reversible change in the shape of small supported silver particles. *Surface science*, *264*(1), 147-156.

[28] A. De Rooij, The oxidation of silver by atomic oxygen, EsA Journal, 13 (1989) 363-382.

[29] De, G., Gusso, M., Tapfer, L., Catalano, M., Gonella, F., Mattei, G., ... & Battaglin, G. (1996). Annealing behavior of silver, copper, and silver–copper nanoclusters in a silica matrix synthesized by the sol-gel technique. *Journal of applied physics*, *80*(12), 6734-6739.

Chapter 5. Efficiency enhancement.

The potential for inexpensive renewable energy relies heavily on organic photovoltaic technology, due to their low cost of production and mechanical flexibility. However for commercialization purposes, more efficient OPV devices are necessary. Besides numerous attempts to developing new materials, significant efforts are focused on device performance improvement upon optimization of the active layer morphology, either by solvent selection, temperature and solvent annealing processes [1]. In this chapter we present the effect kinetics and energetics of thermal treatment of the reference device on the efficiency of OPV upon incorporation of Ag nanoparticles.

5.1 *Effect of thermal annealing*

Figure 5.1 shows the structure of a standard BHJ Organic solar cell used as a reference cell. Each reference device includes three main layers starting with indium tin oxide as a transparent positive anode, 0.16 cm^2 of the active area (P3HT:PCBM) sandwiched between the hole transport layer PEDOT:PSS and a layer of Aluminum (Al) acting as the cathode.

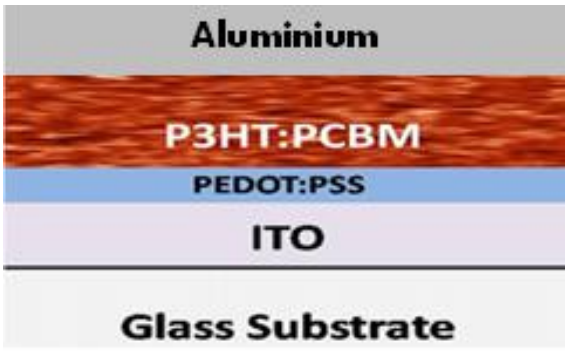


Figure 5.1 Device architecture of reference cell.

The fabrication process starts with cutting ITO-coated glass into 1.25 cm × 1.25 cm slices using a diamond tip scriber. The half portion of cut ITO glass was then etched away through wet chemistry with zinc powder and hydrochloric acid. This helps in reducing chances of short-circuiting the device during I-V measurements. The samples were then cleaned with detergent and rinsed with deionized (DI) water. After ultrasonicating the samples with acetone, methanol,

ethanol and DI water for 10 minutes each, the substrates were dried with nitrogen and baked at 150 ºC for 20 minutes. PEDOT:PSS (Baytron PH 500) was then spin cast on the cleaned ITO has received and baked for 15min. at 130°C. 10 mg of P3HT and PCBM each were then separately dissolved in 0.5 ml of chlorobenzene and stirred for 3 hours before being mixed and again stirred for two hours to form 1:1 wt %, 20mg/ml in chlorobenzene solution. To achieve highly reproducible performance of Organic solar cell, the film quality of P3HT and PCBM is critical. Both P3HT and PCBM have functional side groups that give solubility in organic solvent. However, the solubility of polymer and the fullerene varies with type of solvent used. Therefore, the blend solution should be carefully prepared to produce a homogenous film. Figure 5.2 shows microscopy images of the spin cast film from 1:1 wt % of P3HT and PCBM solution in chlorobenzene solvent (a) before and (b) after proper dissolution in chlorobenzene. The big particles in Figure 5.2 (a) are the aggregates of P3HT/PCBM due to their limited solubility. The aggregates of organic semiconductor are believed to cause charge accumulation and/or localized charge trapping [2]. Proper dissolution enhances good morphology development necessary for efficient exciton generation, diffusion as well as ultimate charge transport to the respective electrodes.

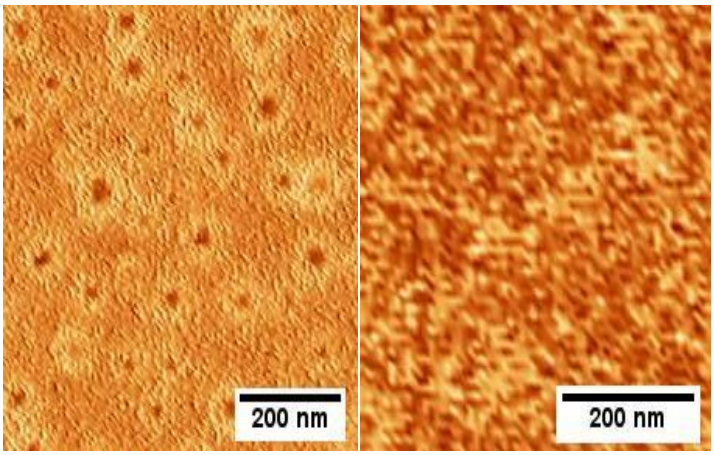


Figure 5.2 The morphology of P3HT:PCBM blend before and after proper dissolution in chlorobenzene.

The P3HT:PCBM blend was then spin coated at 2000 rpm for 1 minute to yield a homogeneous film of 165 nm film measured using Surface profilometer. 200 nm layer of aluminum was then thermally evaporated at a pressure of 2×10^{-6} mbar to form ITO/PEDOT:PSS/P3HT+PCBM/Al device. One glass slide was characterized as casted while the other was annealed at different temperature for 10 minutes. Another set of the devices were annealed at a constant temperature (50 ^{o}C) over varied time intervals to ascertain the effect of annealing time and temperature on the device.

The absorption of the device was measured using UV-Vis NIR-500 Carry Spectrometer while the current density–voltage (J–V) characteristics were obtained using HP 4141B source measure unit (SMU) under 70 mW/cm^2 illumination (AM 1.5G). All the measurements were carried out at room temperature under standard conditions.

The photovoltaic activity of the P3HT:PCBM layers may be increased remarkably by varying the film composition (ratio of polymer to fullerene or introduction of a third organic molecule), thickness and/or growth conditions, including the processing solvents and annealing temperatures. The morphology and the molecular parking of both P3HT and PCBM within their respective domains must be optimized in order to ensure maximum charge-carrier mobilities as well as exciton diffusion. Moreover, the nanophase segregated heterojunction domain size must be less than the diffusion length to ensure efficient conversion of adsorbed photons into useful electrical current to be collected at the electrodes. In BHJ solar cells, the charge must travel perpendicular to the substrate in order to reach the electrodes hence the need for $\pi - \pi$ stacking (delocalized π electrons) oriented perpendicular to the substrate [3]. This can be achieved by controlled thermal annealing or molecular self-assembly. A first clear visual observation upon annealing is the change in color of the active layer from orange/brown to purple/red.

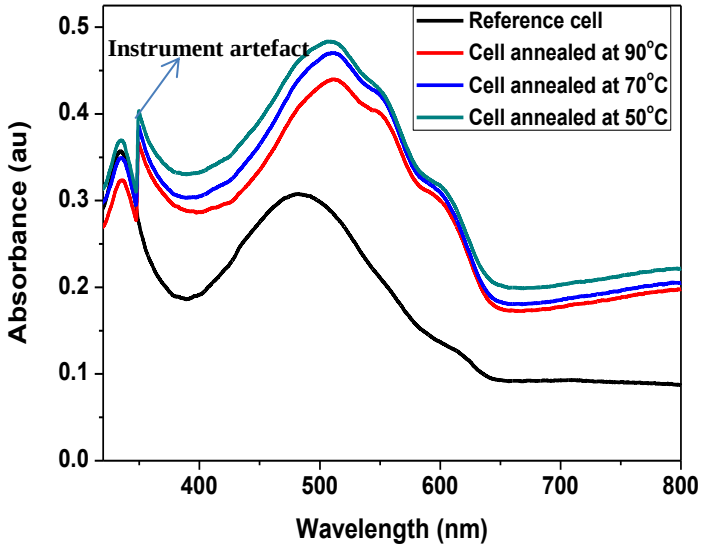


Figure 5.3 UV-Vis absorption spectra of P3HT: PCBM blend films as cast and after annealing for 10 minutes at 50 ^{o}C, 70 ^{o}C and 90 ^{o}C ± 10 ^{o}C.

The singularity at 350 nm in the absorption data in figure 5.3 and 5.4 could be attributed to change in the spectrometer lamps during measurement.

The three apparent vibronic absorption shoulders at wavelength range of 550 - 650 nm, observed from the absorption spectra in figure 5.3 can be attributed to the strong interchain-interlayer interactions of P3HT [4].

From the UV-Vis spectrometer measurements, it is evident that the absorption maximum of annealed samples is red shifted from 488nm to 512nm and the overall absorption efficiency increases due to the formation of the ground state aggregation and backbone planarization. The shift in absorption peaks towards longer wavelengths with increasing annealing temperature, results in broader absorption range of the solar cell that is beneficial for the short-circuit current especially since after annealing the cell absorbs more closely to the maximum photon flux in the solar spectrum [5]. However, at higher temperatures, a reduced absorption is observed from figure 5.3 and reduced fill factor in figure 5.5.

Although the absorption increases with annealing time as shown in figure 5.4, optimized time for annealing is very crucial as long time heating may lead to degradation of the polymer layer causing an increase in series resistance and poor charge transport mobility.

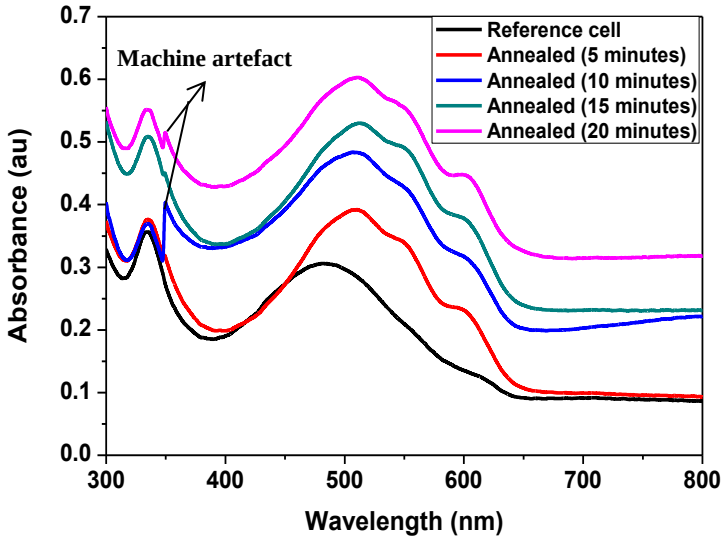


Figure 5.4 UV-Vis absorption spectra of P3HT: PCBM blend films as cast and after annealing at 50 ^{o}C ± 10 ^{o}C for 5 minutes, 10 minutes, 15 minutes and 20 minutes.

The increased absorption with annealing time could be attributed to rearrangement of the P3HT polymer chains in the blend forming a more aggregated (or crystallized) P3HT moiety which has an increased local density or with a lower free volume [6].

The increased intensity and red shifting of the absorption spectrum as a result of crystallization of the P3HT enhances the short circuit current due to generation of charge carriers. This is observed in *J-V* characteristic curve in figure 5.5.

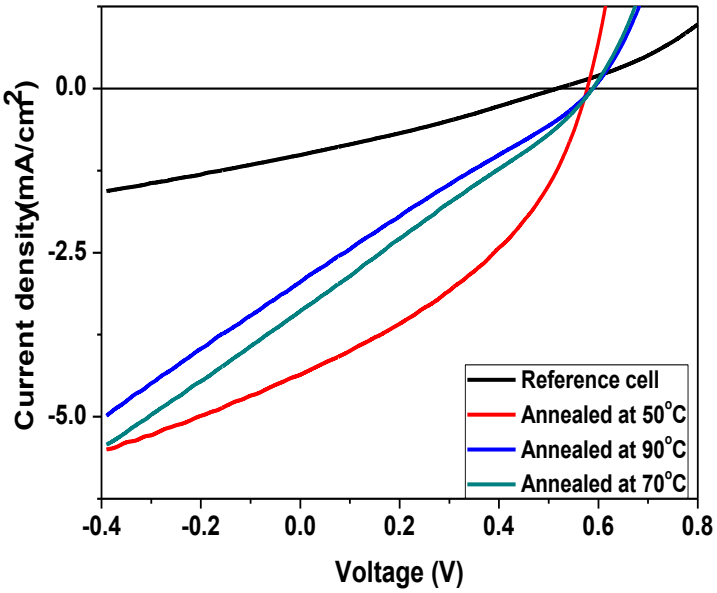


Figure 5.5 J-V characteristics (AM1.5, 70Mw/cm^2) of as-fabricated device and the annealed at 50 ^{o}C, 70 ^{o}C and 90 ^{o}C ± 10 ^{o}C for 10 minutes in Argon ambience.

Table 5-1 Summary of the performance of the OPVs as-fabricated and after annealing at different temperature for 10 minutes in Argon ambience.

Device	Jsc (mA/cm^2)	V_{oc} (V)	FF (%)	PCE (%)	R_s (Ω cm^2)	R_{sh} (Ω cm^2)
Reference	1.01±0.12	0.52± 0.02	31.8±1.2	0.16±0.10	54.4± 0.23	277.8 ± 13
Annealed at 50 ^{o}C	4.36±0.15	0.58± 0.02	41.9±1.1	1.02±0.08	4.6± 0.18	710.2 ±22
Annealed at 70 ^{o}C	3.39±0.13	0.59± 0.01	35.7±1.4	0.71±0.12	11.2± 0.36	439.1 ± 16
Annealed at 90 ^{o}C	2.95±0.12	0.59±0.12	34.3±0.6	0.59±0.12	13.6±0.22	436.7±21

Figure 5.5 shows *J-V* characteristics of P3HT:PCBM (1:1) devices annealed in Argon at different temperature (50 ^{o}C, 70 ^{o}C and 90 ^{o}C ± 10 ^{o}C) for 10 minutes). From the table of results annealing at 50 ^{o}C led to an increase in Jsc from 1.01 mA/cm^2 to 4.36 mA/cm^2. This could be due to the increased absorption efficiency (figure 5.3) as well as reduced resistivity of the blend layer. Charge transport in the organic semiconductors is due to intramolecular charge transport and intermolecular charge transport hence enhancing intermolecular packing and crystallization through thermal annealing ensures more efficient charge transport. This

enhanced charge transport can be seen in the reduced series resistance from 54.4 to 4.6 Ω cm^2. This shows that the series resistance of OPVs is greatly affected by the molecular packing of the conjugated polymer. Resistivity may results from the defects due to kink and torsional disorder along the conjugated polymer backbone. Reducing the kink and torsional disorder leads to densely packed backbone conjugated polymer with a reduced series resistance. Furthermore, densely packed conjugated polymer backbone may enhance more efficient intermolecular charge hopping [2]. Heat treatment may also enhance contact at the organic polymer-Aluminium interface by forming C-Al or C-O-Al covalent bonds hence lowering the injection barrier height. The reduction in resistivity resulted in an increase of FF from 31.8 to 41.9. The PCE increased from 0.16% to 1.02% due to the increased J_{sc} and FF. This remarkable improvement in PCE upon thermal annealing as a result of induced high crystallization or ordering of intra-chain interaction in P3HT chains [7-8] is quite instrumental before incorporation of Ag nanoparticles.

Annealing at higher temperature of 70 °C and above causes a deterioration of the device performance characterized by the reduced, J_{sc} and the FF. At high temperature, the polymers could get damaged, resulting in degradation of transport properties of the blend as well as deterioration of the contact with the electrodes [9].

Another parameter to consider during annealing process is time. Figure 5.6 shows the effect of time variation at a temperature of 50 ^oC in argon ambient.

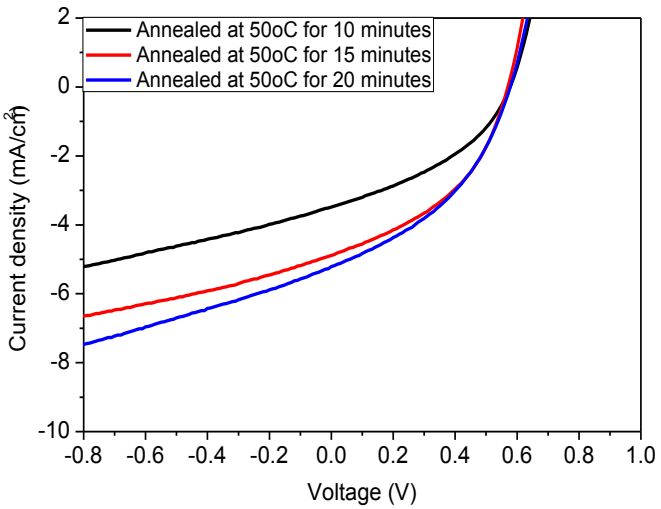


Figure 5.6 J-V characteristics (AM1.5, 70mW/cm^2) of as-fabricated device and the annealed at 10minutes, 15minutes and 20 minutes at a temperature of 50 ^{o}C ± 10 ^{o}C in Argon ambience.

Table 5-2 Summary of the performance of the OPVs upon annealing for different time interval at a temperature of 50 ^{o}C ± 10 ^{o}C in Argon ambience.

Device Annealed	Jsc (mA/cm^2)	V_{oc} (V)	FF (%)	PCE (%)
10 minutes	3.49±0.05	0.58± 0.04	37.6±0.8	1.08±0.06
15 minutes	4.90±0.11	0.58± 0.01	41.5±1.2	1.68±0.02
20 minutes	5.22±0.14	0.58± 0.13	40.3±1.0	1.74±0.05

Figure 5.6 shows that increased annealing time leads to an improved solar device performance. This is attributed to enhanced ordering of intra-chain interaction in P3HT chains and hence better carrier transport [6]. The short circuit current density gradually increases with increase in annealing time while the short circuit voltage remains relatively constant.

From this observation, it is evident that a lower temperature (50 ^{o}C) or a longer annealing time (20 minutes) is necessary to achieve optimized nano morphology of P3HT/PCBM blend for efficient charge separation and transport for optimal performance.

5.2 Absorption enhancement using NPs

Silver (Ag) NPs of varied sizes and inter-particle distance were developed using both RF sputtering and thermal evaporation on top of cleaned ITO coated glass as described in chapter 4 of this thesis. Spin coating of PEDOT:PSS and P3HT: PCBM was then carried out before metallization of the aluminum electrode. The architecture of the device with incorporated NPs is depicted in figure 5.7.

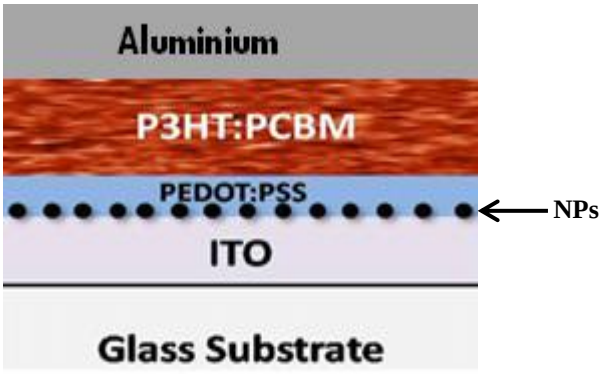
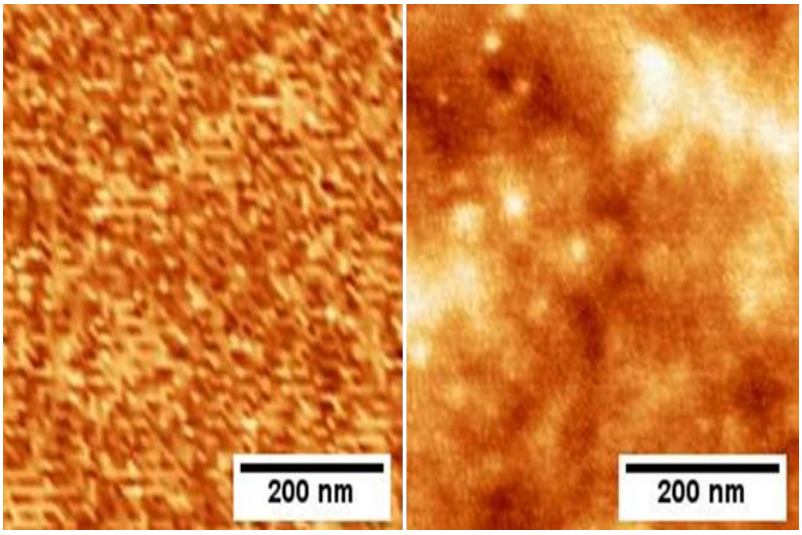


Figure 5.7 Device architectures of OSC with NPs on top of ITO.

The nanoparticles grown on top of the ITO film were annealed at 100 ^{o}C, 150 ^{o}C, 200 ^{o}C and 250 ^{o}C ± 10 ^{o}C respectively for 10 minutes in Argon ambience. Morphology check using tapping mode of AFM showed that NPs placed on top of the ITO do not affect the morphology of the polymer blend (fig 5.8a) in comparison with those placed on top of the active layer (fig5.8b). This shows that PEDOT:PSS fully covers the Ag islands. The identical polymer blend morphology in both reference and Ag nanoparticle embedded device is attributed to complete coverage of the Ag islands by the hole transport layer.



(a) **(b)**

Figure 5.8 Morphology of film of P3HT:PCBM blend with a) NPs beneath (On top of ITO) and b) NPs on top of the active layer.

The use of metal nanoparticles in organic semiconductors allows a considerable reduction in the physical thickness of absorber layers. This ensures that the thickness is in the range of diffusion length of the excitons as well as enhancing efficient light harvesting. This is achieved when the nanoparticles act as a subwavelength scattering elements to couple and trap freely propagating plane waves from the sun into the active layer by folding the light into the thin layer (fig 5.9a). This will lead to an increased effective path length in the layer. Strong local field enhancement around the noble metal nanoparticles may also act as subwavelength antennas in which the plasmonic near field is coupled to the active layer increasing its effective absorption cross-section (fig 5.9b). This ensures that the incident energy is stored in a localized surface plasmon mode.The metals may also enhance electromagnetic waves that travel along the interface between the metal back contact and the active layer (Surface plasmon resonance). See fig 5.9c. This can efficiently trap and guide light into the active layer [9-10] as shown in figure 5.9.

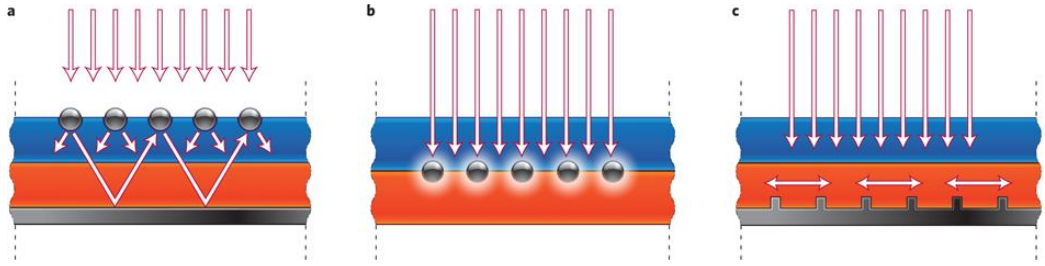


Figure 5.9 Different plasmonic geometries for light-trapping for thin-film solar cells adapted from Ref [9]

The incorporation of Ag nanoparticles resulting in efficient light absorption was observed in enhanced peaks from UV-Vis measurements shown in figure 5.10.

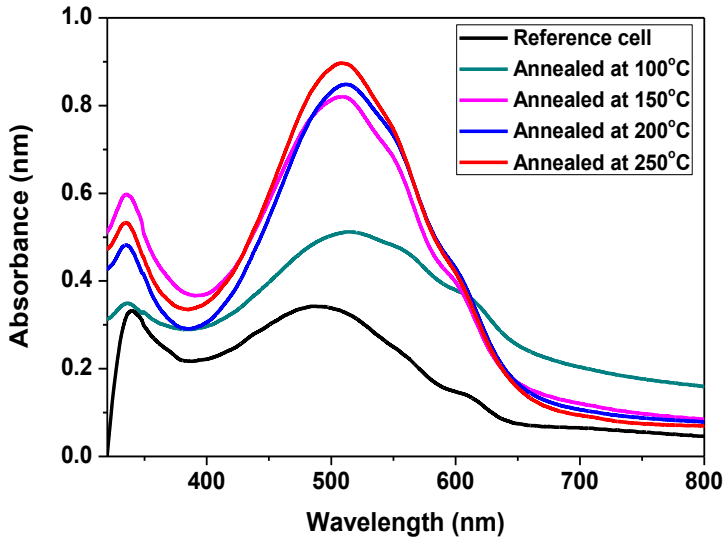


Figure 5.10. The optical absorption spectra of the P3HT:PCBM BHJ without NPs as well as with NPs annealed at 100 °C, 150 °C, 200 °C and 250 °C (the absorbance is baseline corrected with Indium tin oxide (ITO) coated glass as the reference standard).

Figure 5.10 illustrates the optical absorption of ITO/Ag nanoparticles/PEDOT:PSS/P3HT:PCBM film after Ag nanoparticles are annealed at different temperatures. A broad enhancement observed from 450 nm to 550 nm is attributed to the π-π* interaction of the P3HT while the absorption peak at 340 nm is attributed to PCBM. The reference device (black) shows a slight shift of absorption peak to higher wavelength as well as in intensity compared to reference in figure 5.4.

5.3 Device results and discussions

The NPs inside the OPVs could also act as the scattering centres which improve the photo conversion efficiency by increasing the optical path length inside the active layer. However, for Ag nanoparticles of diameter less than 100 nm, the light absorption cross-section is higher than the light scattering cross-section. In this study, the average particle radius used ranged between 39-71nm, therefore, the improvement in the performance of the OSCs would be prominently be related to the LSPR effect [11].

Annealing the Ag nanoparticles increases the size as well as the inter-particle distance leading to a shift in plasmonic absorption bands towards higher wavelength as discussed in chapter 4. The positioning of the Ag nanoparticles beneath the hole transport layer enhances the absorption intensity and produces a red shift in the absorption band as shown in figure 5.9. Furthermore thermal treatment promotes adhesion of islands to the substrate.

Figure 5.11 shows the J-V characteristics for devices fabricated with incorporated Ag nanoparticles upon annealing at 100 ^{o}C and 250 ^{o}C in Argon ambience.

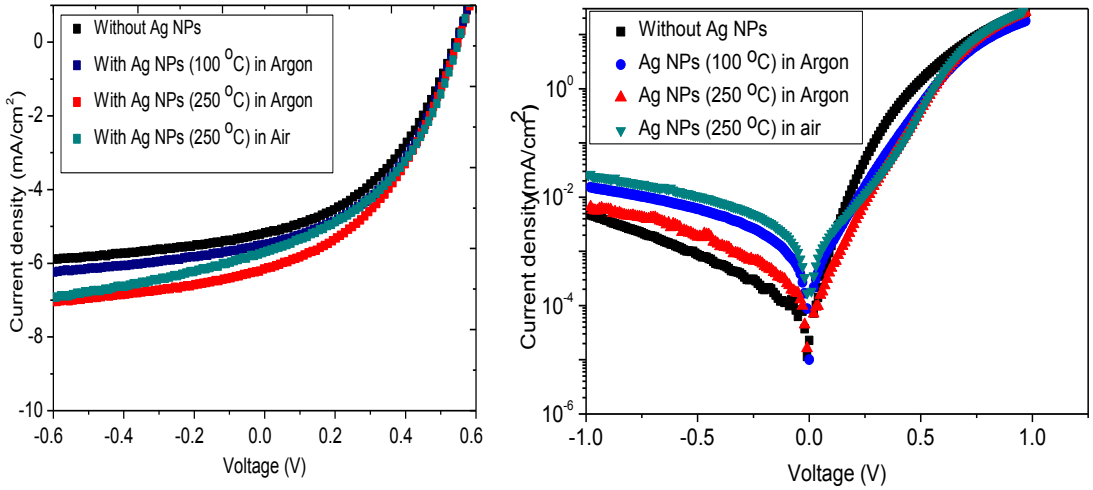


Figure 5.11 (a,) shows a *J–V* characteristics of both devices under illumination of devices with incorporated Ag sputtered on top of hole transport layer (ITO) and annealed at 100 ^{o}C and 250 ^{o}C while (b) is a semi-log plot of the J-V characteristics in the dark.

Table 5-3**.** Summary of the performance of the OPVs with different Ag nanoparticles size sputtered on top of the ITO.

Device	Jsc (mA/cm^2)	V_{oc} (V)	FF (%)	PCE (%)	R_s ($\Omega\ cm^2$)	R_{sh} ($k\Omega\ cm^2$)
Reference	5.05±0.12	0.54± 0.02	43.2±1.2	1.68±0.10	12.5± 0.23	20 ± 3
With Ag (100 °C)	5.47±0.15	0.54± 0.02	41.4±1.1	1.74±0.08	30.4± 0.68	10 ± 2
With Ag (250 °C)	6.16±0.13	0.55± 0.01	42.6±1.4	2.06±0.12	25.6± 0.56	19 ± 2
With Ag (250 °C) in air	5.68±0.10	0.54± 0.02	36.5±1.0	1.60±0.01	42.3±0.14	14± 1

The dark current in fig 5.11(b) shows elevated reverse saturation current suggesting that the Ag nanoparticles significantly introduced surface recombination centers, leading to a higher leakage current density. This is also adduced by the reduction in shunt resistance upon incorporation of Ag nanoparticles annealed at 100°C. However further increase in the Ag nanoparticles size engenders a protrusion through the hole transport layer (PEDOT:PSS) closer to the photoactive layer. Additional current pathways are formed through the cell which leads to reduced excitons quenching and charge recombination resulting into the increased shunt resistance [11]. Under AM 1.5 G filtered spectral illumination at incident intensity, 70 mW/cm^2, J_{sc} increased with incorporation of NPs due to the enhancement of the photogeneration of excitons near the plasmon resonance. The increase in J_{sc} for the large sized Ag nanoparticles of mean diameter of 71 nm is attributed to the formation of preferential current paths inside the hybrid layer through the particles, leading to substantial increase of the electric field between the electrodes. The large size particles created through high temperature resulting in islands of 71nm (at 250 °C) as reported earlier could create high field density points that extend to the P3HT:PCBM) as well as protrude through the PEDOT:PSS close to the P3HT:PCBM photoactive layer hence increasing contact interface between the anode and the photoactive layer providing relatively shorter routes for holes to travel to the anode hence enhancing hole collection efficiency of the anode [12]. The V_{oc} remained relatively the same

indicating that Ag nanoparticles addition does not alter the position of the HOMO level in the donor (P3HT) and the LUMO level in the acceptor (PCBM) respectively [11]. However, the specific series resistance (R_s) (slope of the $J-V$ curve at J=0 mA/cm^2) also increased to 30.4 Ω cm^2 for device with NPs annealed at 100 ^{o}C but reduced to 25.6 Ω cm^2 for the device with NPs annealed at 250 ^{o}C. The shunt resistance (R_{sh}) defined by the gradient at V=0 reduced to 10kΩ but later rose to 19kΩ upon incorporation of Ag nanoparticles annealed at 250 ^{o}C [13].

The deposition of annealed Ag nanoparticles on ITO-coated glass could also modify the charge transport and collection process through the anode due to their higher conductivity compared to PEDOT:PSS.

The reduction of series resistance by up to 16% upon annealing at 250 ^{o}C indicates remarkable improvement of the electrical properties of the device. From the results presented it is worth noting that incorporation annealed Ag nanoparticles not only enhances the optical response of the device but also its electrical properties being improved significantly.

The spectrophotometry results revealed that the absorption spectra of P3HT:PCBM became more intense and shifted towards higher wavelengths as compared to that without annealed Ag nanoparticles. In overall, the absorption enhancement from the metallic nanoparticles contributes to the overall photocurrent and efficiency of the device. It appears that the surface Plasmon's evanescent field coupling to the P3HT: PCBM blend extends to several nanometres to enable the absorption enhancement.

In air, the formation of $Ag_{2-x}O_x$ envelope when annealing is done at 250 ^{o}C could have led to increased series resistance resulting in low current density.

Reference

[1] Rodrigues, R., Meira, R., Ferreira, Q., Charas, A., & Morgado, J. (2014). Improving the Efficiency of Organic Solar Cells upon Addition of Polyvinylpyridine. *Materials*, *7*(12), 8189-8196.

[2] Kim, Myung-Su. *Understanding organic photovoltaic cells: Electrode, nanostructure, reliability, and performance*. ProQuest, 2009.

[3] Verploegen, E., Mondal, R., Bettinger, C. J., Sok, S., Toney, M. F., & Bao, Z. (2010). Effects of thermal annealing upon the morphology of polymer–fullerene blends. *Advanced Functional Materials*, *20*(20), 3519-3529.

[4] Sundberg, M., Inganäs, O., Stafström, S., Gustafsson, G., & Sjögren, B. (1989). Optical absorption of poly (3-alkylthiophenes) at low temperatures. *Solid state communications*, *71*(6), 435-439.

[5] Vanlaeke, P., Swinnen, A., Haeldermans, I., Vanhoyland, G., Aernouts, T., Cheyns, D., & Manca, J. V. (2006). P3HT/PCBM bulk heterojunction solar cells: Relation between morphology and electro-optical characteristics. *Solar energy materials and solar cells*, *90*(14), 2150-2158.

[6] Kim, H., So, W., & Moon, S. (2006). Effect of thermal annealing on the performance of P3HT/PCBM polymer photovoltaic cells.

[7] Pitliya, P., Sun, Y., Garza, J. C., Liu, C., Gong, X., Karim, A., & Raghavan, D. (2014). Synthesis and characterization of novel fulleropyrrolidine in P3HT blended bulk heterojunction solar cells. *Polymer*, *55*(7), 1769-1781.

[8] Jørgensen, M., Norrman, K., & Krebs, F. C. (2008). Stability/degradation of polymer solar cells. *Solar Energy Materials and Solar Cells*, *92*(7), 686-714.

[9] Kim, Y., Choulis, S. A., Nelson, J., Bradley, D. D., Cook, S., & Durrant, J. R. (2005). Device annealing effect in organic solar cells with blends of regioregular poly (3-hexylthiophene) and soluble fullerene. *Applied Physics Letters*, *86*(6), 3502.

[10] Atwater, H. A., & Polman, A. (2010). Plasmonics for improved photovoltaic devices. *Nature materials*, *9*(3), 205-213.

[11] Etebari Alamdari, N. (2013). *Mixed Plasmonic Nanoparticles for Enhanced-Performance Organic Solar Cells* (Doctoral dissertation, Concordia University).

[12] Zhang, Y., Yip, H. L., Acton, O., Hau, S. K., Huang, F., & Jen, A. K. Y. (2009). A simple and effective way of achieving highly efficient and thermally stable bulk-heterojunction

polymer solar cells using amorphous fullerene derivatives as electron acceptor. *Chemistry of Materials, 21*(13), 2598-2600.

[13] Kalfagiannis, N., Karagiannidis, P. G., Pitsalidis, C., Hastas, N., Panagiotopoulos, N. T., Patsalas, P., & Logothetidis, S. (2014). Performance of hybrid buffer Poly (3, 4-ethylenedioxythiophene) poly (styrenesulfonate) layers doped with plasmonic silver nanoparticles. *Thin Solid Films, 560*, 27-33.

Chapter 6 Encapsulation using Pentacene

6.1 Degradation mechanisms

Recent research efforts have aimed at optimising the device performance of organic photovoltaics by studying the efficiency enhancements through device geometry and phase morphology. However, to realize commercialization of organic solar cells, the device stability, cost as well as processing must be looked into. Traditionally non encapsulated organic polymers have shown a limited lifetime of the order of 1 day compared to their inorganic counterparts which possess lifetimes in excess of 25 years [1].

Some of the earliest study on the importance of degradation and stability include work by Yu *et al* . In their findings, devices kept in the dark had a stability of over 3 months under a low illumination intensity of 20 $mWcm^{-2}$ [2]. In this project we explore the study of the stability of devices by analysis of the degradation mechanisms.

6.2 Chemical degradation.

Chemical degradation of organic solar cells is usually as a result of reaction with oxygen and water as well as aluminium electrode reaction with the active polymer layer. The devices in this project were all fabricated in air. UV illumination of the devices easily activated oxygen in the presence of organic molecules forming superoxide or hydrogen peroxide capable of attacking the active polymer.

6.21 Effect of oxygen and water in device.

In air ambience, water and oxygen diffuse into the device leading to the degrading of the performance of the solar cell. The diffusion into the active layer is mainly through the microscopic pinholes in the outer electrodes. Moreover, the diffusion may also be through the metal grains making up the evaporated electrodes. Entry of oxygen causes a sublayer of the organic material to be oxidized causing the material to expand in all directions. This may lead to formation of either hillocks to the outer electrode and microscopic pinholes at the centre of the outer electrode surface [3]. The diffusion through the microscopic metal grains is found to

take place regardless of whether device is illuminated or stored in darkness; however, it is accelerated by UV illumination. Furthermore, oxygen may also diffuse through the active layer uncovered by the aluminum electrode.

6.22 Effect of photochemistry and photo-oxidation

Most conducting polymers are susceptible to photo-oxidation resulting in reduced lifetime of the devices. This degradation occurs when singlet oxygen is formed by energy transfer from photo-exited polymer to adsorbed ground state oxygen molecules. This occurs when the polymer has higher energy than the singlet state of oxygen for energy exchange to take place. The intersystem crossing from the polymer excited state to the triplet states may be favored. Moreover, the triplet states must be long lived enough to boost the probability of the energy exchange. If all these are met, then the singlet oxygen reacts with the vinylene groups in conducting polymers through a 2+2 cyclo addition reaction before the intermediate adduct breaking down leading to chain scission [4]. P3HT used in this project as a donor, may have their simple thiophenes reacting with oxygen at low temperatures under irradiation forming thio-ozonides which may further degrade at room temperature [5].

6.23 Chemical degradation of the Aluminum electrode.

According to Lögdlund et al, aluminum reacts with conducting polymer at the inter-face forming Al-C bonds leading to single-electron transfer creating anion radicals on the polymer. These anion radicals are highly reactive species and thus may react with proton donors such as traces of water introduced by PEDOT:PSS during device fabrication. This may lead to reduction of vinylene groups hence loss in conjugation [6]. PCBM used as an electron acceptor has a high electron affinity thus more likely to react with metal electrodes. According to Nishanaga et al., molecular distortion induced by Al-C_{60} bonding may permit the formation of the symmetry forbidden HOMO-LUMO transition [5]. Although the Al-C_{60} interaction may

enhance charge transport across the interface, this can only be efficient when a buffer layer is placed or when the C_{60} is slightly doped. In organic solar cells, an ultra-thin layer of lithium fluoride may be used between aluminum and polymer to act as a buffer layer. This according to Brabec et al.: lowers effective work function; eliminates reaction between aluminum and the polymer; leads to formation of a dipole layer and may also lead to protection of the polymer layer from alumina during thermal evaporation of the aluminum electrode [7].

6.24 Chemical degradation of ITO electrode

According to Jong et al., indium contents increased on the PEDOT:PSS layer when a device is kept in nitrogen atmosphere. The rate of erosion of ITO film increases when the device is exposed to air. This is attributed to ITO/PEDOT interface being highly sensitive to air and that the hygroscopic nature of PSS may permit water absorption leading to etching of the ITO layer.

6.25 Degradation of PEDOT:PSS film

Poly(ethylenedioxythiophene) poly(styrene sulfonic acid) is usually used to facilitate hole injection/extraction. It can also be used to improve surface quality of the ITO electrode due to its higher conductivity and better film-forming ability. This helps in reducing pinhole density and stifling current leakage that occurs along shunting paths. Furthermore, it may be used to modify the work function of ITO by chemical/electrochemical redox reactions [8]. However, it may contribute to the overall degradation of the organic solar device. According to Pacios et al., hydroscopic PEDOT:PSS layer takes up water from the atmosphere leading to an increase in sheet resistance [9]. Norman et al. on the other hand suggests that PSS which is normally in excess compared to PEDOT, may diffuse into the device possibly reacting with other components of the device. Moreover, PSS undergoes what Norman *et al*. calls oxido-de-sulfonato-substituition resulting in phenolate which may ultimately react with PSS to form two

PSS chains linked together through sulfonic ester group. Carbon in this group may easily be oxidized changing the molecular structure of the particles [10].

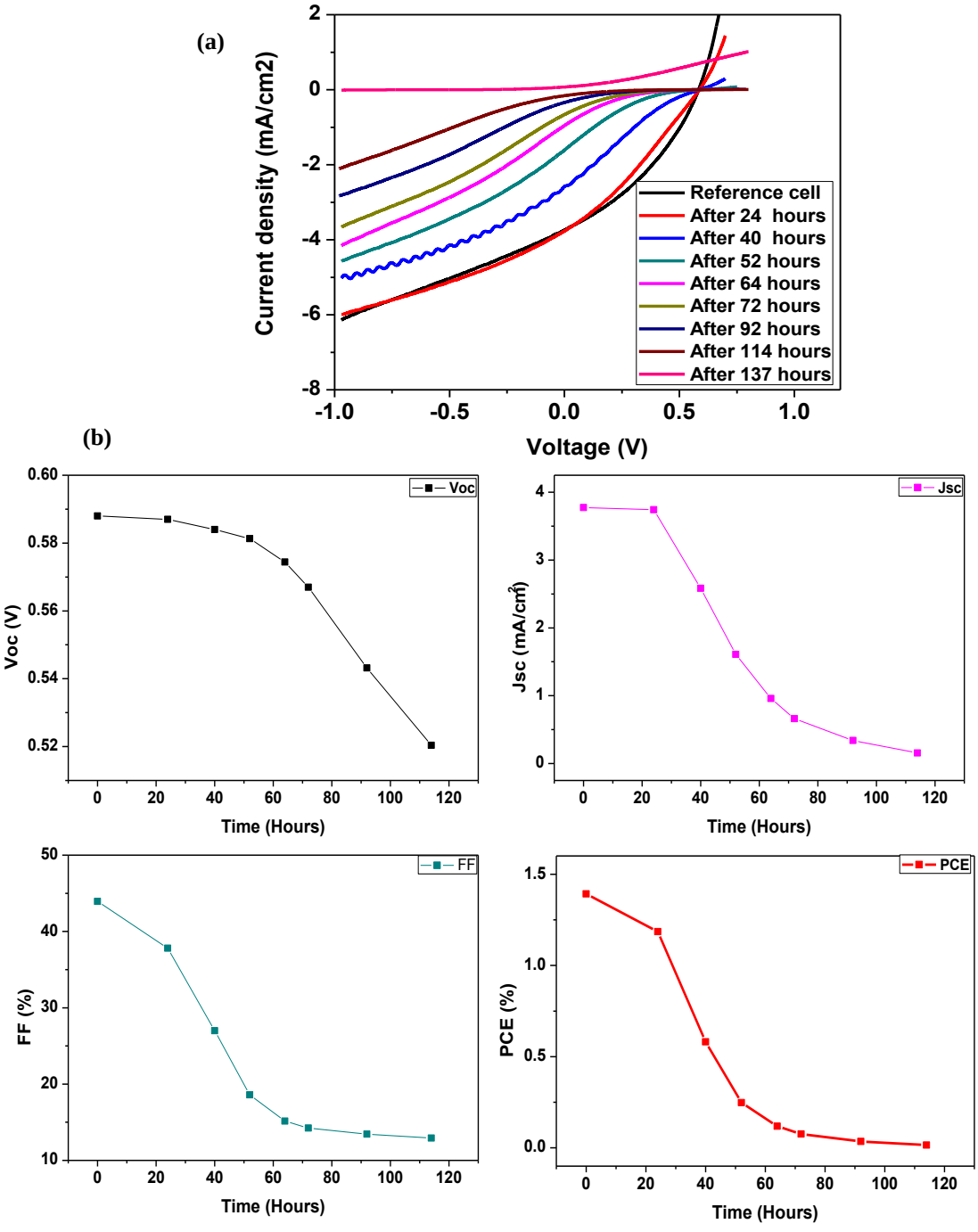
6.3 Physical and mechanical degradation mechanisms

The efficient functioning of organic solar cell device greatly depend on the spatial organization of the different materials into layers spin coated such that they attain precise thickness in order to realize optimum photon harvesting and charge-carrier transport. One class of particular interest is the concept of BHJ. This constitutes a network of nano-separated domains of an electron donor and an electron acceptor formed from a blend of a conjugated polymer with a fullerene derivative. The optimal blend should have a nanophase separation of the active layer into an interpenetrating network of donor and acceptor material. Maintaining such structure is not certain during the device fabrication. P3HT and PCBM used as donor and acceptor respectively have small organic molecules with some freedom to diffuse slowly or recrystallize over time moreso at elevated temperature. Therefore, even the best structure for device performance will not have 100% probability of being thermodynamically stable [5]. The OPVs are therefore prone to degradation as a result of the gradual changes in the microstructure.

6.31 Morphology degradation

The BHJ organic solar cell makes it possible for exciton diffusion within the small diffusion range normally in the order of 10 nm. Such small diffusion lengths ensure that continuous paths to the outer electrodes for the charges formed at the donor-acceptor interface are attained. However, obtaining optimal nanophase separation still remains a challenge. This is because, apart from thermodynamic effect, it also depends on the kinetics of segregation and crystallization of the donor and the acceptor respectively. Achieving optimal morphology

depends on various factors such as choice of solvent, concentration ratios of donor and acceptor, temperature and speed and time of spin coating as well as post annealing effect. According to Klimov *et al* [11] and Yang *et al* [12] post annealing of P3HT:PCBM blend results in a more stable morphology with a long device lifetime. The degradation mechanisms mentioned previously impacts on the OPV devices through gradual loss of the benchmark parameters such as V_{oc}, Jsc, FF and PCE as illustrated in figure 6.1



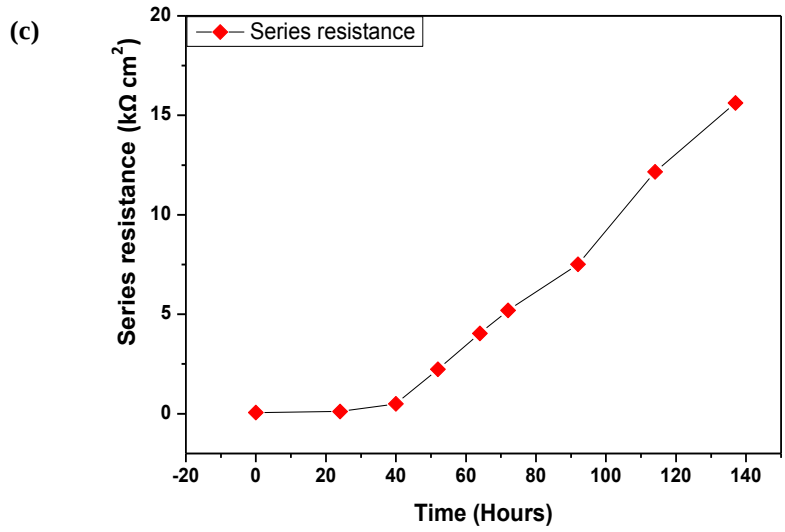


Figure 6.1 a) I-V characteristics for ITO/PEDOT:PSS/P3HT:PCBM/Al solar device degrading with time in air ambience b-c) Photovoltaic performance of unencapsulated device as a function of exposure time to ambient air under AM 1.5 G filtered spectral illumination at incident intensity, 70 mW/cm^2.

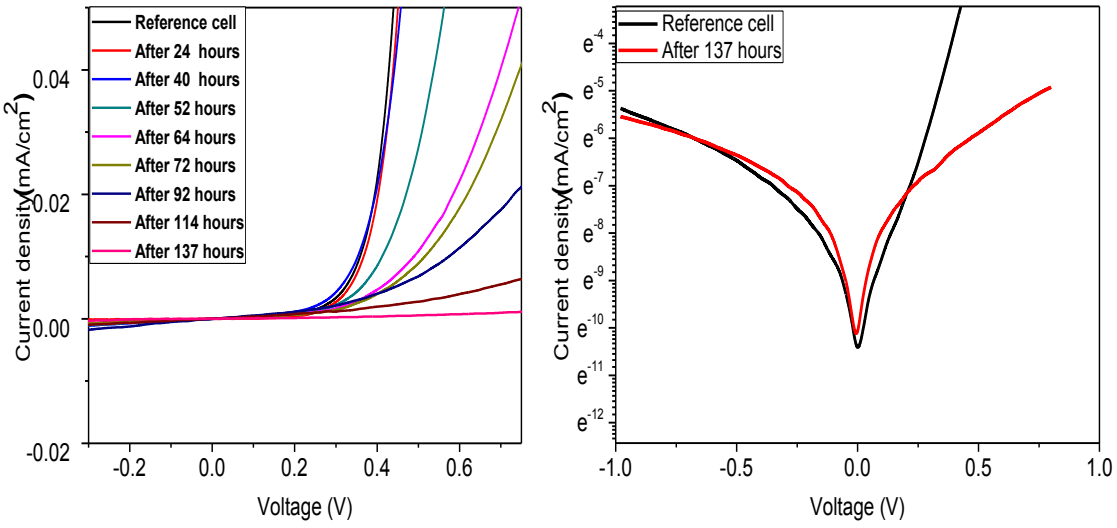


Figure 6.2 (a) I-V characteristics for ITO/PEDOT:PSS/P3HT:PCBM/Al solar device in the dark as a function of time in ambient air (b) Semi-log graph of reference device compared to device after 137 hours.

Figure 6.1 and 6.2 shows photovoltaic response of the reference solar cell (ITO/PEDOT:PSS/P3HT:PCBM/Al) as a function of exposure time to ambient air. I-V characteristics data shown represents cells measured both in the dark and under continuous simulated AM1.5 solar irradiation of ~100mWcm^{-2}. The V_{oc}, Jsc, FF and PCE first gradually

degrade within the first 24 hours before a distinct trend of rapid degradation. The J_{sc}, FF and PCE later on after 65 hours gain a relatively low degradation rate. The loss in J_{sc} may be due to introduction of photo-activated interfacial states caused by the rapid degradation due to oxygen induced doping of P3HT:PCBM. This is corroborated by increase in series resistance with time shown in figure 6.1(c). These interfacial states or increased trapping density may lead to increased series resistance that in turn inhibits charge extraction/transport. Besides, absorption/desorption of water by the PEDOT:PSS layer may also adversely affect the performance as this results in poor transport at the PEDOT:PSS interfaces as well as PEDO:PSS bulk. V_{oc} on the other side is determined by the HOMO-LUMO difference of the donor and acceptor materials respectively as well as the work function difference of the electrodes. The slow degradation of V_{oc} in the first 24 hours shows that there is no significant change in the nano-morphology with aging and that the interconnected network is marginally affected as well, this is consistent with the absorption data of fig 6.3. The decrease in absorption could be an interface effect but the absorption finger prints of the polymer fullerene blend remain unchanged. Since PEDOT:PSS is hydroscopic in nature, it may absorbs water from the surrounding causing an alteration in carrier density in PEDOT:PSS close to the interface or formation of a dipole layer at the interface leading to reduced work function. Besides, PEDOT:PSS may etch part of ITO making it possible for indium to diffuse from ITO into the active layer. This change causes a reduction in work function of ITO/PEDOT:PSS interface leading to reduced work function difference between the two electrodes hence low V_{oc}. The FF showed a first rapid degradation before slowing down after 60 hours. After 40 hours, FF reduced drastically such that the illuminated characteristics showed an S-shape curve. The reduction in FF was caused by a change in series and shunt resistances, reduced charge carrier mobilities in P3HT:PCBM blend as well as introduction of traps that in turn act as recombination centres affecting the distribution of electric field in the device. Moreover, the

reduction in FF may also be attributed to formation of space charges due to imbalance in charge carrier mobilities as a result of degradation. BHJ solar cells have 100% exciton diffusion probability. This reduces drastically due to degradation as a result of formed traps that minimize the mobility and lifetime of the charge carriers. A change in work function of the electrodes may lead to reduced internal electric field. This is the energy required to split an exciton and further reduces its diffusion length leading to an increase in recombination loses.

In such instances the excitons formed are unable to reach the donor-acceptor interface for dissociation to occur. This implies that only charge carriers close to the electrodes would be collected hence reducing the photocurrent [12].

The gradual followed by rapid degradation may also result from increasing oxygen intake by the P3HT and PCBM which corroborates with Norman *et al*. observation. Oxygen diffuses through the pinholes in the aluminum electrode causing a chemical degradation of P3HT forming a charge transfer complexes with oxygen which may lead to formation of cation and anion radical species. Sulphur from P3HT may also react with water or oxygen from the atmosphere leading to the degradation of the cell [3].

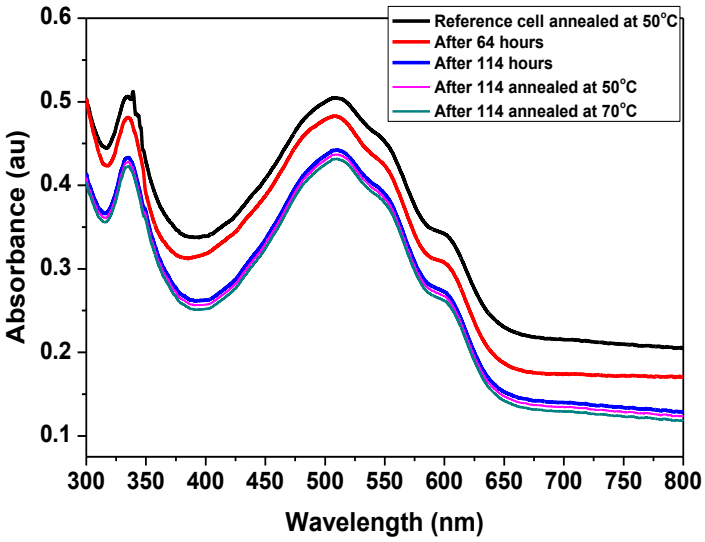


Figure 6.3 UV-Vis spectrometer measurement of absorbance of P3HT:PCBM film with time before annealing at 50 ^{o}C and 70 ^{o}C in Argon ambience.

In an attempt to verify the effect of air exposure on optical properties of organic solar device, the absorption of reference device annealed at 50 ^{o}C after exposure to air was measured using UV-Vis spectrometer as shown in figure 6.3. From figure 6.3, the absorbance of the BHJ film reduces with significant drop in the vibronic peaks at 360, 520, 550 and 600 nm as a result of photo-oxidation or photo bleaching. It is interesting to note that after an exposure of 114 hours to air, the film lost its absorbance significantly. We then annealed the device at 50 ^{o}C and another at 70 ^{o}C for 10 minutes and measured absorbance. After thermal treatment in Argon ambience, the film absorbance was never reset to its pristine value. This experiment clearly shows that photo-oxidation is an irreversible process.

6.4 Growth and characterization of pentacene.

Ricardo et al. defines Pentacene ($C_{22}H_{14}$) as a planar molecule consisting of five benzene rings with triclinic structure in its bulk phase with lattice constants a=7.90 Å, b=6.06 Å and c=16.01 Å, bandgap of 2.5 eV, ionization potential of 5.1 eV for an electron in the HOMO level. It has a relative dielectric constant of 4 and effective density of states of 5.8×10^{21} cm $^{-3}$. When grown in vacuum, pentacene assumes "thin film phase" structure. At pentacene/inorganic interfaces, the orientation of pentacene molecules depends on the molecular interactions between pentacene and the substrate. Usually when deposited on metals and reactive semiconductors form structures with the molecules lying flat on the surface that are quite stable.

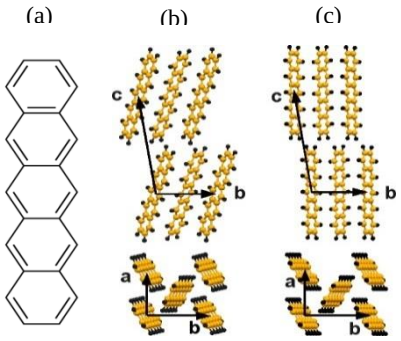


Figure 6.4 (a) Molecular structure and (b) triclinic bulk structure of pentacene (c) thin film phase.

Pentacene has gained a lot of research interest as a model molecule among organic semiconductors as a result of its ability to form well-ordered polycrystalline thin films that show a high charge carrier mobility of $1cm^2V^{-1}s^{-1}$and even above have been recorded. This is due to the efficient π-orbital overlap between its molecules [13-16]. Thus it can be used as a hole transport layer when encapsulated on a Ag nanoparticle.

6.5 Experimental results

ITO coated glass was cleaned in ultrasonic distilled water-acetone-methanol-ethanol-distilled water baths in that order before drying with Nitrogen. NPs were then grown and annealed in Argon ambience and then placed in a thermal evaporator that was then evacuated using rotary and diffusion pump to a pressure of 1.5 x 10^{-5} mbar. The solid pentacene source was heated to 170 - 200 °C during the deposition. The Ag nanoparticles on ITO acting as the substrate were kept at room temperature during the evaporation of pentacene. The deposition rate was monitored using the crystal monitor that showed the film thickness of 22.2 nm.

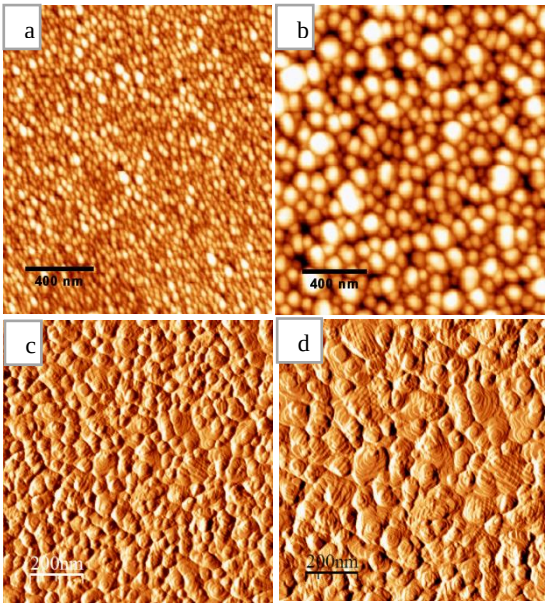


Figure 6.5 (a-b) AFM image of RF sputtered Ag nanoparticles annealed at 100 ^oC and 250 ^oC respectively in Argon ambience (c-d) 22.2 nm evaporated pentacene on the annealed Ag nanoparticles.

From the morphology studies using Veeco Di 300 AFM, pentacene thin film on Ag nanoparticles shows rough surface with voids that may modify the electronic states associated with the molecules surrounding each vacancy. This molecular vacancies may trap or scatter charge carriers. The distortion of the crystalline lattice near vacancies can usually be used to determine the energy required to form the vacancy and the thermodynamic stability of this defect. According to Craig et al. the environment with relaxed molecules surrounding a vacancy is energetically more stable than that in a perfect crystal [17]. However, the deformed lattice near a vacancy may change the electronic states of molecules in the vicinity of the defect region. Such distortion in the crystalline lattice may lead to formation of traps for charge carriers [13] as witnessed in the I-V characteristics later in this thesis.

Thin film of pentacene on top of annealed Ag nanoparticles may couple with the surface plasmons to produce enhanced absorption as shown in figure 6.5.

Pentacene thin film on its own may experiences singlet and triplet exciton formation on an ultrafast time that may be due to polymorphism. It may also exhibit singlet fission, i.e. splitting of a singlet exciton into two triplets hence the multiple absorption peaks.

From the UV-Vis measurements shown in figure 6.6, pentacene thin film has four different absorption peaks with energies of 1.85 eV (at λ= 671 nm) , 1.97 eV (at λ= 630 nm), 2.12 eV (at λ= 585 nm) and 2.27 eV (at λ= 545 nm). Since the excited states in pentacene thin film are singlet states, the excitation at λ= 671 nm can be assigned to the S_1 state while that at λ= 630 nm corresponds to the second level of the Davydov doublet after Davydov splitting. The absorption bands at λ= 545 nm (2.27 eV excitation) corresponds to an electron-hole pair, which is situated on two neighboring molecules of adjacent unit cells while that at λ= 585 nm may be due to a charge transfer state with the hole and electron being at the sites of the two molecules of one unit cell [18].

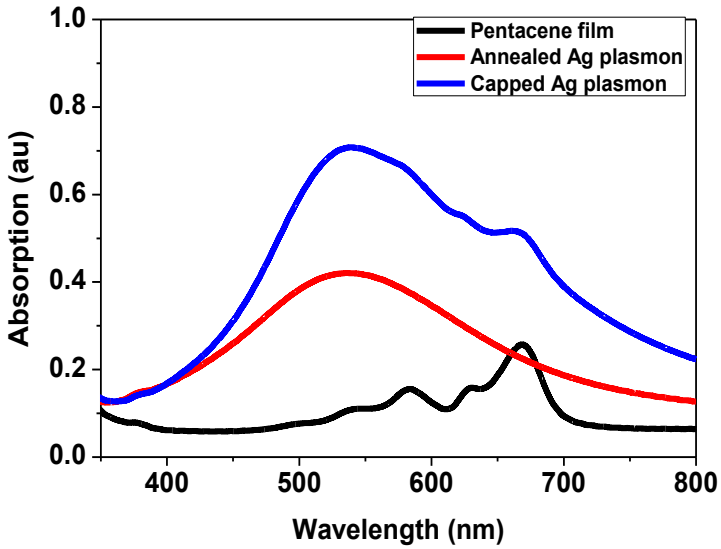


Figure 6.6 UV-Vis spectrometer measurement of absorbance of pentacene film on top of annealed Ag nanoparticles.

The black line shows that pentacene film has multiple absorption peaks which are useful in enhancing absorption of Ag nanoparticles as shown by the blue line. This could also be as a result of coupling of pentacene with the surface plasmonic resonance.

When P3HT:PCBM blend was spin coated on top of the pentacene film, a different dielectric environment is created producing an enhanced absorption as shown in figure 6.7.

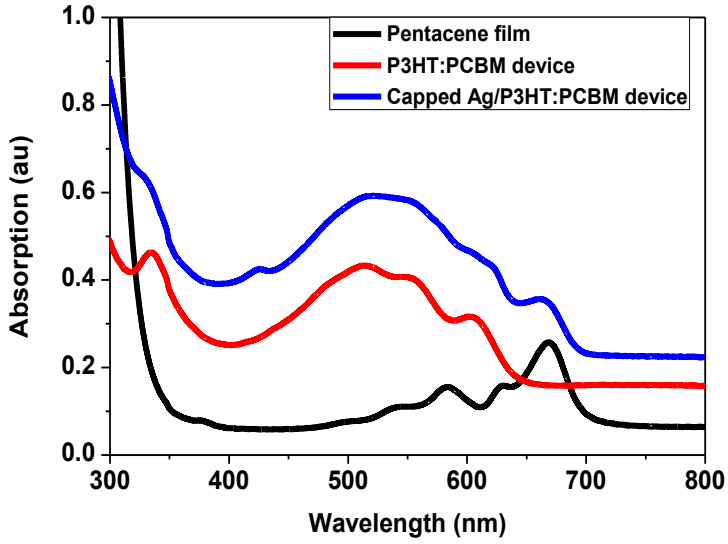


Figure 6.7 UV-Vis spectrometer measurement of absorbance of PEDOT:PSS, P3HT:PCBM active layer on top of annealed Ag nanoparticles encapsulated with pentacene thin film.

The conspicuous enhanced absorption at a wavelength of 670 nm extends the absorption spectrum of the active layer to a higher wavelength. This is needed for multiple absorption tuning in the active layer of the device. However the conductivity of the encapsulated layer remains a fundamental parameter in the determination of the current that flows within the solar cell. From figure 6.8, pentacene introduces a contact barrier of ~0.8 eV. This could cause hole trapping at the PEDOT:PSS-pentacene interface leading to reduces J_{sc}.

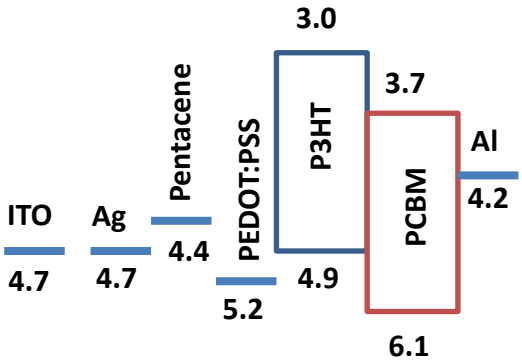


Figure 6.8 Band energy diagram for ITO/Ag nanoparticles/Pentacene/PEDOT:PSS/P3HT:PCBM/Al device.

Despite the clear absorption enhancement upon encapsulation of Ag nanoparticles with pentacene, the J_{sc}, V_{oc}, FF and PCE drastically reduced but with improved device stability when exposed to air ambience as shown figure 6.8.

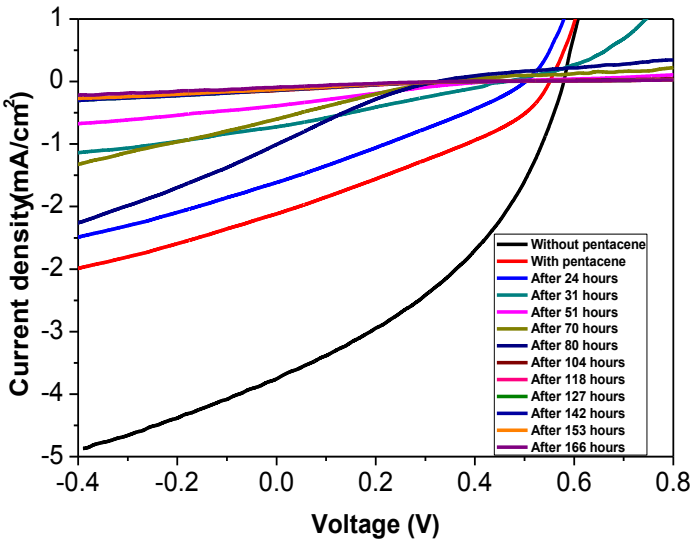


Figure 6.9 I-V characteristics for ITO/PEDOT:PSS/P3HT:PCBM/Al solar device degrading with time in air ambience under AM 1.5 G filtered spectral illumination at incident intensity, 70 mW/cm^2.

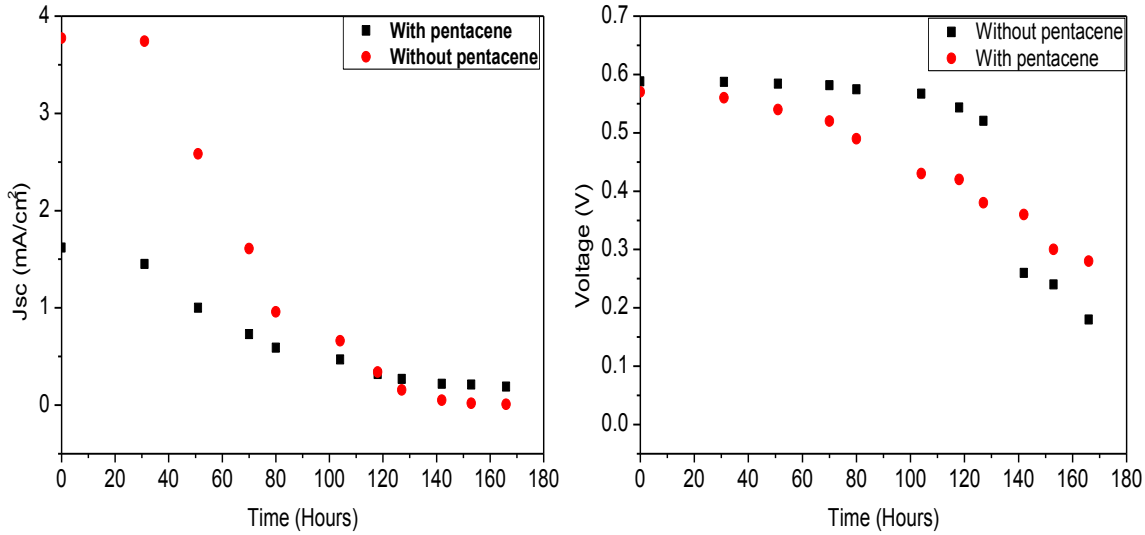


Figure 6.10 Photovoltaic performance of encapsulated device as a function of exposure time to ambient air.

Analysis of J_{sc} shows that devices without pentacene encapsulation acquired same value as the one with encapsulation after 118 hours despite its high original J_{sc} upon fabrication, thus encapsulation reduces the rate and magnitude of degradation. Beyond this time, the encapsulated device showed a greater J_{sc}. A similar trend was seen with the V_{oc} where after 140 hours, encapsulated plasmonic device recorded a higher V_{oc} compared to the device without encapsulation. The long electrical activity upon encapsulation could be as a result of pentacene forming a thin layer that separates PEDO:PSS from ITO. In this case the pentacene prevents the etching of ITO layer by the acidic PEDOT:PSS. The encapsulation of Ag nanoparticles could also be used for passivation of the silver surface hence reducing the rate of oxidation of the Ag nanoparticle that could reduce the plasmonic absorption. However such passivation only requires a very thin layer in order not reduce the field around the nanoparticles as well as molecular self-assembly to enhance charge transport due to better π orbital alignment.

The reduced J_{sc} compared to plasmonic devices without encapsulation can be attributed to formation of large Schottky barrier (~ 0.7 eV) between pentacene and Ag nanoparticles

resulting in a large contact resistance between the ITO electrode and the active layer due to mismatch of their Fermi energy.

Reference

[1] Norrman, K., N. B. Larsen, and Frederik C. Krebs. "Lifetimes of organic photovoltaics: combining chemical and physical characterization techniques to study degradation mechanisms." *Solar energy materials and solar cells* 90.17 (2006): 2793-2814.

[2] Donkor, E., Viswanath, A. K., Pearton, S., Lee, J., Gomes, W. P., Xiang, X. & Stepanov, S. (2001). Handbook of advanced electronic and photonic materials and devices. *Handbook of Advanced Electronic and Photonic Materials and Devices: Conducting polymers*.

[3] Norrman, K., Madsen, M. V., Gevorgyan, S. A., & Krebs, F. C. (2010). Degradation patterns in water and oxygen of an inverted polymer solar cell. *Journal of the American Chemical Society*, *132*(47), 16883-16892.

[4] Scurlock, R. D., Wang, B., Ogilby, P. R., Sheats, J. R., & Clough, R. L. (1995). Singlet oxygen as a reactive intermediate in the photodegradation of an electroluminescent polymer. *Journal of the American Chemical Society*,*117*(41), 10194-10202.

[5] Jørgensen, M., Norrman, K., & Krebs, F. C. (2008). Stability/degradation of polymer solar cells. *Solar Energy Materials and Solar Cells*, *92*(7), 686-714.

[6] Jin, H., Tuomikoski, M., Hiltunen, J., Kopola, P., Maaninen, A., & Pino, F. (2009). Polymer− electrode interfacial effect on photovoltaic performances in poly (3-hexylthiophene): phenyl-c61-butyric acid methyl ester based solar cells. *The Journal of Physical Chemistry C*, *113*(38), 16807-16810.

[7] Bra Brabec, C. J., Shaheen, S. E., Winder, C., Sariciftci, N. S., & Denk, P. (2002). Effect of LiF/metal electrodes on the performance of plastic solar cells. *Applied Physics Letters*, *80*(7), 1288-1290.

[8] Frohne, H., Shaheen, S. E., Brabec, C. J., Müller, D. C., Sariciftci, N. S., & Meerholz, K. (2002). Influence of the anodic work function on the performance of organic solar cells. *ChemPhysChem*, *3*(9), 795-799.

[9] Pacios, R., Chatten, A. J., Kawano, K., Durrant, J. R., Bradley, D. D., & Nelson, J. (2006). Effects of Photo-oxidation on the Performance of Poly (2-methoxy-5-(3', 7'-dimethyloctyloxy)-

1, 4-phenylene vinylene):(6, 6)-Phenyl C61-Butyric Acid Methyl Ester Solar CellsFNR HREF=" fn1"> FN ID=" fn1"> We.*Advanced Functional Materials*, *16*(16), 2117-2126.

[10] Norrman, K., Larsen, N. B., & Krebs, F. C. (2006). Lifetimes of organic photovoltaics: combining chemical and physical characterization techniques to study degradation mechanisms. *Solar energy materials and solar cells*, *90*(17), 2793-2814.

[11] Klimov, E., Li, W., Yang, X., Hoffmann, G. G., & Loos, J. (2006). Scanning near-field and confocal Raman microscopic investigation of P3HT-PCBM systems for solar cell applications. *Macromolecules*, *39*(13), 4493-4496.

[12] Yang, X., Loos, J., Veenstra, S. C., Verhees, W. J., Wienk, M. M., Kroon, J. M., ... & Janssen, R. A. (2005). Nanoscale morphology of high-performance polymer solar cells. *Nano letters*, *5*(4), 579-583.

[13] Seo, S. (2010). *Structural and electronic properties of pentacene at organic-inorganic interfaces*.

[14] Ruiz, R., Choudhary, D., Nickel, B., Toccoli, T., Chang, K. C., Mayer, A. C., ... & Malliaras, G. G. (2004). Pentacene thin film growth. *Chemistry of Materials*,*16*(23), 4497-4508.

[15] Yernagula, J. (2005). C*ontact effects in thermally evaporated pentacene thin films and aspects of mircrosystem hybrid integration* (Doctoral dissertation, Faculty of the Louisiana State University and Agricultural and Mechanical College in partial fulfillment of the requirements for the degree of Master of Science in Electrical Engineering in The Department of Electrical and Computer Engineering by Jagadish Yernagula B. Tech., Jawaharlal Nehru Technological University).

[16] Klauk, H., Halik, M., Zschieschang, U., Schmid, G., Radlik, W., & Weber, W. (2002). High-mobility polymer gate dielectric pentacene thin film transistors.*Journal of Applied Physics*, *92*(9), 5259-5263.

[17] Craig, D. P., Markey, B. R., & Griewank, A. O. (1979). Structural disturbance and lattice relaxation in molecular crystal packing calculations. *Chemical Physics Letters*, *62*(2), 223-229.

[18] Fiebig, M. (2010). *Spatially resolved electronic and optoelectronic measurements of pentacene thin film transistors* (Doctoral dissertation, lmu).

Chapter 7. CONCLUSIONS AND RECOMMENDATIONS

7.1 Conclusion

This research project focused on Ag and Au nanoparticles grown by physical vapor technique and incorporated into organic solar cells on top of the ITO coated glass with the aim of enhancing efficiency through increased light absorption due to surface plasmon resonance effect. The Ag nanoparticles were grown using both thermal evaporation and RF sputtering system. In addition, the power and time of deposition was varied with a view of obtaining correct sizes capable of being covered by the PEDOT:PSS such that the centers of the nanoparticles are close to the active layer but not protruding through the active layer that may make them interfere with active layer morphology or even short circuit the cell. The nanoparticles were then annealed both in air and Argon ambience to vary their geometry, density, size and shape in an attempt to obtain match between their resonance peaks and maximum absorption. As deduced from the characterization data, Ag nanoparticles annealed at 250 ^{o}C showed a reduced surface coverage up to 38% with particle mean diameter of 71nm. An attempt to anneal Ag nanoparticles in air ambient showed different results from samples produced at the same time. This could be as a result of oxidation which varies depending on the environmental condition of the day.

In order to understand the mechanisms responsible for enhancing efficiency, a reference cell was fabricated with ITO/PEDOT:PSS/P3HT:PCBM/Al structure. This device was then annealed at different temperatures and time interval in order to realize most effective reference cell. The device performance upon annealing improved and annealing at 50 ^{o}C for 10 minutes showed best performance resulting in 3 times the J_{sc} and 5 times PCE. Higher temperatures caused deterioration of the device giving low J_{sc} and PCE.

The Ag nanoparticles with different sizes and shape resulting from annealing effect were then incorporated into the device. They were grown on ITO before completing the device. In

making the device PEDOT:PSS was first spin-coated followed by P3HT:PCBM blend before thermally evaporating Al electrode to form ITO/ Ag NPs/PEDOT:PSS/ P3HT:PCBM/ Al structure. A morphology check using tapping mode AFM showed that the Ag nanoparticles did not interfere with the morphology of the active layer. The optical characterization using UV-Vis spectrometer showed enhanced absorption with increasing particle sizes. This was also reflected in enhanced J_{sc} and PCE though FF and V_{oc} remained relatively constant.

Enhancement in light harvesting is believed to have led to greater exciton generation leading to increase in J_{sc} and PCE. The results showed a significant efficiency enhancement upon incorporation of annealed NPs. The PCE and J_{sc} went up by 24% and 23% respectively for NPs annealed at 250 ^{o}C.

We further explored the potential causes of degradation, degradation trend as well as effect of encapsulation of Ag nanoparticles before incorporation into organic solar cells.

Air exposure of ITO/Ag nanoparticles/PEDOT:PSS/P3HT:PCBM/Al device showed a gradual, followed by rapid degradation. This was more so when the devices were illuminated in air. The degradation could result from water absorption by PEDOT:PSS layer causing its degradation forming a spatially inhomogeneous that is associated with formation of insulating patches leading to loss of current and device efficiency. Another cause of degradation of OPVs could be resulting from change in electrode work function as the react with the PEDOT:PSS. The diffusion of oxygen into the active layer through the pinholes in the aluminum electrode causing a chemical degradation of P3HT forming a charge transfer complexes with oxygen could also have led to cell degradation.

Encapsulation of Ag nanoparticles using thin film of pentacene showed an improved stability to air as well as increased light absorption as seen from the UV Spectrometer measurement. However the J_{sc} reduced drastically probably due to introduced contact barrier of ~0.8 eV at the PEDOT:PSS- pentacene interface which could cause hole trapping.

7.2. Future work and Recommendations

There is need to vary device geometry during fabrication of devices with incorporated NPs to achieve a comparison in plasmonic effectiveness at various positions in the device.

Study of change in contacts angles on annealing of NPs and their effect on light absorption should be carried out in future.

The effect of tandem multi-junction should be investigated by incorporating both Ag and Au NPs on a device such that the absorption may be tuned sequentially from short to long wavelength.

Deeper analysis on the cause of reduced J_{sc} upon incorporation of pentacene encapsulation despite the increased optical absorption as discussed in this thesis should be carried out in future. This will require the measurement of surface energies to enable better self-assembly of the pentacene molecule when encapsulating Ag nanoparticles using contact angle measurements.

It would also be suitable if the kinetics and energetics of the annealing process for solar cells annealed at optimum temperature be investigated. This is essential in understanding the diffusion mechanisms and rates of the PCBM in P3HT or otherwise. Understanding of the kinetics is useful in the establishment of the optimum nano morphology that gives higher efficiency.

Workshop/ Conferences attended

i) Oral presentation: Held (23/10-27/05/2014). 7th International Symposium on Macro- and Supramolecular Architectures and Materials entitled (MAM-14): Surface Plasmon Resonance effect to enhance photo-conversion efficiency of organic solar.

ii) Oral presentation: Held (29/10-31/10/2014). Material for energy research group annual workshop. 'Enhancement of photo-conversion efficiency of organic solar cells by surface Plasmon resonance effect'. held in Free- State in South Africa.

iii) Poster presentation: Held (28/10-29/10/2014). The 6th Cross faculty graduate symposium showcasing graduate research at Wits. 'Enhancement of photo-conversion efficiency of organic solar cells by surface Plasmon resonance effect.'

iv) Oral presentation: Held (28th June- 3rd July 2015). The 2015 South African Institute of Physics annual conference held in Boardwalk Convention Centre. Port Elizabeth- South Africa.

v) Attended the International school for material for energy and sustainability IV (ISMES IV) - 13-20th July 2015 held in Colorado school of Mines – United States of America (USA).

vi) Won 1st prize in the team challenge at the International school for material for energy and sustainability IV (ISMES IV) - 13-20th July 2015 held in Colorado school of Mines – United States of America (USA).